DISSERTATION

MEASUREMENTS OF ELECTRON-ION COLLISION RATES AND RYDBERG ATOM POPULATIONS IN ULTRACOLD PLASMAS BY USING SHORT ELECTRIC FIELD PULSES

Submitted by

Wei-Ting Chen

Department of Physics

In partial fulfillment of the requirements

For the Degree of Doctor of Philosophy

Colorado State University

Fort Collins, Colorado

Fall 2017

Doctoral Committee:

Advisor: Jacob Roberts

R. Steve Robinson
John Harton
Deigo Krapf

ABSTRACT

MEASUREMENTS OF ELECTRON-ION COLLISION RATES AND RYDBERG ATOM POPULATIONS IN ULTRACOLD PLASMAS BY USING SHORT ELECTRIC FIELD PULSES

Ultracold plasmas are good tools for studying fundamental plasma physics. In particular, these plasmas are well-suited to study so-called strong coupling physics - the physics of plasmas where nearest-neighbor Coulomb interactions become large enough to cause spatial correlations and break assumptions. An ultracold plasma makes such a good tool because it is it is free of interactions with neutral atoms, and has a well controlled and tunable initial conditions. The UCPs in this work were created from the photoionization of cold ^{85}Rb atoms. The experiments described in this thesis are focused on the measurements of damping of electron center-of-mass oscillations. We developed a method that uses two short electric field pulses to map the temporal profile of the oscillation amplitude. We found that the damping of such oscillations can result from dephasing which is a collisionless mechanism or from electron-ion collisions or a combination of both. Thus, we separate the study of two pulse measurements into two parts. The first part of the two short electric field pulse measurement is about the measurements and modeling of in the collisionless damping regime. The second part will focus on the regime where the damping is dominated by electron-ion collisions where we not only observed strong coupling influence on electron-ion collision rates, but also saw break down of one or more standard assumptions used in plasma physics calculations.

Rydberg atoms can be formed in ultracold plasmas through three-body recombination process. Our setup was capable of measuring Rydberg atoms in a energy range above the bottleneck energy. We measured the Rydberg populations at different temperatures, and our preliminary results agree well with a parameter-free calculation. However, there are some unexplained parts of our measurements on early time Rydberg populations. This means more studies are needed in the future in order to interpret our results and make use of them.

Future work includes measurements of the strong coupling influence on electron-ion collision rates in a magnetized ultracold plasma, measurement of Rydberg population below the bottleneck energy, a detailed study of evaporations in ultracold plasmas.

ACKNOWLEDGEMENTS

The works in this thesis are supported by lots of people. First, I would like to thank my advisor Professor Jacob Roberts. Working in his lab, I obtained lots of knowledge and skills for conducting a research. I especially appreciate all the discussions we had (physics-relevant or not) from which I gained a lot. He always thinks positively and this is very helpful for me to get through the difficulties encountered in our experiments. I would also like to thank Craig Witte for his simulation support that is crucial for us to understand our the experimental results. His work also helped us understand our system in a more thorough and deep way. I want to thank John Guthrie for his simulations on the Rydberg atom populations which helps us interpret our measurements. Finally, I have to thank my parent and relatives in Taiwan for their unconditional support for my studying abroad.

TABLE OF CONTENTS

Chapter 1

Introduction

In this chapter, a broad introduction to plasmas and their connections to strong coupling physics will be described. In addition, we will explain the advantages of using ultracold plasmas to study strong coupling influences in plasmas.

1.1 General Introduction to Plasmas

A plasma is a collection of charged particles dominated by interparticle Coulomb forces. Not all collections of charged particles can be considered plasmas. For example, although cosmic ray ionization involves charged particles, the dominant interaction is not between the charged particles, but between neutral particles and charged particles. Therefore, cosmic ray ionization cannot be viewed as a plasma. Another example is an electron beam, which is a collection of charged particles, but the mutual interaction between electrons in the beam is usually weak in comparison to external fields. In this case, plasma effects play an insignificant role unless the beam is dense enough or the kinetic energy is small enough [1].

In plasmas, the importance of inter-particle Coulomb forces results in collective behaviors for the charged particles. One collective response is screening, whereby charged particles arrange themselves in response to electric fields so that the electric fields seen inside the plasma is reduced. Other examples of a collective behaviors in a plasma are waves or oscillations. These sorts of collective behaviors are characteristic features of plasmas.

Plasmas can be found in wide varieties of natural environments. On earth, the ionosphere is a plasma environment. In space, plasmas are almost everywhere: from stars, large-planet cores, solar wind, various types of jets, dense stellar object remnants (i.e., white dwarves and supernovas), active galactic nuclei, and inter-galactic-scale interactions. Plasma physics is also important in the laboratory environment. Examples include: fusion physics, high-energy density plasmas [2], laboratory astrophysics, and strong coupling systems.

Experimental work in plasma physics is important for several reasons. First of all, most of plasma systems are difficult to directly simulate due to the long range nature of Coulomb forces.

Table 1.1: The strong coupling parameter Γ for different types of plasmas

Type of Plasma	Γ
Tokamak	$\sim 10^{-6}$
ICF	$0.01 \sim 0.1$
Ultracold Plasma(UCP)	$0.1 \sim 10$
Warm Dense Matter	$1 \sim 10$
Jupiter core	~ 100

The number of particles in the system, and the associated time and dimension scales can sometime span orders of magnitude. By experimenting, the validity of different plasma theories can be tested. In addition, new experimental results can shed light on some problems in models that are unseen before. For example, for astrophysical plasmas, spectroscopic data is a crucial parameter for modeling. A spectrum measurement on highly charged iron ions in Z-pinch experiment (Sandia Lab) [3] indicates that the originally well accepted and well established model of the Sun (which itself is a plasma) has significant problems.

Figure 1.1 shows several different types of plasma graphed with respect to density and temperature [4].Plasmas occupy almost 20 orders of magnitude range on both axes of the temperature-density parameter space.

1.2 Strong Coupling in Plasma Physics

One way to categorize these plasmas is by looking at the strong coupling parameter Γ, which is the ratio of the averaged inter-particle Coulomb energy to thermal energy:

$$\Gamma = \frac{1}{4\pi\epsilon_0}\frac{e^2}{a}\cdot\frac{1}{k_b T} \tag{1.1}$$

where ϵ_0 is the electric permittivity in vacuum, e is the electron charge, k_b is the Boltzmann constant, T is the temperature of the particles, and $a = (\frac{4}{3}\pi n)^{-\frac{1}{3}}$ is the Wigner-Seitz radius, where n is the plasma density.

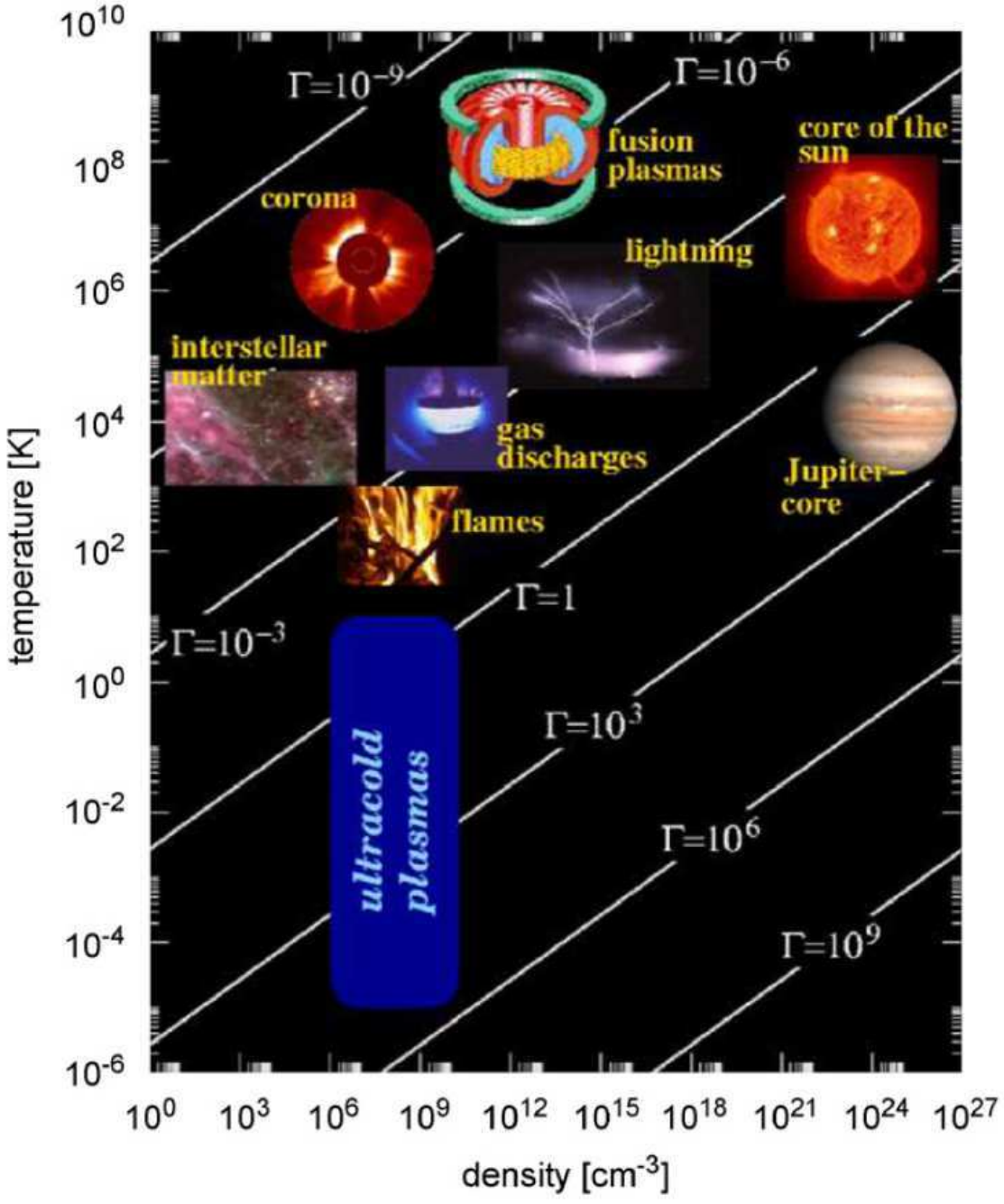

Figure 1.1: Different types of plasmas in density and temperature parameter space.

From the perspective of strong coupling parameters, the degree of Coulomb coupling strength varies significantly among different types of plasmas. Table 1.1 lists some plasmas and their corresponding Γ.

When the strong coupling parameter Γ of a plasma increases, the inter-particle Coulomb energy becomes more significant than thermal energy. Therefore, particles in the system build up spatial correlations.

Figure. 1.2 shows the radial distribution function $g(r)$ for different Γ, where $g(r)$ represents the probability of finding another particle at a distance r away from a given particle [5]. Interesting behaviors such as crystallization will show up in very strongly coupled systems. Some theoretical expressions for fundamental properties like screening and collisions are also expected to be modified due to the strong inter-particle Coulomb interaction as compared to expressions obtained through weak coupling treatments. For example, the conventional weak coupling collision rate is proportional to $\Gamma^{3/2}\ln(a\Gamma^{-3/2})$, where a is a constant. This expression obviously fails when $\Gamma \gg 1$ for it gives a non-realistic physical result of a negative collision rates. Therefore the collision rate formula needs to be modified to include the strong coupling effect. The equation of state is also expected to be altered accordingly when Γ increases. For weakly coupled plasmas, the equation of state is the same as it is for ideal gases, $PV = Nk_bT$. The application to the ideal gas equation of state assumes the interactions between particles are negligible. When the Γ becomes large, it means that the interactions between particles play a significant role and therefore the ideal gas equation of state will no longer apply. The equation becomes

$$PV = Nk_bT + U_{ex}/3 \tag{1.2}$$

where U_{ex} is the excess internal energy which can be written as

$$\frac{U_{ex}}{Nk_bT} = \frac{n}{2k_bT}\int \mathrm{d}\mathbf{r}\frac{(Ze)^2}{r}[g(r)-1] \tag{1.3}$$

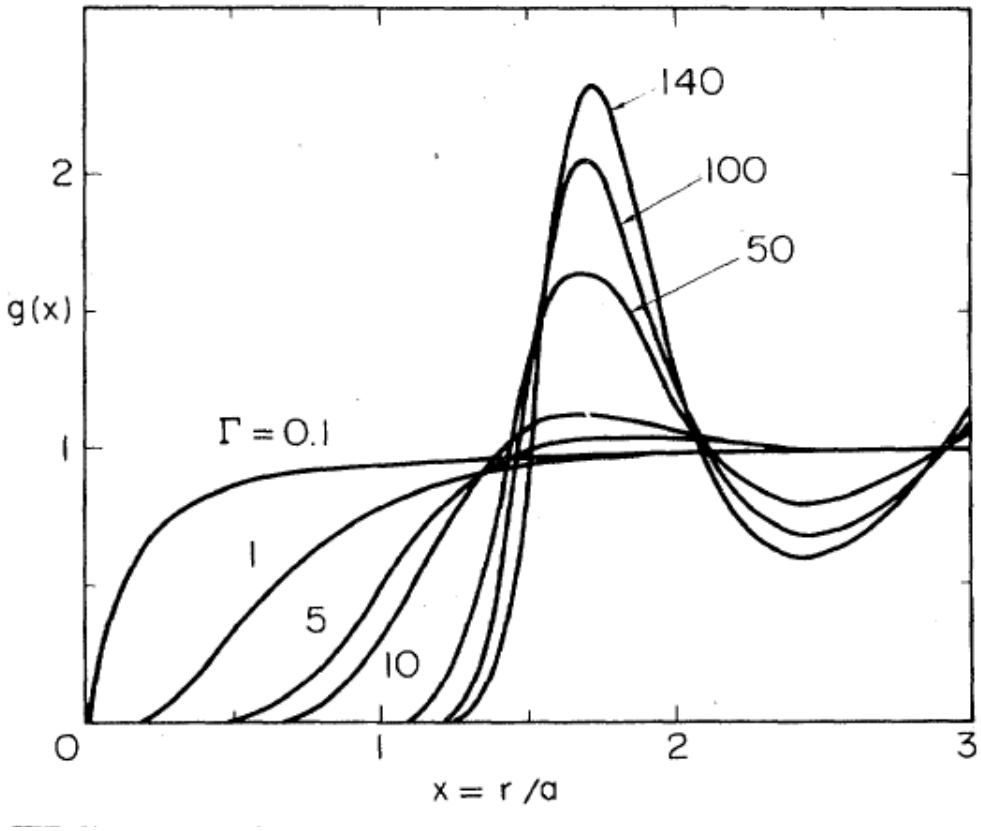

Figure 1.2: Radial distribution function of plasmas of different Γ.

where n is the number density, Z is the number of the charge, e is the electron charge, and $g(r)$ is the pair correlation function of the charged particles. Equation 1.2 and 1.3 are in Gauss units.

Under strong coupling conditions, expressions for both collisions and the equation of state must be modified. Therefore, properties related to transport phenomenon, such as diffusion which can be due to either collisional or collisoinless mechanisms (e.g. turbulence), also must be modified accordingly. The build up of spatial correlations increases the complexity of theoretical treatments. Thus theoretical treatments and formulas or expressions that are adequate for weak coupling plasmas break down when strong coupling effects become significant.

There are numerous theoretical works regarding treatments in the strong coupling regime [6–10]. However, experimental results are needed to test these theories. Several laboratories are able to conduct research in the strong coupling regime, such as ultracold ion plasmas [11] and dusty plasmas, [12] and are capable of achieving the degree of strong coupling necessary for Wigner crystallization. Ultracold plasmas are also good tools for strong coupling research because they are tunable with well-controlled initial conditions. In addition, ultracold plasmas are two component plasmas (i.e. have electrons and ions) and are thus suitable for studying interactions between unlike charges.

1.3 Waves in Plasmas

Oscillations are one of the hallmark characteristics of collective behaviors in plasmas. One of the most important plasma oscillationd is the cold plasma electron oscillation. The frequency of such an oscillation is $\sqrt{e^2 n/m\epsilon_0}/2\pi$. This frequency determines a natural time scale for plasma dynamics. In addition, in many plasma conditions, such as those found in astrophysical plasmas or in fusion plasmas, there exists an environmental external magnetic field. This field breaks the spatial symmetry in a plasma and can produce other categories of oscillations and modes. There are also a wide range of plasmas can be described using hydrodynamics, such that instabilities like the Rayleigh-Taylor instability or the Kelvin- Helmholtz instability and turbulence can also be observed. These instabilities and turbulences are important in momentum and energy transport in some plasma systems. Although recent research has been widely conducted in high energy density plasmas [13, 14], these particular instabilities are not the focus in this study.

1.4 Collisions in Plasmas

Collisions are important phenomena in plasmas. They are the fundamental processes for a plasma to establish thermal equilibrium and most plasma calculations make the assumption that plamsas are in thermal equilibrium. The velocity relaxation and energy relaxation time are directly related to collision rates. Collisions are also relevant to the stopping power problem, which studies energy loss associated with a charged particle moving through a medium. At velocities lower than a typical thermal velocity, the stopping power is influenced dominantly by collisions. Stopping power considerations are important in many contexts, including in DT fusion plasmas.

Treatments for collisions in plasmas are based on calculating the deflection of momentum and change of enenrgy due to Rutherford scattering. The scattering potential is a Coulomb potential, which is a long range force. This long range interaction leads to a logarithmic divergence when averaging impact parameters for calculating the expected amount of deflection. In order to avoid the divergence, an *ad hoc* cutoff based on screening is introduced. This cutoff treatment works well for weakly coupled plasmas but fails when the plasma is sufficiently strongly coupled. Thus, as mentioned previously, this requires modification for strongly coupled plasmas. Numerical simulation of collision rates is further complicated because of the long range nature of the Coulomb interaction (i.e. it is a N^2 problem), hence calculations of nearest neighbor interactions are insufficient. Advances in computer technology yielding increasing computation power in the past decade have made direct modeling of systems such as ultracold plasmas possible. However, direct modeling for large plasma systems is not yet possible.

Collision rate measurements of ion-ion collisions were conducted in the Γ range of approximately 1 to 3, which lead to a need to extend collision theories in order to correctly compare the theoretical predictions to the measurements [15], or the implementation of a more sophisticated effective potential theory [16]. Studies of electron-ion collisions have been performed in several different types of plasmas, including this work as the primary area of study.

1.5 Advantages of Using Ultracold Plasmas

Ultracold plasmas (UCPs) can be created by the photoionization of ultracold atoms [17] or supersonic molecular beams [18]. The initial kinetic energy of the plasma electrons can be calculated

using the degree to which the ionization photon energy exceeds the ionization threshold. After the UCP is created, it will undergo expansion with a lifetime on the order of few tens to a hundred μs.

UCPs have several advantages over other plasmas in the study of plasma physics. First of all, a UCP is a clean system with well controlled and tunable initial conditions due to the fact that the atomic and ionization state are known. It has an open boundary, thus the boundary condition is well-defined. The roughly one hundred μs lifetime is a reasonable experimental timescale that allows for the use of standard electronics for measurements. The achievable strong coupling parameters of UCPs can range from 10^{-3} to 5, which contain both weak and strong coupling regimes. Its interaction with neutral species is negligible. A relatively small numbers of particles in UCPs, especially for our low density conditions, allows the one-to-one comparison between the experiments and simulations. On one hand, we can use the experimental measurements to check the model. On the other hand, with the help of the modeling, it allows us to better interpret our data and extract relevant physics. The UCP apparatus is a tabletop size experiment similar to the study of ultracold ions and dusty plasmas, so the cost is relatively low. In conclusion, UCPs are excellent systems for testing fundamental plasma physics.

References

[1] D. G. Swanson, Plasma Kinetic Theory. CRC Press (2008)

[2] *10th International Conference on High Energy Density Laboratory Astrophysics*, High Energy Density Physics **17**, Part A, Pages 1-218 (2015)

[3] J. E. Baily *et al.*, Nature (London), **517**, 56 (2015)

[4] T. C. Killain, T. Pattard, T. Pohl, J. M. Rost, Physics Reports, **449**, 77-130 (2007)

[5] S. Ichimaru, Rev, Mod. Phys., **54**, No.4., 1017 (1982)

[6] D. O. Gericke and M. S. Murillo, and M. Schlanges, Phys. Rev. E **65**, 036418 (2002).

[7] Guy Dimonte, and Jerome Daligault, Phys. Rev. Lett. **101**, 135001 (2008).

[8] Paul E. Grabowski, Michael P. Surh, David F. Richards, Frank R. Graziani, and Michael S. Murillo, Phys. Rev. Lett. **111**, 215002 (2013).

[9] S. D. Baalrud, Phys. Plasmas **19**, 030701 (2012).

[10] L. G. Stanton and M. S. Murillo, Phys. Rev. E **91**, 033104 (2015).

[11] J. N. Tan, J. J. Bollinger, B. Jelenkovic, and D. J. Wineland, Phys. Rev. Lett. **75**, 4198 (1995).

[12] H. Thomas, G. E. Morfill, V. Demmel, J. Goree, B. Feuerbacher, and D. Mhlmann, Phys. Rev. Lett. **73**, 652 (1994).

[13] E. C. Harding, J. F. Hansen, O. A. Hurricane, R. P. Drake, H. F. Robey, C. C. Kuranz, B. A. Remington, M. J. Bomo, M. J. Grosskopf, and R. S. Gillespie, Phys. Rev. Letts. **103**, 045005 (2009).

[14] V. A. Smalyuk, S. X. Hu, V. N. Goncharov, D. D. Meyerhofer, T. C. Sangster, D. Shvarts, C. Stoeckl, B. Yaakobi, J. A. Frenje, and R. D. Petrasso, Phys. Rev. Letts. **101**, 025002 (2008).

[15] G. Bannasch, J. Castro, P. McQuillen, T. Pohl, and T. C. Killian, Phys. Rev. Lett. **109**, 185008 (2012)

[16] S. D. Baalrud and J. Daligault, Phys. Rev. Lett. **110**, 235001 (2013)

[17] T. C. Killian, S. Kulin, S. D. Bergeson, L. A. Orozco, C. Orzel, and S. L. Rolston, Phys. Rev. Lett. **83**, 4776 (1999).

[18] J. P. Morrison, C. J. Rennick, J. S. Keller, and E. R. Grant, Phys. Rev. Lett. **101**, 205005 (2008).

Chapter 2

Basic Plasma Physics and Ultracold Plasmas

In this chapter, some basic plasma physics concepts important to UCPs will be introduced. These include shielding, plasma oscillations, and collisions. These concepts will be treated in individual sections below. This will be followed by an introduction to UCPs that includes the creation process, evolution after formation, and heating and cooling mechanisms.

2.1 Debye Shielding

In this section, the shielding of electric fields by plasmas will be discussed. This is a fundamental characteristic of all plasmas and, in fact, is a crucial consideration in the definition of a plasma. A plasma is a collection of charged particles that interacts through inter-particle Coulomb forces. If an extra charge is introduced in a plasma, the other charged particles in the plasma will move in response to the introduced charge in a way that reduces the net electric field that results from the addition of the extra charge. This phenomenon is called screening or shielding. Under standard assumptions [1], the potential is no longer a Coulomb potential, but an Yukawa potential:

$$V(r) = \frac{1}{r} e^{-r/\lambda_D} \tag{2.1}$$

$$\lambda_D = \sqrt{\frac{\epsilon_0 k_b T}{e^2 n}} \tag{2.2}$$

where r is the distance to the charge, n is the density of the plasma, and λ_D is called Debye screening length, which is the length scale of this effect. Within λ_D, the potential is close to a normal Coulomb potential, but beyond a λ_D distance away from the charge, the potential will have become reduced significantly as compared to the original Coulomb potential. For moving charged particles, only particles moving fast enough are going to participate in the screening, altering the screening length of such particles. This effect is called dynamical screening [1]. It also implies that while electrons can screen the fields from ions, ions can not screen the electrons due to the huge mass ratio between ions and electrons. In order for a collection of charged particles to be a

plasma, their spatial extent has to be greater than the associated screening length. Otherwise, the system is just a collection of charges that cannot respond collectively, and hence is not a plasma. In addition, the screening effect is relevant to the collision processes in a plasma, which is an important consideration for the work in this thesis.

2.2 Plasma Oscillations

Displacements of electrons from equilibrium in a plasma tend to cause the electrons to oscillate back and forth around the equilibrium position in a longitudinal wave-like manner. These oscillations are called simply "plasma oscillations" in general. One way to calculate the oscillation frequency of such motion is by considering the displacement of electrons in an infinite isotropic plasma. It is straight forward in that case to calculate the restoring force form the space charge and obtain the oscillation frequency [1]. There are other ways to obtain the frequency, such as through a dielectric response treatment [2], or from a velocity autocorrelation function [3]. Regardless, the angular frequency of this fundamental plasma oscillation is

$$\omega_p = \sqrt{\frac{ne^2}{m\epsilon_0}} \tag{2.3}$$

where m is the mass of the charged particle, either electrons or ions for electron and ion oscillations respectively. This frequency is a natural unit of plasma electron/ion dynamics as demonstrated in [4]. One thing to note with regard to UCPs is that for a spherically symmetric plasma, there is a $1/\sqrt{3}$ correction factor for the cold plasma frequency. The density in the formula should be replaced by a spatially averaged density [5].

$$\omega_p = \sqrt{\frac{\langle n \rangle e^2}{3m\epsilon_0}} \tag{2.4}$$

where $\langle n \rangle$ is the spatial averaged density.

This frequency is density dependent and therefore the density of the plasma can be measured using the oscillation frequency. Such a measurement can be performed by different methods in

a UCP. If a continuous radio frequency (RF) electric field is applied to a UCP, and if a layer of the UCP has the right density to absorb the energy resonantly from the RF electric field, this energy twill then be transferred to the other layers of the UCP, which will result in an increase in electron temperature. This increase of electron energy will result in an increase in the number of escaping electrons, which can then be detected [6]. Alternatively, a short few-cycle RF pulse can be applied to initiate an electron center-of-mass motion in a UCP. The oscillation will create an internal oscillation field that drives electrons at proper locations in phase space out of the plasma. The larger the amplitude of the electron oscillation, the more electrons are expelled. The amplitude of the electron oscillation depends on the frequency applied to the UCP. By scanning the RF frequencies, it is possible to obtain the resonant frequency [5]. In yet another method, the velocity auto-correlation function can be used to extract plasma frequency in molecular dynamic simulations [7]. Other collective modes can exist in a UCP, such as Tonks-Dattner mode [8], as well.

Because of the density dependence of plasma oscillation frequencies, plasma frequency measurements are the primary method in which the UCP density was determined in this thesis. The plasma frequencies also often inform our intuition about how rapidly the UCP could respond to an external influence (e.g. electric field). It is also a natural time unit for relaxation processes in plasmas. The measurement and analysis of the damping of plasma oscillations covered in later parts of this thesis represents the major results of this work.

2.3 Collisions in Plasmas

The main goal of this thesis is to study the strong coupling influence on electron-ion collision rates using a UCP system. The importance of studying collisions is that they are fundamental processes in a plasma that are relevant to other important properties. For instance, thermal equilibrium is assumed in most of the theoretical works concerning plasma physics. Collisions are the critical mechanism that can bring a system into thermal equilibrium since collisions can transfer both energy and momentum between particles in a random fashion. Transport properties, such as diffusion or viscosity, are also related to collisions (e.g. Brownain motion). Further, stopping power considerations, which deal with the energy dissipation $\mathrm{d}E/\mathrm{d}x$ of a charged particle

projectile moving in a plasma, are important in understanding deuterium-tritium (DT) plasmas [9, 10] and associated fusion in these systems. In some regimes, the loss of the energy of a projectile is dominated by collisions. Collisions are also important when interspecies interaction is significant, so that a simple two fluids model is not adequate to describe such plasmas.

There are numerous theoretical works that focus on collisions using different approaches. Early works on calculating collisional effects focused on weakly coupled plasmas. The methods included using the Fokker-Planck equation and a $1/r$ potential to calculate transport coefficients from collisions [11], or by calculating the Rutherford scattering cross-section and then calculating the average momentum loss rate using a the Maxwell-Boltzmann velocity distribution [12]. Other attempts to predict collision rates have been in the context of the stopping power problem. Different strategies were used for calculating $\mathrm{d}E/\mathrm{d}x$, such as dielectric response method [13], scale invariance(BPS model) [14], generalization of the Fokker-Planck treatment(LP model) [15], or directly through classical molecular dynamic simulations [16, 17]. An alternative method for obtaining collision-linked transport coefficeints is by using an effective potential method [18, 19], from which quantities such as diffusion or friction can be calculated. In addition, the sign of the charge between interacting charges was predicted to modify the collision rates (Barkas effect)[13, 20], but such an modification has not yet been measured experimentally.

While the conventional binary collision rate formula used to describe collisions in plasmas works for $\Gamma \sim 10^{-3}$ or less, extensions to more strongly coupled regimes have been gradually developed theoretically. Improvements in recent works [14, 15] extend the applicable strong coupling regime to $\Gamma \sim 0.1$. The effective potential treatment further extends the applicable range to $1 \sim 10$. With the aid of technology and algorithm developments, the vast increase in computation power has enable using molecular dynamic simulations in the study of strongly coupled plasmas as well.

2.3.1 Collision Cross-Section and Coulomb Logarithm

This section includes a short introduction to conventional collision treatments in plasma physics. Calculating the binary Rutherford cross-section from Coulomb forces in a plasma will show the need for cutoff parameters (or integration limits), and where the term "Coulomb logarithm" originates. The choice of a cutoff parameter and the validity of binary collision will also be discussed.

In a standard treatment for binary collisions for a central force, one can move to the center-of-mass frame [21]. The following derivations and notations are mainly from [1]. In the center-of-mass frame, the deflection angle θ_c resulting from scattering via the Coulomb forces is given by

$$tan\frac{\theta_c}{2} = \frac{Z_1 Z_2 e^2}{4\pi\epsilon_0 \mu v_0^2 b} \tag{2.5}$$

where Z_1 and Z_2 are charge numbers, μ is the reduced mass, v_0 is the incident velocity, and b is the impact parameter.

Note that the quantity $Z_1 Z_2 e^2/4\pi\epsilon_0\mu v_0^2$ is usually denoted as b_0 which is the impact parameter that produces a deflection angle of 90°.

The next step in computing the effects of collisions on particle motions in a plasma is to calculate the average deflection of the velocity over impact parameters. The first step is to determine the square of the velocity deflection of one encounter δv at an impact parameter b.

$$(\delta v_\perp)^2 = v^2 sin^2\theta_c = \frac{4v^2(b/b_0)^2}{[1+(b/b_0)^2]^2} \tag{2.6}$$

If the density of the scattering center is n, then $nv_0 2\pi b\mathrm{d}b$ will be the number of encounters per unit time for an impact parameter b. Therefore, the average velocity deflection per unit time then becomes

$$\begin{aligned}\langle(\Delta v_\perp)^2\rangle &= 4v_0^2(2\pi n v_0)b_0^2\int_0^{b_m/b_0}\frac{(b/b_0)^3\mathrm{d}(b/b_0)}{[1+(b/b_0)^2]^2} \\ &= 8\pi n v_0^3 b_0^2\int_0^{x_m}\frac{x^3\mathrm{d}x}{(1+x^2)^2} \\ &= 4\pi n v_0^3 b_0^2[\ln(1+x_m^2)+\frac{1}{1+x_m^2}-1]\end{aligned} \tag{2.7}$$

where $x_m = b_m/b_0$. For condition $x_m^2 \gg 1$, (2.7) can be further simplified to

$$\langle(\Delta v_\perp)^2\rangle = 8\pi n v_0^3 b_0^2 \ln(x_m) \tag{2.8}$$

Several things about the above equation should be noted. First, the integral in (2.7) diverges logarithmically, which requires a cutoff of the impact parameter in the upper integration limit to avoid divergence. As shown in [22], density fluctuations less than the scale of Debye screening length λ_D are associated with individual particle motions, while those larger than λ_D are from collective behaviors, not random fluctuations. Therefore, the b_m in the integration upper limit is naturally chosen to be λ_D. The term $\ln \lambda_D/b_0$ is called a Coulomb logarithm and is usually denoted as $\ln \Lambda$. There is also an underlying assumption of the validity of the binary collision formalism in the treatment. In [23], under the assumption of approximately straight-line collision trajectories, the author estimates $\langle v_\perp \rangle^2$ using the autocorrelation of an electric field acting on a particle that gives a binary collision form of Eq. 2.8. Other treatments using test particles moving in a plasma showed the binary collision approximation is valid for ions with subsonic speeds [24]. The assumption that $x_m^2 \gg 1$ implies the deflection is dominated by the accumulation of numerous small angle deflections.

(i.e. large b). For example, if $b_m = 570b_0$, from (2.5), the scatterings occur with $b > 10b_0$ consisting of more than 99.9% of all scattering events, and their corresponding scattering angles are less than 0.2 radians. This small angle deflection assumption is valid for weak-coupled plasmas. For example, the $b_m = 570b_0$ case corresponds to a strong coupling parameter $\Gamma \sim 10^{-2}$, and x_m is about $10^3 (\gg 1)$.

2.3.2 Collision-Related Rates

To determine natural collision timescales, the first step is to calculate the angles of deflection per unit time from (2.8). Since this thesis is focused on the electron-ion collision rate, the collisions considered from here forwards will refer to electron-ion collisions specifically.

$$\langle (\Delta\theta)^2 \rangle = \frac{\langle (\Delta v_\perp)^2 \rangle}{v^2} = 8\pi n v_0 b_0^2 \ln(\Lambda) = \frac{n Z_1^2 Z_2^2 e^4}{2\pi \epsilon_0^2 m_e^2 v_0^3} \ln(\Lambda) \tag{2.9}$$

For a quick estimation of the rate for a particle to deflect by roughly $\pi/2$, we pick $\langle (\Delta\theta)^2 \rangle \sim 1$. The rate then becomes $\nu_{\pi/2} \approx \frac{n Z_1^2 Z_2^2 e^4}{2\pi \epsilon_0^2 m_e^2 v_0^3} \ln(\Lambda)$.

To get a better determination, one can also look at the rate that the velocity changes from its original direction, which is closely related to stopping power. The change in momentum of a test

particle of mass m and velocity v incident on a field of particles is $mv[1 - cos(\theta)]$ for a deflection angle θ. Averaging this change over all impact parameters for a given relative velocity using eq. (**??**) and then multiplying this result by the particle flux leads to

$$\dot{p} = -m_e\nu(v)v = -m(\frac{nZ_1^2Z_2^2e^4}{4\pi\epsilon_0^2m_e^2v^3}\ln\Lambda)v. \tag{2.10}$$

By averaging $\dot{p}$ over a Maxwellian-Boltzmann velocity distribution, the collision rate of the incident particles can be calculated[25].

$$\nu = \frac{1}{3}\sqrt{\frac{2}{\pi}}\frac{Z_1^2Z_2^2e^4n_i}{4\pi\epsilon_0^2m_e^2v_{th}^3}\ln\Lambda \tag{2.11}$$

where $v_{th} = \sqrt{k_BT/m}$.

There are other ways of obtaining similar expressions for the collision rate, such as calculating the stopping power of a charged particle using the plasma dielectric response function[13], through dimensional continuity[14], or through a generalized Fokker-Planck equation[15]. The need of a cutoff length to avoid the divergence of Coulomb logarithm from (2.7) is clear in any treatment. However, we note that the conventional choice of $C = 1$ for $b_m = C\lambda_D$, although reasonable, is *ad hoc* without proper theoretical justification, and $C = 1$ will not likely be the correct coefficient. In the work of [14], different approaches were used that yield the factor $C = 4e^{-2\gamma}/\sqrt{e} \simeq 0.765$, where $\gamma \sim 0.577216$ is the Eular constant. This was supported by MD simulation results[16, 17]. The results in this thesis suggest that determining collision rates is even more complicated than that presented here. This will be discussed in chapter 5 of this thesis.

One interesting feature of these collision rates is that they can be written as a function that only depends on Γ and ω_p, $\nu/\omega_p = \sqrt{2/\pi}\Gamma^{3/2}\ln\Lambda(\Gamma)$, since Λ is a function of $\lambda_D/b_0 = (\sqrt{3}\Gamma^{3/2})^{-1}$. This means the amount of collisions are the same after the same plasma period if you fix Γ, even for plasmas with wildly different temperatures and densities. In other words, at the same Γ, all binary collision induced slowing produces the same result in unit of time equal to the inverse plasma frequency. Thus by plotting the scaled damping rate with respect to Γ, the binary collision rate from all plasmas would be expected to fall on a universal curve[26]. Similar scaling also holds on three-body recombination rates, which will be discussed in chapter 6.

2.3.3 Extensions to Strong Coupling Regime

So far, all discussions above are limited to weak-coupling treatments, but recently there are several works that attempt to extend the Coulomb logarithm expressions into the strong coupling regime. They include T-matrix treatments, MD simulations, effective potentials, and dielectric response function treatments.

The T-matrix treatment[27] uses the form for the Coulomb logarithm of $\ln(1 + b_m^2/b_0^2)$ but constructs several different types of cutoff for b_m and b_0, and then compares them to a T-matrix calculation to determine the best choice of cutoffs. In classical regimes, b_m is set to be $\sqrt{\lambda_D^2 + a^2}$, while b_0 remains the same, where a is Wigner-Seitz radius, and that produces reasonable agreement with T-matrix-predicted rates in a classical limit, at least when considered on a log plot.

Another method is using MD simulations to extract the empirical forms that modify Coulomb logarithms. For modeling thermalization between charge particles, the modified Coulomb logarithm is [16]

$$\ln \Lambda = \ln(1 + \frac{0.7}{\sqrt{3}\Gamma^{3/2}}) \tag{2.12}$$

instead of the weak-coupling form $\ln(0.765/\sqrt{3}\Gamma^{-3/2})$. In addition, the low velocity limit of stopping power is dominated by collisions. Thus one can also obtain the form of Coulomb logarithm by investigating the low velocity limit obtained from stopping power results [17]. The high velocity limit of stopping power is dominated by wave excitation which is irrelevant to collisions. The Coulomb logarithm obtained from stopping power results through MD simulation is

$$\ln \Lambda = \ln [1 + \frac{4e^{-2\gamma}e^{-1/2}}{\sqrt{3}\Gamma^{3/2}(1 + a\sqrt{3}\Gamma^{3/2})}] \tag{2.13}$$

where $a = 1.04102 \times 10^{-5}$. This form is almost identical to (2.12) except for extremely high Γ.

A recent study by Stanton and Murillo calculated the collision integral for a Yukawa potential and determined its analytical expressions. The authors used those collision integrals and introduced an effective screening lengths to calculate transport coefficients of ions in a plasma such as self-diffusivity, viscosity and thermal conductivity, and found good agreement when comparing their results to MD simulations [19].

Another way to extend the Coulomb logarithm expression to strong coupling regimes is through working with effective potentials. The main idea is to find an effective two-body potential to describe a many body process. The form of the argument in the Coulomb logarithm depends upon the type of the potential. For a Coulomb potential with a *ad hoc* distance cutoff, the Coulomb logarithm is of the form $\ln\Lambda = \ln\left(1 + C\lambda_D^2/b_0^2\right)$. Comparing this to (2.12), it can be seen that these two form cannot reduce to each other except in a weak coupling regime. This means the two expressions correspond to different forms of differential cross-sections, which indicated different forms of effective two-body scattering potentials. The work from Baalrud [18] calculated the effective potential by solving the hypernetted chain equations instead, and produced a similar result as [16] (i.e. similar to equation 2.12).

The plasma dielectric response function treatment mentioned above used a weak-coupled response function, and they extended this treatment to strong coupling regime [13].

From this and previous sections, it is clear there are indeed lots of theoretical works that calculate strong coupling corrections through different approaches. For the results presented in this thesis, the main effort is to measure strong coupling effect on electron-ion collision rates and compare the measurements to simulations based on different models. We found that although the effect from strong coupling is very dear experimentally, simulations that directly apply the strong coupling corrections presented above did not match our observations. We determined this is partly due to the lack of validity of one or more assumptions commonly used in collision treatments. A more detailed discussion will be presented in chapter 5.

2.4 Introduction to Ultracold Plasmas

Ultracold plasmas (UCPs) can be created by the photoionization of either ultracold atoms [28] or molecular beams [29], making UCPs clean and well controlled plasma system. They usually have a spatial size on the order of mm, and their density ranges from 10^7 cm^{-3} to 10^{15} cm^{-3}. The temperature of a UCP can range from a few degrees of Kelvin to a few hundreds of degrees.

In our system, they are created through photoionizing ultracold ^{85}Rb atoms [30]. The excess photon energy of the ionization photons will be converted into the initial electron kinetic energy, so there is some control of the initial temperature of the electrons in the UCPs. Since the temper-

ature of UCPs can range from a few degrees to a few hundred degrees Kelvin, the study of both weakly-coupled and strongly-coupled plasmas is possible. UCP interactions with neutral atoms are negligible due to the small collision cross-section of atoms in part due to the small ratio between the plasma temperature to the atom binding energy. The lifetime of our UCPs is typically tens of μs, which is long enough for us to take the measurements that we are interested in. The UCP has a finite extent with an open boundary. UCPs are classical systems even though the temperatures are usually only a few Kelvins. This can be seen by comparing the de Broglie wavelength to the Wigner-Sietz radius, or by comparing the electron kinetic energy to their Fermi energy [31]. For a 1 K electron, the de Broglie wavelength is 0.11 μm, and the Wigner-Sietz radius is 6 μm for a density of $10^{15}m^{-3}$. The Fermi energy for density $10^{15}m^{-3}$ is $\hbar/2m_e(3\pi^2 n_e)^{2/3} \sim 4.2 \times 10^{-5}K$ which is much smaller than few Kelvin energy scale of UCPs.

2.4.1 Evolution of UCPs

Shortly after UCPs are formed via photoionization, there is no trapping potential, so some electrons will leave the plasma freely because they have non-zero kinetic energy.As electrons leave the UCP, however, it will start to build up a space charge (more ions than electrons in the UCP). This will create a self-trapping potential that eventually will become deep enough to trap the rest of the electrons in the UCP.

Since the electrons have finite temperatures, their thermal pressure will create an internal radial electric field that drives the the plasma ions to expand. This can be demonstrated by assuming a Gaussian spatial density distribution of the plasma and a quasi-neutral condition ($n_i \approx n_e$), and then using the Boltzmann relation

$$n(r) = n_0 e^{U(r)/k_B T} = n_0 e^{-r^2/2\sigma^2} \tag{2.14}$$

where n_0 is the plasma density at $r = 0$, $U(r)$ is the total plasma potential, and σ is the characteristic spatial extent of the plasma [47]. The force can be calculated by taking the gradient of the potential energy obtained by this approximate treatment

$$-\partial U(r)/\partial r = \frac{k_B T}{\sigma^2} r \tag{2.15}$$

which indicates a electric force aligned in the positive r direction after accounting for the fact electrons and ions have opposite charges. Thus, the ions in the UCP expand under the influence of the electron thermal pressure. This is illustrated in Fig. 2.1. When the plasma expands, the self-trapping potential will be reduced, which enables more electrons to escape from the UCP. This evaporation of electrons can affect the electron temperature. The overall evolution of a UCP is shown and related to our measured micro-channel plate signal based on the electron escape rate in Fig. 2.2.

In order to interpret our measurements, it is crucial to determine the temperature precisely is. The processes involved in the creation stage of a UCP and the expansion after the UCP creation each have influences on the temperature of the UCP. Mechanisms affecting the UCP temperatures are described in more detail later in this chapter. We thus have to take these considerations into account for the design of the experiments and for the modeling as well.

2.4.2 Mechanisms That Affect The Temperature

One main goal of studying UCPs is to explore and measure the strong coupling effects in a classical Coulomb system. Strong coupling in UCPs can be reached mainly by making the temperature of the component of interest (electrons, ions or both) as low as possible. Therefore, it is necessary to understand mechanisms that affect plasma temperatures other than the initial kinetic energy from the ionization photons. This section will describe several heating and cooling mechanisms in UCPs.

Disorder Induced Heating (DIH)

Before cold atoms are ionized, the atoms have a random spatial correlation with one another. When a UCP is formed, the correlation energy between the charged particles will be released and turned into heat, since the charge particles' distribution is not at the minimum electric potential configuration initially. This is primarily because with a random distribution there are pairs of newly created electrons and ions that are closer to one another than would be the case at equilibrium when Coulomb repulsion has forced them to expand. This heating process is called disorder induced heating. This is theoretically investigated by Murillo[32] for one component plasmas, and was then seen in molecular dynamic simulations for electron components[32]. Since this heating effect is

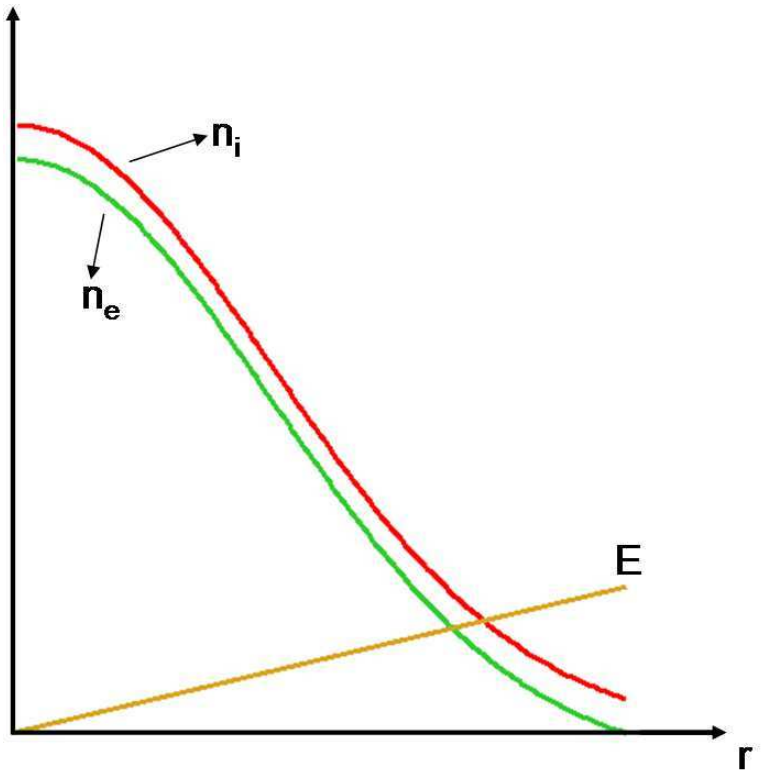

Figure 2.1: Demonstration of electron thermal pressure that drives ion expansion in a UCP. r is the radial position. n_e and n_i are electron and ion density respectively. E is the electric field generated due to the difference between electron and ion density. The less dense electron distribution results in a linear radial electric field that makes the UCP to expand. The densities shown are calculated within the neutrality approximation described in the main text.

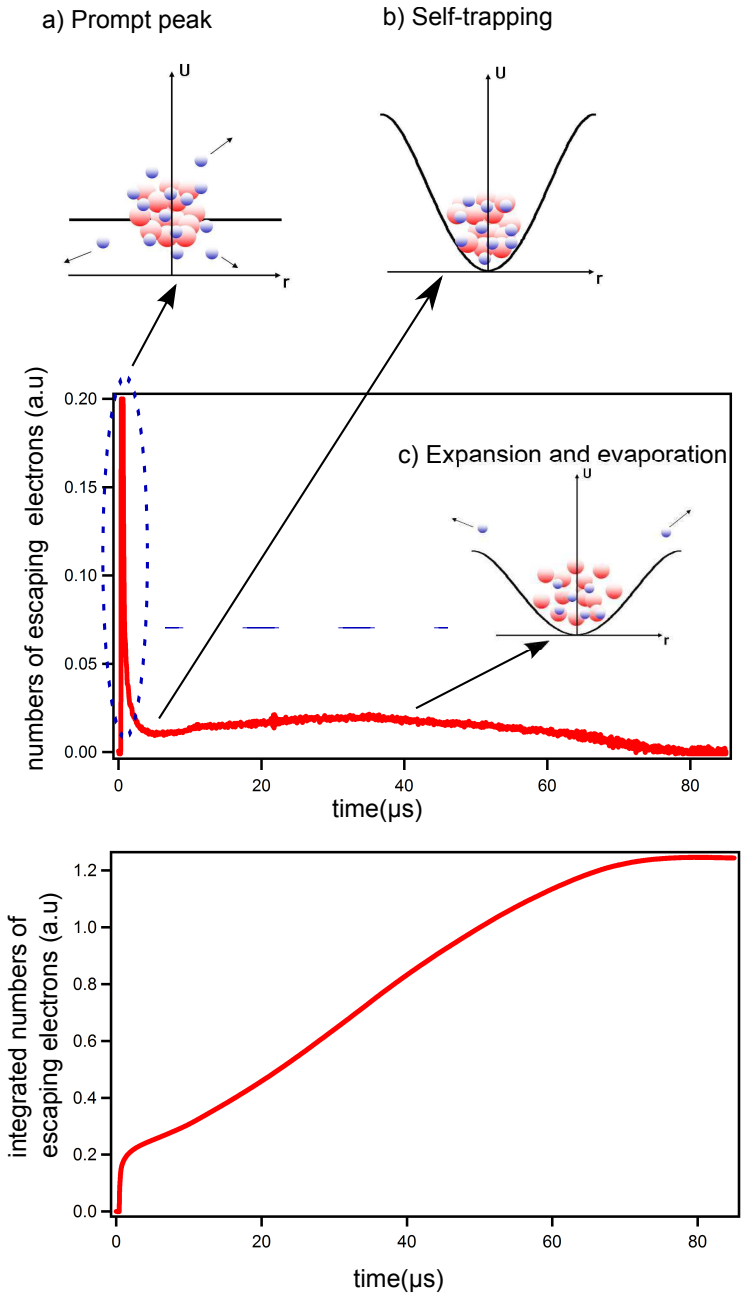

Figure 2.2: Typical UCP traces measured by our micro-channel plate. The trace in the middle is the electron escape rate vs time, and the bottom trace is the integrated electron escaping signal vs time. Inset a), b) and c) represent different stages of UCP evolution. Inset a) illustrates the prompt peak, b) is when the UCP to forms a self-trapping potential, and c) is the electron evaporation due to the expansion of UCP.

unfavorable for reaching strong coupling, so several ways were proposed to reduce the disorder induced heating under the idea of introducing order into the system before plasma creation. These methods include starting the photoionziation from a degenerate Fermi gas[32], placing atoms in optical lattices[33], or exciting atoms to high principle quantum number Rydberg states to form an ordered structure utilizing the strong interaction between Rydberg atoms[34]. One can also increase the coupling strength of the ions by a second ionization at a carefully chosen timing [35], or direct removal of heat from the system by laser-cool the ions [36]. One may think that by simply moving to a low density regime, one can reduce the effect of DIH. However, since DIH scales with $n^{-3} = a^{-1}$, reducing the density indeed reduce the amount of heating, but this also decreases the nearest neighbor Coulomb energy by the same portion. Therefore, reducing DIH by decreasing density does not increase Γ due to the reduction of interparticle Coulomb energy.

The research in [32] is based on assuming a Yukawa potential where the amount of heating depends on the ratio of Winger-Seitz radius to total screening length $\kappa = a/\lambda_D$ and strong coupling parameter Γ. Therefore, by knowing the electron temperature and ion density, the ion temperature can be calculated from the model. By comparing the predictions of ion temperatures to the measuremed ion temperatures, one can examine how well the Yokawa potential can describe the system. Agreement was found agreements between the two[4]. Electron screening plays an interesting role in DIH, since on one hand it reduces the effect of local correlation which leads to reduction in DIH. On the other hand, the screening also reduces the interaction potential between ions which lowers the coupling strength. This results in an estimated upper limit of ion strong coupling around $\Gamma \sim 4$ without delibirate suppression or elimination of DIH [37].

Although the experimental results associated with DIH described above deal with the ion component of UCPs, this heating is also expected to take place for the electron component in a UCP. We estimated that the DIH for our experimental conditions is less than 0.1 K. More detailed analysis is presented in chapter 4.

Continuum Lowering

The concept behind continuum lowering is that the ionization potential of an atom will be reduced by neighboring ions. This phenomenon also has other names such as threshold lowering or ionization potential depression (or suppression). If the ionization potential is decreased but the

photon energy used for ionization process remains the same, then an additional amount of kinetic energy will be added to the ionized electron, which will heat the electron component of the plasma as illustrated in Fig. 2.3.

This reduction in ionization potential is important in that for a dense plasma system, especially for those in which ions have different ionization states, the lowering of ionization potential changes the ionization balance and limits the number of accessible bound states, hence changing the charge state distribution, which will affect the equation of state and opacity of the plasma. Therefore, the understanding of continuum lowering is important not only for research in astrophysics plasmas for both theoretical modeling and the interpretation of observed spectroscopic data [39], but also in inertial confinement fusion (ICF) plasmas [40, 41]. Several experiments were conducted in solid state targets using different light sources such as x-rays from a free electron laser[40] or Nd glass laser (Orion facility)[41], and the ionization threshold lowering was directly obeserved though spectroscopic data. However, these two experiments support different theoretical models. The results from the free electron laser experiments support Ecker and Kroll's model [40] while the Orion laser experiments support Steward and Pyatt's model [41]. Even more surprising, a recent experiment found a lack of density dependence (i.e independent of interparticle spacing) on the threshold lowering between Al and Al_2O_3 for which the density difference was expected to be a factor two [42]. This factor of two difference should have been large enough to detect continuum lowering differences between the two cases. These recent experimental results confirmed the existence of the threshold lowering effect but also indicate the need for more experimentation to obtain a better understanding of continuum lowering.

So far, the study on continuum lowering has focused on very dense plasmas. One may wonder : can continuum lowering play a role in affecting the temperautre in relatively dilute plasma systems such as UCPs? Although the density of our UCP is about 15 orders of magnitude lower than those dense (e.g soild target) plasma systems, the temperature in UCP systems can be about seven orders of magnitude lower so that the heating from the continuum lowering may limit the lowest temperature our UCPs can achieve, as suggested by Hahn [43]. The predicted amount of suppression of the ionization potential depends on different models. Ecker and Kroll(EK) [44] used statistical mechanical and thermaldynamical treatments. To accomodate the results in Ref. [44] in

our system,we note that the charge number is unity, and the dielectric constant is approximated to be unity as well. The formula (eq. (56) and eq. (57) in [44]) becomes

$$\Delta T_{EC} = \begin{cases} \frac{1}{3}\frac{e^2}{4\pi\epsilon_0\lambda_D} & \text{for } n \leq n_{cr} \\ \frac{2\cdot 2.2}{3} n_{cr}^{-1/3} (\frac{e^2 n_{cr}}{k_b T})^{1/2} & \text{for } n \geq n_{cr} \end{cases} \tag{2.16}$$

where ΔT_{EC} is the amount of temperature increase due to continuum lowering, n is the plasma density and $n_{cr} = (3/4\pi)[4\pi\epsilon_0 k_b T]$ is the critical density, which represents the density when strong coupling parameter Γ is unity, and T is the ion temperature. The density of our UCPs is about $10^7 cm^{-3}$, the ion temperature is about 1 mK to 10 mK when the plasma is just formed, so n_{cr} is about $5 \times 10 cm^{-3}$ which is below the density of the UCP. This gives a electron temperature increase of 0.34 K. If we take into consideration the fact that it takes a finite time for the atoms to become a plasma, the density of the plasma is zero initially and is n after the ionization process complete. Therefore by averaging the continuum lowering effect through the density evolution, the temperature increase is about 0.25 K.

Stewart and Pyatt(SP) used Thomas-Fermi model and Fermi-Dirac statistics for the electrons and then solve the Poisson equation for the electrostatic potential[45].

$$\Delta T_{SP} = \frac{k_b T_i}{3\bar{Z}}[(1+\Lambda)^{2/3} - 1] \tag{2.17}$$

where $\bar{Z}$ is the effective charge, which is unity in our system, and $\Lambda = (3\Gamma)^{3/2}$. If we use the same estimation of heating as used in Ecker and Kroll case, the temperature increase given by Steward and Pyatt is 0.29 K, or 0.21 K if averaged through density evolution.

Hahn tried to explain the plateaued expansion rate in UCPs at low temperatures [43] by continuum lowering. Hahn used the result from density functional theory extrapolated to the UCP regime, which produces an estimation of the heating

$$\Delta T_H = \frac{2}{3} C_p \frac{e^2}{4\pi\epsilon_0 a k_b} \tag{2.18}$$

where $C_p = 11 \pm 5$, and a is the Wigner-Seitz radius. For a density of $10^7 cm^{-3}$, a is about $28\mu m$, so the estimated heating is $4.3K \pm 1.9K$. Given the estimated amount of temperature increases

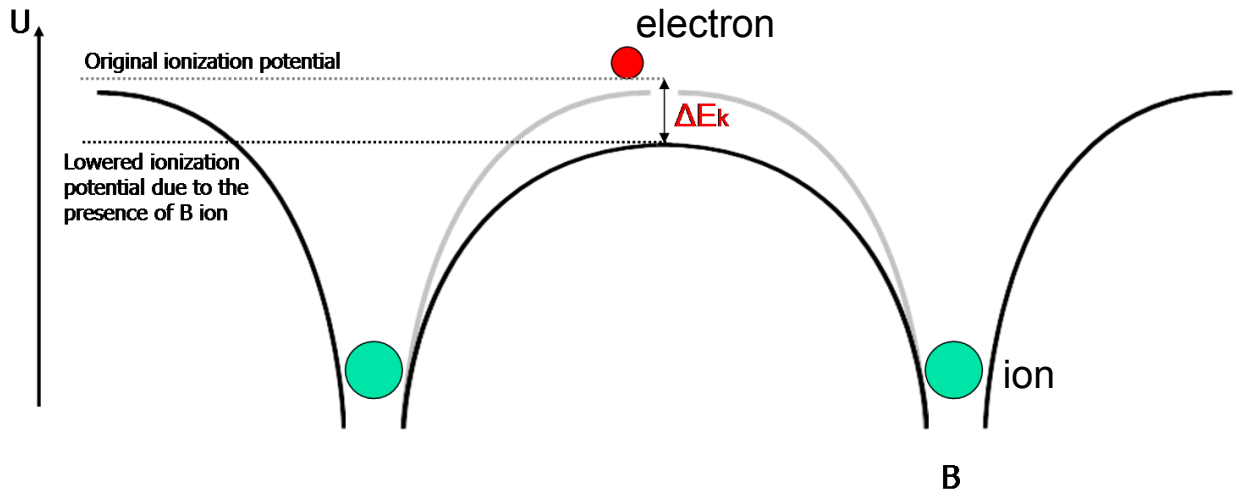

Figure 2.3: Illustration of continuum lowering. The ionization potential is reduced due to the presence of the neighboring ion B.

from continuum lowering, this could be a detectable effect for a UCP of temperature about $1 \sim 2$ K according to SP and EK predictions, and a very significant effect from Hahn's prediction.

However, MD simulations that were performed in our research group (see chapter 5) observed little heating of electrons. This is contrary to the simple predictions described in the previous paragraph. This is thought to be coming from the expansion due to the thermal pressure of electrons in UCPs, which is an effect more prominent in small and open-boundary systems. One can estimate this effect by a very crude model. Assuming an uniform distribution of ideal gas electrons of a initial temperature T_0, pressure P_0, and volume V_0. If the continuum lowering adds an amount of heat $k_b \Delta T$ to the system, by assuming the system will relax to its initial pressure P_0, we can calculate the final temperature, which is $T_0(1 + \Delta T/T_0)^{1/\gamma}$, where $\gamma = 5/3$ is the ratio of specific heat at constant pressure to specific of heat at constant volume for an ideal gas. If initial temperature converted from the excess energy of the ionization photon is 3 K, and the contribution from continuum lowering is 0.25 K, then the effective temperature increase is about 5%, which corresponds to 0.08 K and is close to what MD simulation calculated. If T_0 is set to 1.5 K, then the effect will be about 10%, but this amount of change of the initial temperature can be easily overcome by some small amount of evaporation or other heating mechanisms. Furthermore, in reality, the same cooling mechanism will reduce T_0 even in the absence of continuum lowering (and this effect is ignored in the above estimates). Thus, continuum lowering heating can compensate the cooling . This can make the actual temperature of the UCP stay roughly the same or even slightly lower than then expected temperature converted simply form ionization photons. Considering all of this, it would be very difficult for our current apparatus to quantify or even observe the influence from continuum lowering. This is unfortunate because having additional data could be beneficial in understanding some of the problems between experiments and theories present with respect to continuum lowering at this time.

In addition, there are concerns about the models themselves. Both EK and SP calculate the suppression of ionization potential assuming thermal equilibrium of ions. But in our system, the process where the continuum lowering may play a role is from those ions created by the ionization pulse, which is a very dynamical process. Hahn's description is more suitable for describing continuum lowering in UCPs, but it used extrapolated results from density functional treatments in a

dense plasma system to UCP conditions, instead of performing a formal treatment using density functional method in UCPs. Therefore, a more careful treatment on continuum lowering in UCPs that considers the dynamical processes and finite size effects is needed in evaluating its effects on UCP temperatures. The Hahn prediction is ruled out by our experimental results described in later chapters.

Three-body Recombination

Three-body recombination is a process where two electrons collide with an ion nearby, and one electron forms a bound Rydberg state with the ion (i.e. becoming a Rydberg atom) and the other electron gains kinetic energy to satisfy momentum and energy conservation(Fig. 2.4). Three-body recombination is the main source of Rydberg atom formation in UCPs. This is a plasma loss process, since one Rydberg atom is formed, and so one plasma ion and electron is lost. The conventional plasma three-body recombination rate is proportional to $T_e^{-9/2}$, where T_e is the electron temperature. This scaling is obtained by calculating probability of a binary collision of two electrons and multiplying that to the probability of findiing such an event near an ion [46] (see also chapter 6 in this thesis). This steep relation to temperature predicts a severe heating at low temperature, and this heating from three-body recombination is one of the main predicted limits to the degree of strong coupling achievable in UCPs. This heating is observed in several simulations. Some of the simulations look at the full time span of the plasma lifetime [47], and some of them focus on early time situations [7, 31, 36, 46]. A feature shared by these simulations is that the electron strong coupling parameter drops rapidly within 100 ω_p^{-1}, and then reaches a steady value of about 0.2 to 0.5 depending on the initial electron strong coupling parameter [31, 36, 46]. However, this recombination rate is expected to be modified when the electron strong coupling parameter becomes large [46]. The modification will be introduced in more detail in chapter 6 in this thesis.

Adiabatic Cooling

When a UCP is formed, the electrons will generate a thermal pressure that causes the ions to expand due to their finite temperature. While the system expands, the temperature of UCP electrons drops adiabatically. The expansion can be described via ion fluid equations - namely the

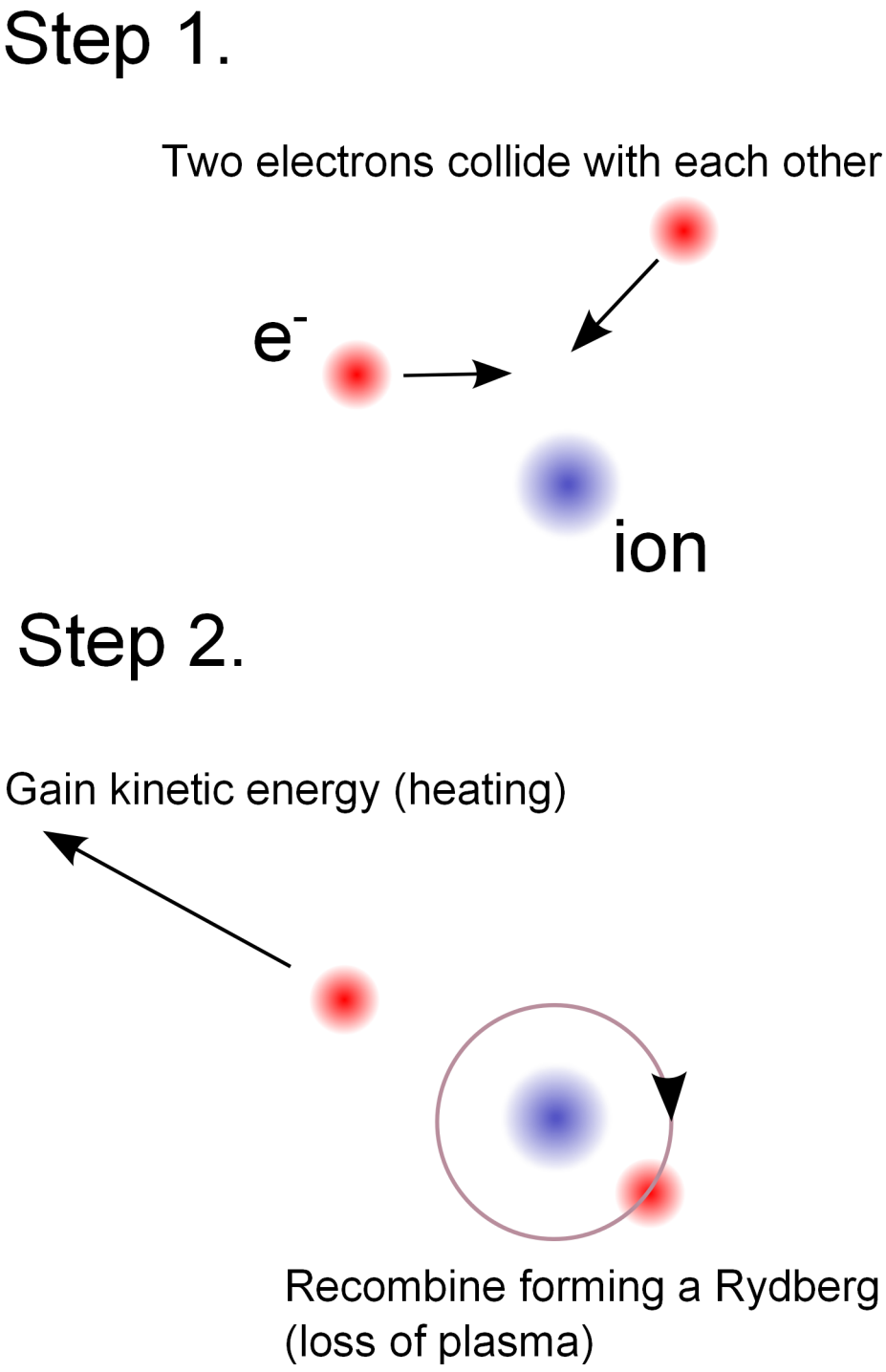

Figure 2.4: Illustration of three-body recombination process.

Euler equation and the equation of continuity [47]. Further approximations can be made as follows for a low temperature plasmas [47].

$$\begin{aligned} n_i(r,t) &= N_i[\beta(t)/\pi]^{3/2} e^{-\beta(t)r^2} \\ v_i(r,t) &= \gamma(t) r \\ a_i(r,t) &= 2\beta(t) k_b T_e r/m_i \end{aligned} \tag{2.19}$$

where n_i, v_i, a_i are the spatial density profile, velocity, and acceleration of the ions respectively. N_i is the ion number, r is the distance to the center, T_e is the electron temperature, and m_i is the ion mass. The first equation states that ions remain in a Gaussian spatial density distribution all the time (i.e. that a Gaussian UCP ion distribution expands self-similarly). The second specifies a linear increase of velocity with respect to their distance form the center. The last one indicates the electric field that drives the expansion is proportional to r so that the whole system will maintain a Gaussian profile while expanding. By substituting the above into an ion fluid equation, the expansion behavior and the temperature can be solved by a set of differential equations:

$$\begin{aligned} \frac{\mathrm{d}\gamma(t)}{\mathrm{d}t} + \gamma(t)^2 &= \frac{2k_b T_e(t)\beta(t)}{m_i} \\ \frac{\mathrm{d}\beta(t)}{\mathrm{d}t} &= -2\beta(t)\gamma(t) \\ \frac{3}{2}k_b \frac{\mathrm{d}T_e(t)}{\mathrm{d}t} &= -\frac{4}{3}N_i m_i \frac{\mathrm{d}}{\mathrm{d}t}\left(\frac{\gamma^2(t)}{\beta(t)}\right) \end{aligned} \tag{2.20}$$

where $\beta = 1/2\sigma^2$, and σ is the characteristic spatial extent defined in (2.15). A typical expansion and temperature evolution is demonstrated in Fig. 2.5.

As the expansion proceeds, the temperature becomes lower continously, and one might expect that the plasma could reach a stronger coupling strength. However, the three-body recombination will heat the system, and the Γ is predicted to level about 0.2 at later time of UCPs [47].

Some additional expansion can happen due to the net space charge of the UCP in addition to the electron thermal pressure. This extra expansion can also bring the electron temperature down. This cooling is estimated to have $\sim 10\%$ effect [48] for our conditions.

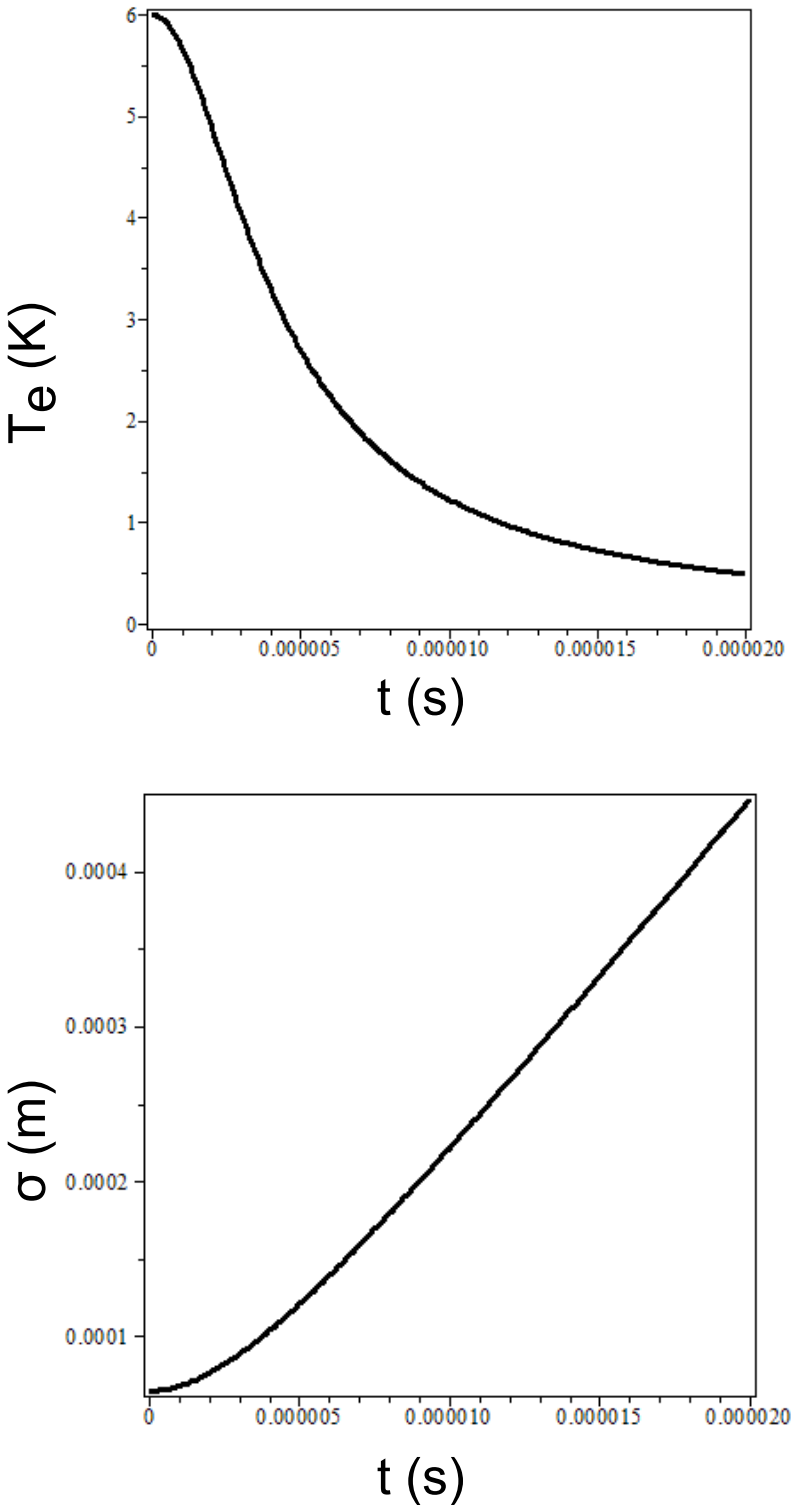

Figure 2.5: Illustration of the temperature (top) and the radius σ (bottom) evolution. The starting temperature $T_e(0)$ is 6 K and $\sigma(0)$ is 650 μm

Evaporative Cooling

Evaporative cooling is not only a common phenomenon in daily lives, but it is also used in atomic physics research to reach temperatures low enough for Bose-Einstein condensation. In evporative cooling, particles in the high energy tail of Maxwell-Boltzmann distribution escape from the system, so the average energy remaining in the system becomes lower.

In atomic physics, higher density leads to more effective evaporative cooling. However, counter-intuitively, in UCPs evaporative cooling is more important in low density cases. For a self-trapped system, the denser the UCP, the less it has to lose fractionally to maintain a trapping potential and thus the lower the maximum fractional number of electrons that can escape to drive cooling. The evaporativce cooling effect on expansion was observed in low density UCPs [49]. With the help of evaporative cooling, the strong coupling parameter at late time UCP evolution may be able to reach a higher value than 0.2 [49].

During the formation stage of a UCP, evaporative cooling can also play some roles in the early electron temperature, though the system is not yet in thermal equilibrium [49]. The effect can be estimated, but the estimated value is highly model dependent. Due to the complex physics during plasma formation, some detailed modeling is required to further investigate the problem.

The interplay between all of these heating and cooling mechanisms is important for our experiments. These mechanisms determine the temperature of electrons in the UCP, which is an important parameter we need to know. In addition, by understanding those heating and cooling mechanisms we are able to design where in parameter space we want to operate our experiments in order to reach higher Γ so that we can observe the strong coupling effect on collisional processes.

References

[1] D. G. Swanson, *Plasma Kinetic Theory*. CRC Press (2008).

[2] J. D. Jackson, *Classical Electrodynamics* 3rd. edition. John Wiley and Sons (1999).

[3] S. Ichimaru, Rev, Mod. Phys., **54**, No.4., 1017 (1982).

[4] Y. C. Chen *et al.*, Phys. Rev. Lett. **93**, 265003 (2004).

[5] Truman M. Wilson, Wei-Ting Chen, and Jacob L. Roberts, Phys. Rev. A, **87**, 013410 (2013).

[6] S. Kulin, T. C. Killian, S. D. Bergeson, and S. L. Rolston, Phys. Rev. Lett., **85**, 318 (2000).

[7] S. Mazevet, L. A. Collins, and J. D. Kress, Phys. Rev. Lett., **88**, 055001 (2002).

[8] R. S. Fletcher, X. L. Zhang, and S. L. Rolston, Phys. Rev. Lett. **96**, 105003 (2006).

[9] A. B. Zylstra *et al.*, Phys. Rev. Lett. **114**, 215002 (2015).

[10] J. A. Frenje *et al.*, Phys. Rev. Lett. **115**, 205001 (2015).

[11] M. N. Rosenbluth, W. M. Macdonald, and D. L. Judd, Phys. Rev. **107**, 1 (1957).

[12] L. S. Spitzer, *Physics of Fully Ionized Gases* (Dover, New York, 2006).

[13] Thomas Peter and Jurgen Meyer-ter-Vehn, Phys. Rev. A **43**, 1998 (1991).

[14] Lowell. S. Brown, Dean. L. Preston, and Robert. L. Singleton Jr., Physics Reports 410, 237-333 (2005).

[15] Chi-Kang Li and Richard D. Petrasso, Phys. Rev. Lett. **70**, 3059 (1993).

[16] Guy Dimonte, and Jerome Daligault, Phys. Rev. Lett. **101**, 135001 (2008).

[17] Paul E. Grabowski, Michael P. Surh, David F. Richards, Frank R. Graziani, and Michael S. Murillo, Phys. Rev. Lett. **111**, 215002 (2013).

[18] S. D. Baalrud, Phys. Plasmas **19**, 030701 (2012).

[19] L. G. Stanton and M. S. Murillo, Phys. Rev. E **91**, 033104 (2015).

[20] W. H. Barkas, J. W. Dyer, and H. H. Heckman, Phys. Rev. Lett. **11**, 26 (1963); **11**, 138E (1963).

[21] Herbert Goldstein, *Classical Mechanics* 2nd Edition, (Addison-Wesley 1980).

[22] David Pines and David Bohm, Phys. Rev. **85**, 338 (1952).

[23] R. S. Cohen, L. Spitzer, Jr., and P. McR. Routly, Phys. Rev. **80**, 230 (1950).

[24] S. Rand, Phys. Fluids **4**, 1251 (1961).

[25] P. Mulser, F. Cornolti, E. Besuelle, and R. Schneider, Phys. Rev. E **63**, 016406 (2000).

[26] G. Bannasch, J. Castro, P. McQuillen, T. Pohl, and T. C. Killian, Phys. Rev. Lett. **109**, 185008 (2012).

[27] D. O. Gericke and M. S. Murillo, and M. Schlanges, Phys. Rev. E **65**, 036418 (2002).

[28] T. C. Killian, Phys. Rev. Lett. **83**, 4776 (1999).

[29] J. P. Morrison, C. J. Rennick, J. S. Keller, and E. R. Grant, Phys. Rev. Lett. **101**, 205005 (2008).

[30] T. M. Wilson, W. T. Chen, and J. L. Roberts, Phys. Rev. A **87**, 013410 (2013).

[31] K. Niffenegger, K. A. Gilmore and F. Robicheaux, J. Phys. B **44**, 145701 (2011).

[32] M. S. Murillo, Phys. Rev. Lett. **87**, 115003 (2001).

[33] T. Pohl, T. Pattard, and J. M. Rost, J. Phys. B **37**, L183 (2004).

[34] G. Bannasch, T. C. Killian, and T. Pohl, Phys. Rev. Lett. **110**, 253003 (2013).

[35] M. Lyon, and S. D. Bergeson, Contrib. Plasma Phys. **55**, 399 (2015).

[36] S. G. Kuzmin and T. M. Oneil, Phys. Plasmas **9**, 3743 (2002).

[37] M. Lyon, and S. D. Bergeson, J. Phys. B **44**, 184014 (2011).

[38] T. C. Killain, T. Pattard, T. Pohl, J. M. Rost, Physics Reports **449**, 77 (2007).

[39] F. J. Rogers and C. A. Iglesias, Science 263, 50 (1994).

[40] O. Ciricosta *et al*,Phys. Rev. Lett. **109**, 065002 (2012).

[41] D. J. Hoarty *et al.*, Phys. Rev. Lett. **110**, 265003 (2013).

[42] Ciricosta *et al.*, Nature Comm. **7**, 11713 (2016).

[43] Y. Hahn, Phys. Lett. A **293**, 266 (2002).

[44] G. Ecker and W. Kroll, Phys. Fluid **6**, 62 (1963).

[45] J. C. Stewart and K. D. Pyatt, Astrophysic. J. **144**, 1203 (1966).

[46] G. Bannasch, and T. Pohl, Phys. Rev. A **84**, 052710 (2011).

[47] F. Robicheaux and J. D. Hanson, Phys. Rev. Lett. **88**, 055002 (2002).

[48] Craig Witte and Jacob L. Roberts, Phys. Plasmas **21**, 103513 (2014).

[49] T. M. Wilson, W.T. Chen, and J. L. Roberts, Phys. Plasmas **20**, 073503 (2013).

[50] T. M. Wilson, Dynamics of low-density ultracold plasmas in externally applied electric and magnetic fields, Ph.D. Dissertation (Colorado State University, 2013).

Chapter 3

Experimental Apparatus

This chapter describes in detail how the experiments in this study were run and calibratred. Since most of the details of the apparatus such as the laser systems, magneto-optic trap (MOT) and magnetic trap setup, electrode design, and the motional track that moves the anti-Hemholtz (AH) coil were presented in an earlier PhD thesis associated with the UCP experiments [1], only an overview of our experimental sequence will be provided so that reader can understand the big picture of how these experiments were performed. However, several modifications and improvements of the system were made in order to meet the requirements of newer experiments. In the second part of this chapter, I will describe why we need and how we implemented these changes in more detail. These changes dealt with multiple individual aspects for the apparatus and calibrations, and so the narrative will jump from topic to topic in the second part.

3.1 Experimental Sequence

The process of creating an ultracold plasma in our system is briefly described in this section. The first step is to create a cold atom cloud. In our experiment, we used a ^{85}Rb magneto-optic trap (MOT) to obtain cold atoms [2]. We loaded the MOT by red detuning the laser to collect atoms. Then we detuned the cooling laser to about 60 MHz to the red to compress the MOT through the reduction of internal radiation forces.

After compression, we then ramped up the current of the anti-Helmholtz coil associated with the MOT to 120 A and turned off both the cooling and repump laser to load the atoms into a magnetic trap. The repump laser is turned off first to load the atoms into the F=2 lower hyperfine state. When the loading was finished, we used a track to physically transfer the magnetic trap coils and thus the atoms toward another chamber for the plasma experiments. There is a differential pumping hole between the MOT chamber and plasma experiment chamber in order to maintain a better vacuum in the plasma chamber. The processes are illustrated in Figure. 3.1. The separation of the MOT and the plasma position is advantageous because it gives more optical accesses for

plasma creation so that the laser beam path will not be compromised by passing through metal grids as used in other UCP experiments [3].

The atoms are ionized through a two-photon ionization process. The two photon ionization consists of one photon to bring the atoms from ground state to the $5P_{3/2}$ state and then a second blue photon ionizes these excited atoms. We use a pulsed dye laser for the blue photon because its wavelength is tunable. We can tune the wavelength ($\sim$ 479 nm) to be above or below the ionization potential. If tuned above the ionization potential, the excess photon energy will be converted into initial kinetic energy of the ionized electrons. This is the way we typically operate the system. Our ability to control the wavelength of the photoionization laser means we can impart more or less initial kinetic energy to the ionized electrons to influence the electron temperature. The reasons that we can't completely control the electron temperature are described in section 2.4.2 and chapter 5. In contrast, if we tune the dye laser wavelength below the ionization potential, high n Rydberg atoms will be created instead. These Rydberg atoms will often ionize into UCPs shortly after the laser pulse [4]. These kinds of measurements were outside the scope of this thesis, so we do not report on such measurements here, but they are a capability of our system. Electrons escaping from the plasma were guided by the DC electric field from the electrodes and a set of grids toward our detector, a micro-channel-plate (MCP). The electron signal is magnified by the MCP and then goes through two stages of amplification. The signal from MCP is first amplified by a low noise SR445A(Stanford Research System)) pre-amplifier and secondly amplified by a factor of 4 by an op-amp. This signal is measured by a fast 1GHz scope (Lacroy 104MXs-B). This electron escape signal gathered by the MCP is our only signal from the UCP. From this signal we can deduce information about UCP, including the response to RF pulses, charge imbalance, total number, and evaporation rate.

In addition to the details presented in Ref. [1], there are two additional details we have observed, with respect to the general operation of the experiment. First, there are several wavelengths of the repump laser that will locally maximize the MOT in terms of atom number collected, but only one of them seems to be able to load and transfer an acceptable amount of atoms (35% to 40%) into the magnetic trap. The transition that does so is identified as the F=2 to F$'$=3 5S to 5P transition. Other wavelengths can only transfer about 10% or less of the atoms toward the plasma chamber region. This was verified by looking at the recapture signal. This phenomenon was observed with

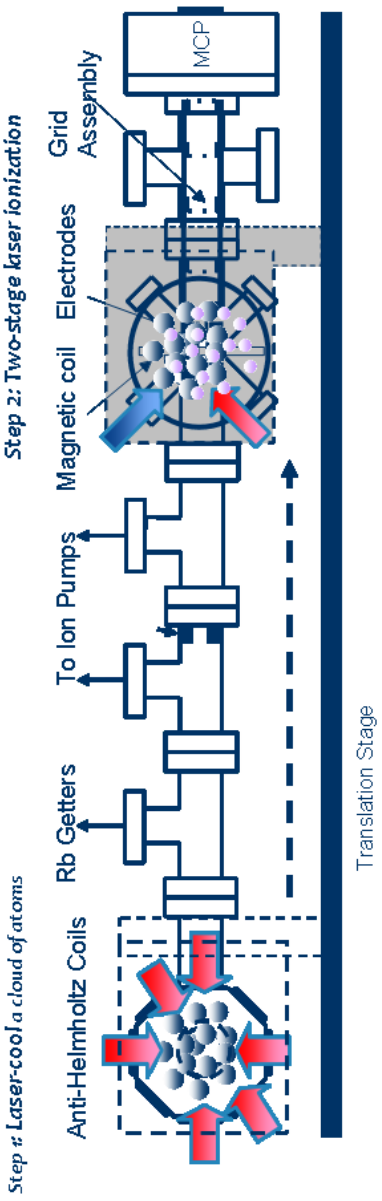

Figure 3.1: Experimental layout. The components of the vacuum apparatus are identified as their spatial relationship to one another.

different laser diodes which indicates it is not likely a problem associated with a particular diode laser. We are not able to fully characterize why this occurs, and were content to operate under the most favorable arrangement. Future studies may illuminate the underlying mechanism, which may be useful for optimal trap loading.

The recapture measurement is used to measure the amount of atoms captured in the magnetic trap. To conduct such a measurement, we first start from a MOT which contains atoms in various m_F states, then we turn off the cooling and repump laser and increase the current of the anti-Helmholtz coil at the same time. Atoms with positive m_F values will not be held by the magnetic filed gradient against the gravity, so they will leave the magetic trap. After about several hundred ms, when the untrapped atoms fully leave the magnetic trap, we turn on the cooling and repump laser, and the current of the AH coil is simultansously decreased. The atom remaining in the trap will fluorescence and we can measure the floresence signal by a photodiode (also see section 3.3.2 in Ref. [1]). By comparing the fluorescence before the atoms were loaded into the magnetic trap to the fluorescence after release the fraction trapped can be determined.

In an attempt to improve the uniformaty of the shot-to-shot behavior of the system, we adopted a technique to trap only one m_F state of the ^{85}Rb F=2 lower hyperfine state. The idea is to eliminate variations in the spatial extent of the atoms that occurs due to the variation of the m_F state populations loaded into the magnetic trap that arise from drifts in MOT alignment. The magnetic field gradient produced by the anti-Helmholtz coils at a current of 120 A is sufficiently large to trap the $m_F = -2$ and $m_F = -1$ states even when gravity is considered. The magnetic moment of each state is $2/3\mu_B$ and $1/3\mu_B$ respectively. Thus while both are trapped, the confinement is not the same. The trapping force on $m_F = -1$ is weaker than $m_F = -2$, and hence they have different spatial profiles [1]. In order to eliminate $m_F = -1$ atoms in the magnetic trap, we lowered the trap current below 120 A during the transfer stage of the atoms. Because the trapping force of $m_F = -1$ is smaller than $m_F = -2$, by properly reducing the current of the magnetic field during the transfer stage, we can remove the $m_F = -1$ atoms from the trap while the $m_F = -2$ atoms still remain.

To ramp the current, we control the set point of an electronic servo system that regulates the coil current magnitude. We then determine the required ramping voltage by observing the recapture fraction verses the ramping voltage. For the normal 120 A situation, $m_F = -1$ and

$m_F = -2$ atoms will be in the trap. If we gradually decrease the current to a value that is still large enough to trap both m_F state atoms, the recapture should remain unchanged. If the current is decreased sufficiently, the magnetic trap will not trap all the $m_F = -1$ state atoms. Then as the current decreases from this point, fewer and fewer $m_F = -1$ atoms will remain in the trap while all $m_F = -2$ atoms remain. As a result, the observed recapture fraction starts to drop. If the current further decreases but is still able to trap most of $m_F = -2$ atoms, then the recapture fraction will plateau. When the current drops further so that trap is not strong enough to trap most of the $m_F = -2$ atoms, the recapture fraction will decrease again. Eventually no atoms will stay in the trap if the current continues to decrease. This step like behavior is illustrated in Figure. 3.2.

We collected much of our electron-ion collision rate measurement data with only the $m_F = -2$ atoms in the magnetic trap. We did not notice, however, a strong improvement in the UCP shot-to-shot reproducibility, so our initial supposition with regard to potential problems from m_F state mixtures was not correct. Not having the $m_F = -1$ atoms, however, helping eliminate any systematic effects that could possibly arise for UCPs that were not approximately spherically symmetric when created. This was potentially useful and the performance of the apparatus was not adversely effected in any case.

3.2 The Choice of Operating Density

The UCP density we operated at is on the order of 10^7 cm^{-3}, which is about 2 orders of magnitude smaller as compared to other experimental groups in UCP research that create UCPs from ultracold atoms. There are several advantages for choosing to operate at low density, and while that was not an initial goal of the experimental apparatus, it is highly fortuitous and we take advantage of it for our experiments. For the electron-ion collision experiments that were conducted, a large charge imbalance was required for reasons described later in chapter 4 and chapter 5 in this thesis. Briefly, near uniform density was required in the region of the UCP where electrons were present, and the UCP is more uniform near the center. Large imbalances between electron and ion number concentrate electrons in the center of the UCP. Usually charge imbalances greater than 50% were used (i.e. less than 50 % of the electron remain in the UCP). A lower density UCP makes it easier to reach the charge imbalance we would like, since the UCP needs to lose a larger fraction

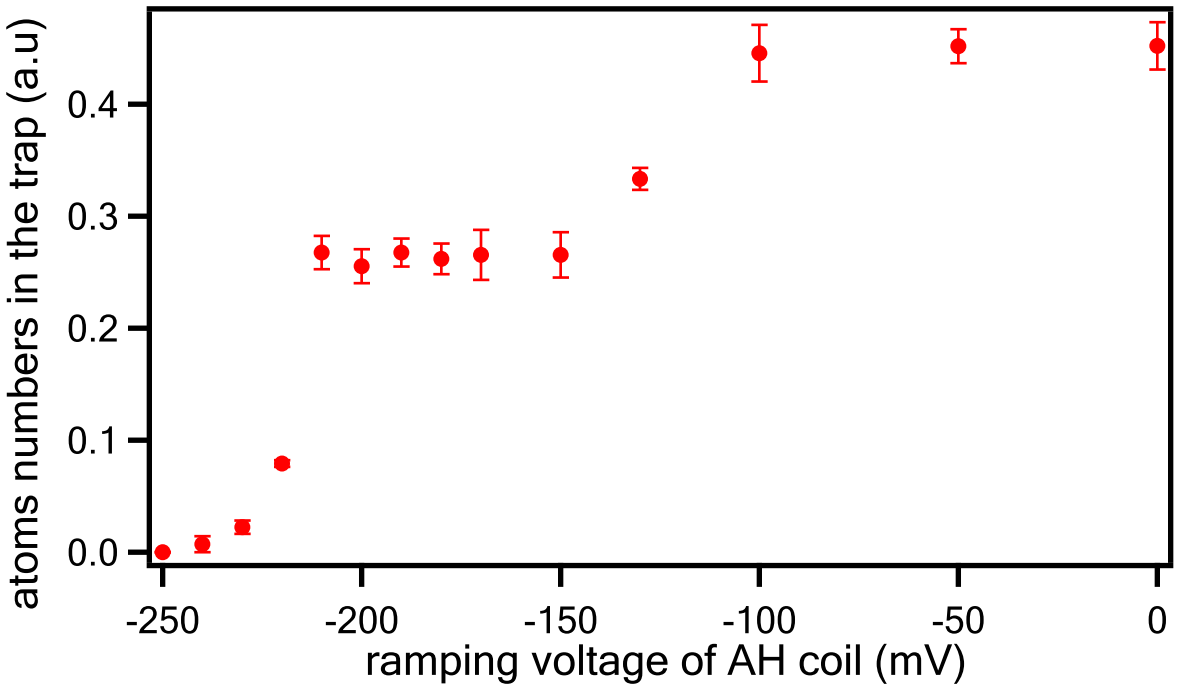

Figure 3.2: Number of atoms trapped in the magnetic trap at various ramping voltage of AH coil.

of electrons to create a self-trapping potential (see section 2.4.2). Another advantage is that the low density is favorable in reducing the effect from three-body recombination heating.

The three-body recombination rate scales with the plasma frequency and strong coupling parameter Γ such that the rate is proportional to $\omega_p \Gamma^{9/2}$. Thus under the same Γ, the recombination will be the same after the same number of periods ω_p^{-1}. Therefore, if we take a measurement at the same time after UCP formation t, the lower the density the smaller the ω_p and the smaller the $\omega_p t$, which means a smaller amount of heating due to three-body recombination. Thus, smaller density UCPs tend to have a smaller amount of recombination-induced heating shortly after formation.

In addition to three-body recombination, there are other heating mechanisms related to the nearest neighbor Coulomb energy, which is proportional to $n^{1/3}$, where n is the density. Any such heating mechanisms can also be reduced by using a lower density. For a sense of scale, if the density is 100 times lower, the reduction of heating is about a factor of 4.6. Using lower-density UCPs is thus advantageous with respect to other mechanisms as well.

3.3 Electric Field Calibration

Our experimental signal comes from the electrons that escape from the UCP. To reduce the trapping potential to help the electrons escape more easily in a wide variety of situations, a DC field was applied. The DC electric field is also necessary to guide the escaping electrons so that the electrons will not hit the chamber wall or an electrode on their way to the detector. Furthermore, the DC electric field was found to have influence on the initial temperature of the ultracold plasma (see chapter 5). Therefore, we need to know the electric field with a reasonable degree of precision. Ideally, the applied electric field could be determined directly from the applied electrode voltages. However, patch charge effects and uncertainties associated with the exact position of the electrodes prevent this.

To measure the electric field, we reduced the particle number of the plasma to operate slightly higher than the threshold number of ions required to form the plasma. This is done by reducing the 5s to 5p light intensity during the two-photon ionization process. 4 to 5 μs after the atoms were ionized, we applied an extraction electric field to pull out any electrons that still remained in the plasma. We then plot the total electron number N_t vs the extracted number N_{ext}. In other words,

we plot the total electron number vs. the electrons that were confined in the UCP. We perform this measurement at several different initial ionization energies.

The electric field affects both the threshold ion number required to form a plasma and the slope of the N_t vs N_{ext} curve. We therefore constructed a model to calculate the number extracted with respect to the total number as a function of the applied electric field. Using this model and collected calibration data, we then perform a χ^2 fit of the model with respect to the data to determine the best fit value of the electric field. Along with a fixed DC component, we may also have a component linear to the spatial coordinate in the direction along the electric field (which we lable the "z" direction), so we model the electric field E by specifying it along the z axis through the center of the UCP as $E = E_0 + E_1 z$ where E_0 and E_1 are constants. We also include the corresponding dipole and quadruple corrections to the UCP field that reflect this specification as described in [1]. With a given ion number, charge imbalance and electric field, we can calculate the depth of the trapping potential. For many conditions, there will be no net confining potential and the electron number that is extracted is zero. If the net confining potential is less than the initial electron kinetic energy, the electron number that can be extracted is also zero. These conditions are below the threshold for a given electric field. In addition, from the depth calculation a volume can be obtained where electrons can be confined given their kinetic energy. This volume can be related to the electron number through the UCP density. By altering the values of both DC and linear component of the external electric field, the model predictions can be compared to the measured data, and a determination of the best fit value of the external electric field could be made. For instance, the electric field calibration indicated a 2 V/m field with a ignorable linear field component for the latest run of experiments. The fractional precision of this measurement was determined from the chi-squared variation to be 5 %. Figure. 3.3 shows an example of measured data along with a fit from the model.

3.4 Velocity Kick Size Characterization

To apply short electric pulses to the ultracold plasma, we used a Tektronix AFG3012 dual channel function generator. The two output channels were combined by using a radio frequency splitter ZFSC-2-1-S+(Mini-Circuits). For experimental purposes, however, we need both a DC electric

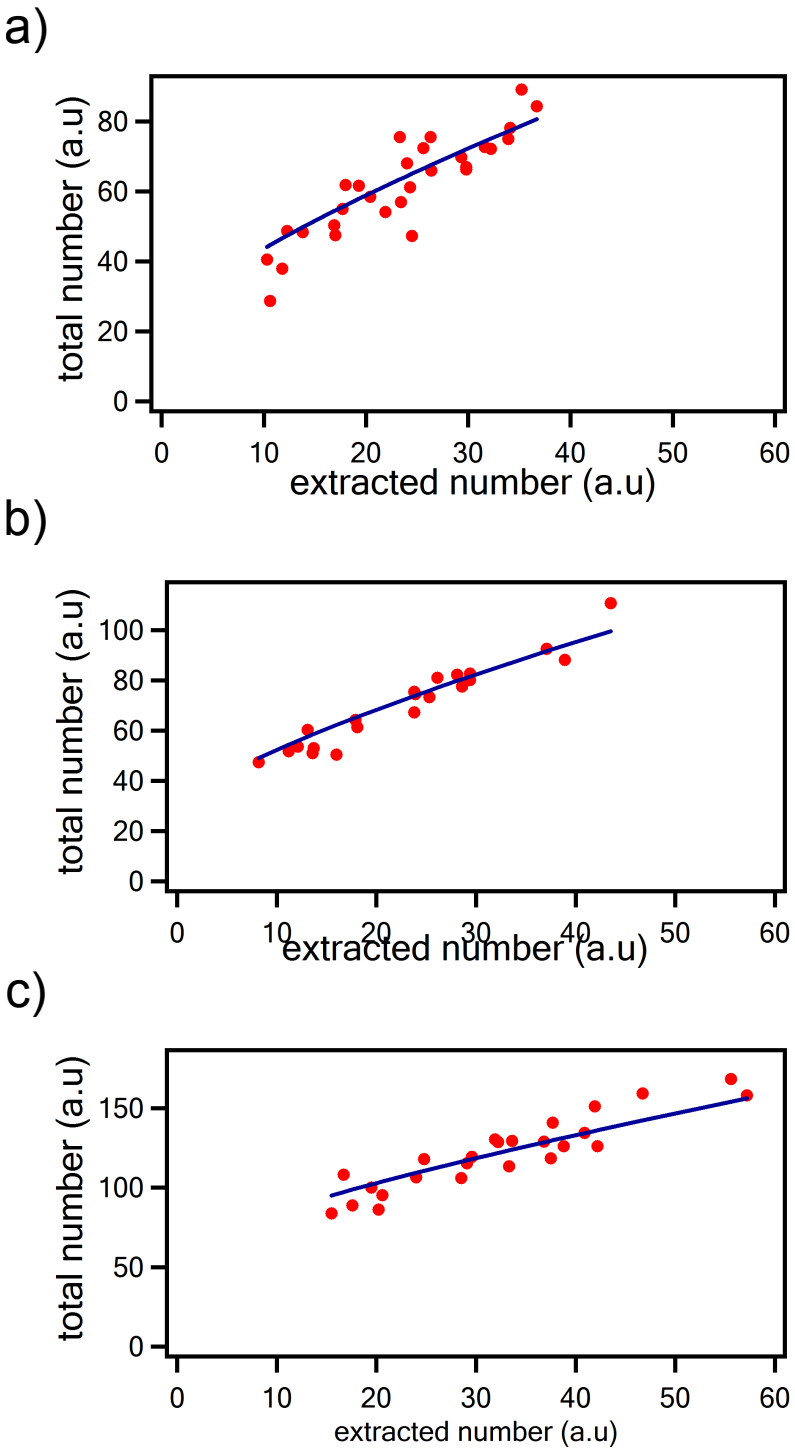

Figure 3.3: The total ion number vs the extracted number data for different initial kinetic energy. The data of a) was taken at initial kinetic energy at 8.26 K (expressed in temperature-equivalent K units), b) was at 23.26 K, and c) was at 98.26 K.

field component to provide the designed DC electric environment and the Tektronix-produced RF short pulse to induce oscillations in the UCP. Both the DC electric voltage and the pulsed voltage are applied to the same electrode, so we need to use a bias T ZFBT-4R2GW+ (Mini-Circuits) to combine the DC voltage and the short electric pulse. There is a 50 Ohm terminator at the rf input port of the bias T. At the exit port of the bias T, we used a 4 dbm attenuater to reduce the reflection. The combined signal was then sent to the electrode.

MD simulations indicated that the damping we measured was dependent on the initial kick velocity. Therefore, we needed to characterize the electric field magnitude of the short electric pulse we applied to our UCPs. If we know the voltage at the electrode, then we can use software like Simion to calculate the electric field of the pulse with sufficient precision. However, the connection to the chamber has an unknown impedance and the electrode is an open-ended configuration, so the voltage set at the function generator was not fully coupled to the electrode. Therefore, we needed to actually measure the voltage on the electrode.

To do this, we use the fact that the electrode has an open-end configuration. We can mimic this by setting the impedance of the scope to be 1 MΩ. We then attached a 10 ft. BNC cable between the function generator and the oscilloscope, which mimics those between the function generator and the chamber input port for our experimental apparatus. This long cable connection made the incident pulse and its reflection well-separated. We then send the signal to the scope to measure and integrate the voltage temporal profile. The kick voltage trace is shown in Figure. 3.4. The time integrated electric field will be $\int V(t)/(d \cdot \alpha)dt$, where d is the spacing between the electrode which is 0.019 cm and α is the correction factor from the electrode geometry. α is 3.8 as calculated from Simion. This electric field gives 6200 m/s of kick velocity for 1.7 V output from the Tektronix function generator as was used in most of our measurements.

3.5 Laser Wavelength Calibrations

As mentioned in section 3.1, we used a two-photon ionization technique to ionize the atoms. The excess energy of the ionization photons above the ionization threshold will be nearly completely transferred to the initial kinetic energy of the ionized electrons, so it is necessary to determine the wavelength of the laser in order to know the initial electron kinetic energy. The red photon is not

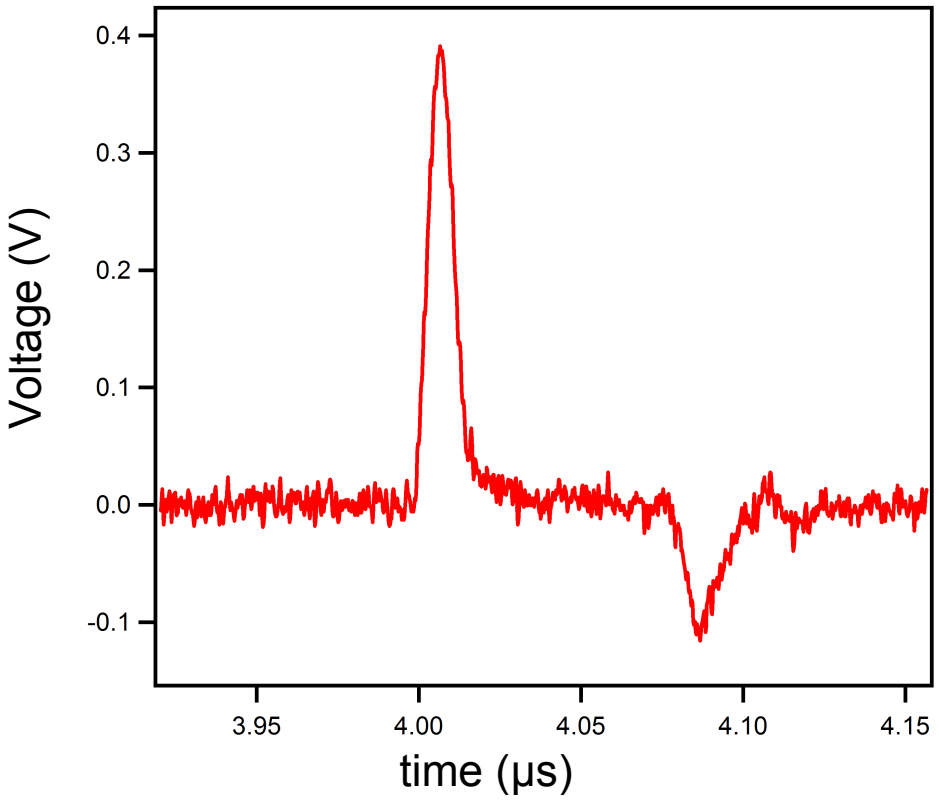

Figure 3.4: The kickpulse voltage trace from the scope. The negative dip is a real feature, but it is delayed from its actual time at the electrode by finite cable lengths. Under experimental conditions, the dip occurs under the larger positive peak.

particularly relevant to this discussion. The transfer is incoherent and so comes directly from the 5P state population regardless of how it gets there. The specification for the wavelength calibration of the pulsed dye laser used to excite the electrons from the $5P_{3/2}$ state to the continuum gives an absolute wavelength error up to 0.03 nm. This corresponds to $k_b \cdot 1.87K$ of initial kinetic energy at the threshold photoionization wavelength near 480 nm. This amount of wavelength uncertainty is not a problem when the temperature is sufficiently high, but it is a problem when the temperature is sufficiently low. Therefore we developed an *in situ* method to calibrate the wavelength of the blue dye laser.

Before getting into the details of how this calibration is performed, it is useful to discuss how our applied electric field can affect this calibration. Because there is a DC electric field applied to the atoms before they are ionized, there are shifts in the energy level near the continuum through Stark splittings. This splitting for levels near to ionization threshold will make some atoms have higher ionization thresholds and others have lower ionization thresholds depending on their l and m states. This means that even when the photon energy is below the ionization threshold, it will be able to ionize some of the atoms. For photon energy slightly higher than the ionization threshold, due to the splitting, it will not be able to ionize the entire population. This means that the DC electric field contributes a width to the range of photon energies that will ionize the atoms. In addition, there is a shift in the ionization threshold that results on average. Our calibration thus needs to be performed at as low an electric field as possible to avoid any systematic errors owing to the applied field.

To perform the calibration, we radically reduced the intensity of the laser driving the first stage of the photoionization transition. This was done so that processes such as three-body recombination are greatly reduced in order to keep the relevant physics simple. Typically, about ten thousand ions were created. Next, we measured the number of ions produced under these conditions as a function of the blue dye laser wavelength as shown in Fig. 3.3. One may note that the external electric field can reduce the ionization threshold which may shift our measurements. However, we made the calibration measurements at different electric fields around where we operate our experiments and were unable to detect any noticeable shifts. We therefore assigned the wavelength that corresponded to 50% ionization to be the threshold. Using this method, we were able to

calibrate the blue dye laser wavelength to a precision equal to $0.2k_B$ uncertainty in initial electron kinetic energy.

3.6 Using Electrode VS. Grids

There are different types of setups can be used to produce the electric field configuration needed for our experiments. In our experiments, we used a set of ring shaped electrodes similar to those used for Penning traps (see Figure 3.10 and 3.12 in Ref. [1]). The plasma is located at the center of the electrode set and by setting the voltage on those electrodes, the desired electric field can be produced. Another configuration, however, would have been to use grids rather than electrodes. The plasma is placed at the center of the grid assembly, and the electric field is generated by applying voltages to the grids. The electrode and grid setting is illustrated in Fig. 3.6.

There were several reasons why we chose to use electrodes. First, electrodes could be designed to have individual voltage control on each component, which enabled us to generate versatile electric field configurations. We originally planned to use this versatility to trap UCPs in a Penning trap. Grids would have been problematic for that in that electrons can collide with grid wires and be lost. The current electric field environment does allows us to produce the required charge imbalance for the experiment while maintaining a measurable signal size. However, that can be only achieved by configuring the electrode voltages such that a complicated electric field environment was produced. The complexity was evident from four perspectives.

First, from Simion simulations we found that instead of our desired spatially constant electric field region around the plasma, for the configurations that we had to use to get signal to the detector the magnitude of the electric field could easily vary significantly across the UCP. It could contain small spatial ripple structures, for instance. Originally, we had thought that we would be able to create a region around the UCP where there was a DC electric field that was approximately constant by adjusting potentials on the electrodes to cancel out higher-order variations. We could test the overall magnitude of the electric field, and hence get information about its variability, by measuring the UCP lifetime. This is because higher electric fields reduce the UCP lifetime by making it more difficult for the ions to contain the electrons as the UCP expands. Our optimal conditions showed, however, that the expectation that we could achieve a uniform DC electric field

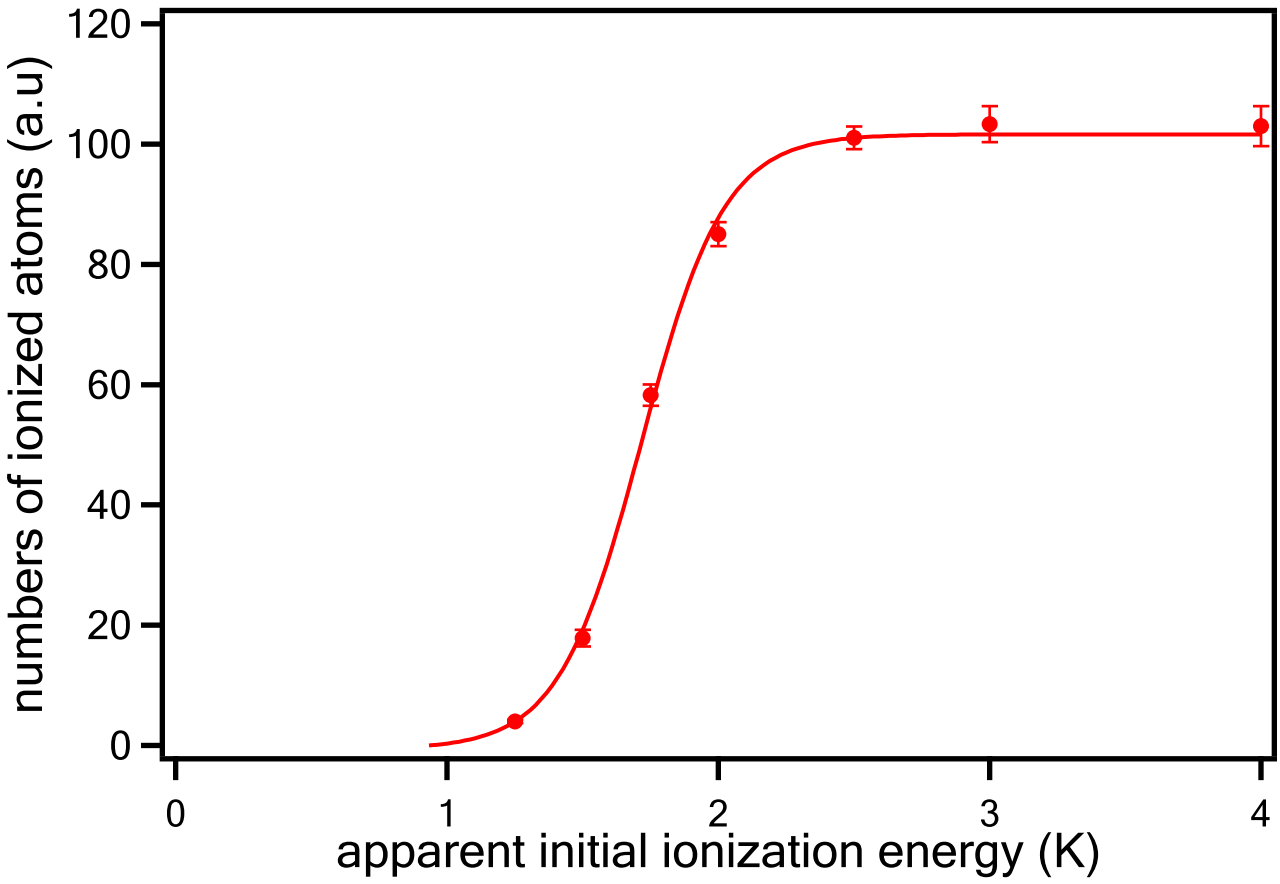

Figure 3.5: This figure shows the measured number of ionized atoms at different dye laser wavelengths determined from manufacturer's specification.

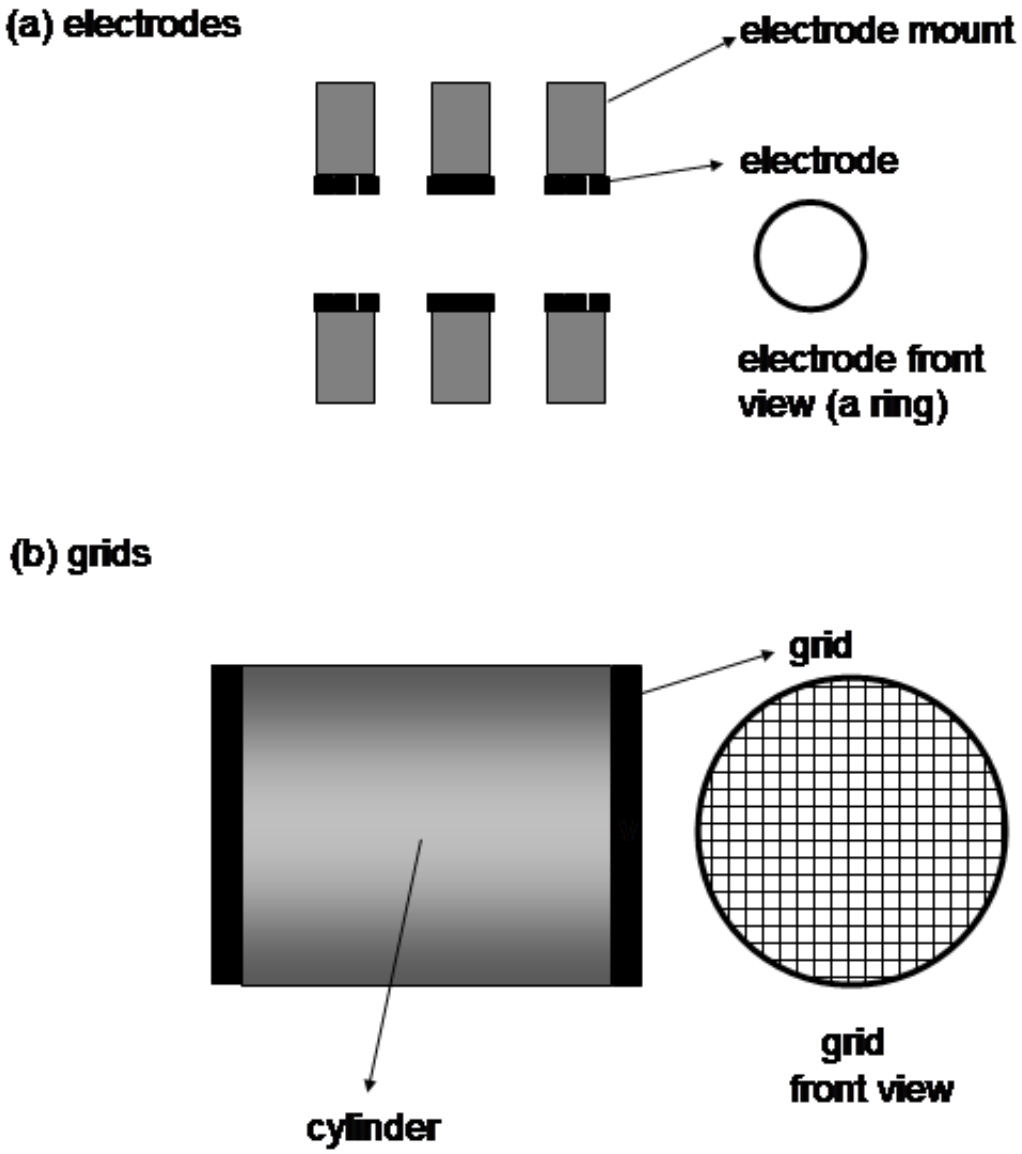

Figure 3.6: Illustration of (a) electrode setting and (b) gird setting for the experiments.

through canceling higher-order contributions was not correct. By optimizing the UCP lifetime we didn't minimize higher-order contributions but found that the contributions from different higher-order terms would roughly cancel. Thus, the magnitude of the electric field was kept low, but at the cost of spatial variation and a tendency for radical changes in magnitude just outside the UCP volume at full expansion. Since the plasma itself would screen out the external field these ripples had no effect inside the plasma. However, the electric field structure at the outer part of the plasma could be strange and complicated.

The second indication that electric field environment was more complicated than desired came after looking at the molecular dynamic simulation results modeling our UCP behavior given our measured experimental parameters [5]. We found that if we only used the DC electric field value determined from our calibration and assumed that DC electric field magnitude was unchanged through all space near the plasma region, the plasma was predicted by the simulation to be much more neutral than what was observed in the experiment. This indicated that the electric field structure was not simple.

The reason that we can't just tune the electrodes to get rid of this complicated structure is that it is possible for electrons to strike the electrodes and be lost. One of the constraints, then, is that the electrode voltages had to be configured to prevent this from happening while also making sure that the electrons that escape the UCP strike the MCP. Doing that while maintaining a small uniform DC electric field in the UCP region is difficult. This is especially true given the fact that patch charges also influence the field in the UCP region.

Given that the charge imbalance in the experiment was greater than that in the simulation, we tried to approximate the electric field as a DC field in the main region with a sharp increase in magnitude ("a cliff") outside the UCP volume. This produced some improvement in simulation/experiment agreement on this score, but it was never fully satisfactory indicating that a more detailed structure description is implied.

Fortunately, the oscillation physics and Rydberg atom physics studied and described in this thesis is sensitive only to the DC electric field in the UCP region thanks to the effective plasma screening. The calibration of the field indicated that the DC electric field is constant over the UCP. Thus, the uncertainty and complication in structure does not affect those measurements. It does,

however, affect the evaporation rate and charge imbalance – but those quantities can be measured directly and so theoretical determination of them is not necessary.

The third consideration was that of image charges. The radius of central electrode was only a few times the plasma characteristic size and the experiemnts were run at large charge imbalances. Therefore, the image charge on the electrode would have non-ignorable influence on the electric field environment in the outer part of the UCP. This can be estimated by using a infinite cylinder Greens function to calculate the potential [6]. The result shows the image charge has an effect on the order of 10 % to 20 % on the electric potential outside the UCP. This effect is smaller than other uncertainties in the electric field structure described in the section above. It does, however, add to uncertainties in the environment.

The last concern is the presence of patch charges. Patch charges on the electrode not only alter the electric field strength but also break the cylindrical symmetry of the electric field environment. The electric field created by patch charges is usually quite localized, so its effect decays rapidly with respect to the distance. Nevertheless, we did observe long-term drifts in the electric field environment that we attribute to patch charge effects. This drift could be compensated, and of all of the complicating factors patch charges were the least problematic.

All the concerns mentioned above suggest that if we want to reduce the complexity of the electric field environment around the UCP, changing from using electrodes to grids would help and in fact would address all the considerations specified above. The grid plus the outer metal vacuum apparatus can be considered roughly as a grounded cylinder with grids forming the two ends of the cylinder. This setup is a much simpler configuration than that of the electrodes, which makes the electric field determination and modeling more precise and easier. The radius of the cylindrical wall designed to hold grids is at least twice the radius of the relevant electrode as shown in Fig. 3.6. By switching from electrodes to grids, the effect from the patch charges can thus be reduced significantly. The grid setup has another advantage in that it is easier to apply a large voltage/field without worrying that the electrons will be lost on their way out of the plasma as would be the case with electrodes. This is especially helpful for Rydberg atom experiments. The larger electric field we can apply, the more deeply we can field ionize Rydberg atoms, which will be helpful for understanding the Rydberg formation processes and examining the Rydberg atoms formation rate.

Though the grids setup has these advantages, there are also potential drawbacks. First, Penning trap designs are the typical way to trap opposite sign charges simultaneously [7]. Therefore, it may be rather difficult, if not impossible, to trap both electrons and ions for a much longer time as compared to the natural life time of the UCP. The other drawback is that under the current electrode setup, we were able to reach a charge imbalance less than 50 % while still having a measurable signal size for experiments whose signals consist of small numbers of extracted electrons. For a simpler electric field environment, a 50 % or less charge imbalance is likely too deep for electrons to escape completely from the UCP. That means a more exotic electric field time sequence will be needed to conduct variety of UCP measurements. Taking the two pulse measurement for illustration, under the current electrode configuration it was possible to apply one pulse to initiate the oscillation and a second to modify the amplitude of the oscillation. Electrons were able to escape after the second pulse. With grids, at a 50% UCP charge imbalance it is not likely that electrons will be able to escape after the second pulse. Thus, another pulse will have to be added that will allow the higher-energy electrons that are produced as a result of the second pulse to escape. These design problems will be investigated in the future.

References

[1] T. M. Wilson, Dynamics of low-density ultracold plasmas in externally applied electric and magnetic fields, Ph.D. Dissertation (Colorado State University, 2013).

[2] S. Chu, Rev. Mod. Phys. **70**, 685 (1998); C. N. Cohen-Tannoudji, ibid. **70**, 707 (1998); W. D. Phillips, ibid. **70**, 721 (1998).

[3] T. C. Killian, S. Kulin, S. D. Bergeson, L. A. Orozco, C. Orzel, and S. L. Rolston, Phys. Rev. Lett. **83**, 4776 (1999).

[4] Wenhui Li *et al.*, Phys. Rev. A **70**, 042713 (2004).

[5] Craig Witte, *Computational Modeling of Low-density Ultracold Plasmas*, Ph.D. Dissertation (Colorado State University, 2017).

[6] J. A. Hernandes and A. K. T. Assis, J. Electrostatics **63**, 1115 (2005).

[7] G. B. Andresen *et al.*, Nature **468**, 673 (2010).

Chapter 4

The Measurement of Electron Center-of-mass Damping in Ultracold Plasmas: General Introduction to The Technique And Collisionless Damping

One of the fundamental features of a plasma is the existence of electron plasma oscillations. These oscillations are a hallmark of collective effects and set the fundamental timescale for electron dynamics in the plasma. The plasma oscillation frequency as shown in Eq 2.3 is determined largely by the plasma density and fundamental constants for cold electron plasmas. Although there is some temperature sensitivity for shorter wavelength oscillations too, as seen by the finite-temperature dispersion relation [1]

$$\omega^2 = \omega_p^2 + \frac{3k_bT_e}{m_e}k^2, \tag{4.1}$$

where ω is the angular frequency of the electric field, ω_p is the cold plasma frequency defined in Eq. (2.3), k_b is the Boltzmann constant, T_e is the electron temperature, and k is the wave number.

In addition to the oscillation frequency, plasma oscillations have a damping rate as well. This damping can be primarily collisional in nature through electron-ion collisions. For other parameters, it can be primarily collisionless in nature, most notably through Landau damping [2]. In addition, there are other collisionless effects such as plasma oscillation echos and mode coupling between Tonks-Dattner modes in non-uniform density plasmas that can influence the oscillation amplitude as a function of time [3–5]. The work presented in this chapter focuses on experimental and associated theoretical studies on the primary nature (collisional or collisionless) and rate of plasma oscillation damping in ultracold plasmas.

Ultracold plasmas (UCPs) represent a useful system in which to study electron oscillations. These plasmas are created through the photoionization of either ultracold atoms or molecules in beams [6, 7]. Many plasma oscillation experimental results have been reported in UCPs, focusing on the resonant oscillation response [5, 8]. In contrast to the oscillation frequency, the damping rate of plasma oscillations in UCPs has not been studied extensively. In the experiments of Ref. [9], it was initially observed that particular electron plasma oscillations in a relatively low-density

UCP parameter regime did indeed damp with time, but a systematic study of the damping rate was not conducted. In the work described in this chapter, we used a combination of theoretical and experimental techniques to investigate the behavior of the electron center-of-mass (CM) oscillation damping in UCPs.

4.1 Theoretical Model

When we apply a short electric pulse to a UCP, it will initiate a electron center-of-mass (CM) oscillation, as illustrated in Fig. 4.1. This manifests itself as an oscillation of the electron center of mass around the ion center of mass in the ultracold plasma. The oscillation will damp away over time. To theoretically investigate the electron CM damping in the UCP, we developed a computational model to match the experimental conditions to study the damping-related physics. The computational model consisted of several parts. First, to avoid dealing with the creation of bound states between electrons and ions, the ions were treated as a smoothed continuous and stationary charge distribution with Gaussian density profile, $n = n_i e^{-r^2/2\sigma^2}$, where n_i is the peak ion density, r is the distance to the origin, and σ characterizes the spatial extent of the ions.

Second, the $e^- - e^-$ interaction was calculated through a full molecular dynamic simulation. Individual forces between all the electrons were calculated at each timestep in the simulation and the electron velocities and then positions are adjusted accordingly. MD simulation of the normal Coulomb potential $1/r$ can often require very small time steps to deal with some particles which have very small closest distances of approach. This greatly increases the calculation load and thus increases the necessary running time. In order to increase computation speed, we used a softened Coulomb potential $1/\sqrt{r^2+\alpha^2}$ instead of $1/r$, where α is the softening parameter. We tested the outcome of simulations using different α, and then worked in the regime where the damping rate was insensitive to the value of α.

Third, the e^--ion collisions were modeled by using a Monte-Carlo (MC) collision operator. In this collisional operator treatment, we assume the ions have infinite mass and are stationary. Several other standard "textbook" approximations were assumed as well, including the binary collision approximation, a cut-off of collision impact parameters, and the normal practice of pulling the Coulomb logarithm out of collision integrals by replacing velocity terms with the electron tem-

perature instead. Collisions occur randomly with random impact parameters in our model. The probability of the collision in any time step is $n\pi\lambda^2 vdt$, where, n is density, λ is the cut-off parameter, v is the velocity of the particles, and dt is the time step. The cut-off parameters, which were on the order of Debye length, were adjusted such that results matched the prediction from standard stopping power models such as the BPS model [10]. Once a collision occurs, an impact parameter less than λ was randomly chosen and the velocity of the electron was deflected by the amount determined by Rutherford Scattering. In performing the computation required in our model, we used the OpenCL standard to utilize the massively parallel architecture of modern Graphic Processing Units (GPUs). GPU programming offers enormous speed increases over traditional CPU-based programming, allowing for every single electron in the experimental system to be modeled individually. For more details on modeling and GPU calculation, please refer to [11].

The division of electron-ion Coulomb interactions into a long range interaction that confines the electrons in the UCP and into binary collisions allows for probing of the underlying physics of electron-ion interactions in the UCPs. By running simulations with and without electron-ion binary collisions, it is possible to quantify the effect that binary collisions have on the collective motion of electrons in the UCP. This also makes it possible to test different theories on the extension of weak-coupling collisional treatments that are suitable for the strong coupling regime against experimental measurements. For more about this last point, see chapter 5.

4.2 Model Results

The damping of the CM oscillation could be primarily collisional or collisionless or a combination of both. For collisional damping, the damping would result from electron-ion collisions. Note that $e^- - e^-$ collisions have no effect on this damping because they result from internal force that cannot influence the center-of-mass motion. One would expect in a uniform-density ion cloud that the damping of the CM oscillation would damp as a function only of the electron-ion collision rate. For uniform-density ions, the trapping electric field is linear with respect to the distance to the center of the plasma (i.e. it is a harmonic trapping potential). Indeed, if the collision is turned off in the simulation, we see no damping of the CM oscillation for uniform density cases. Under a

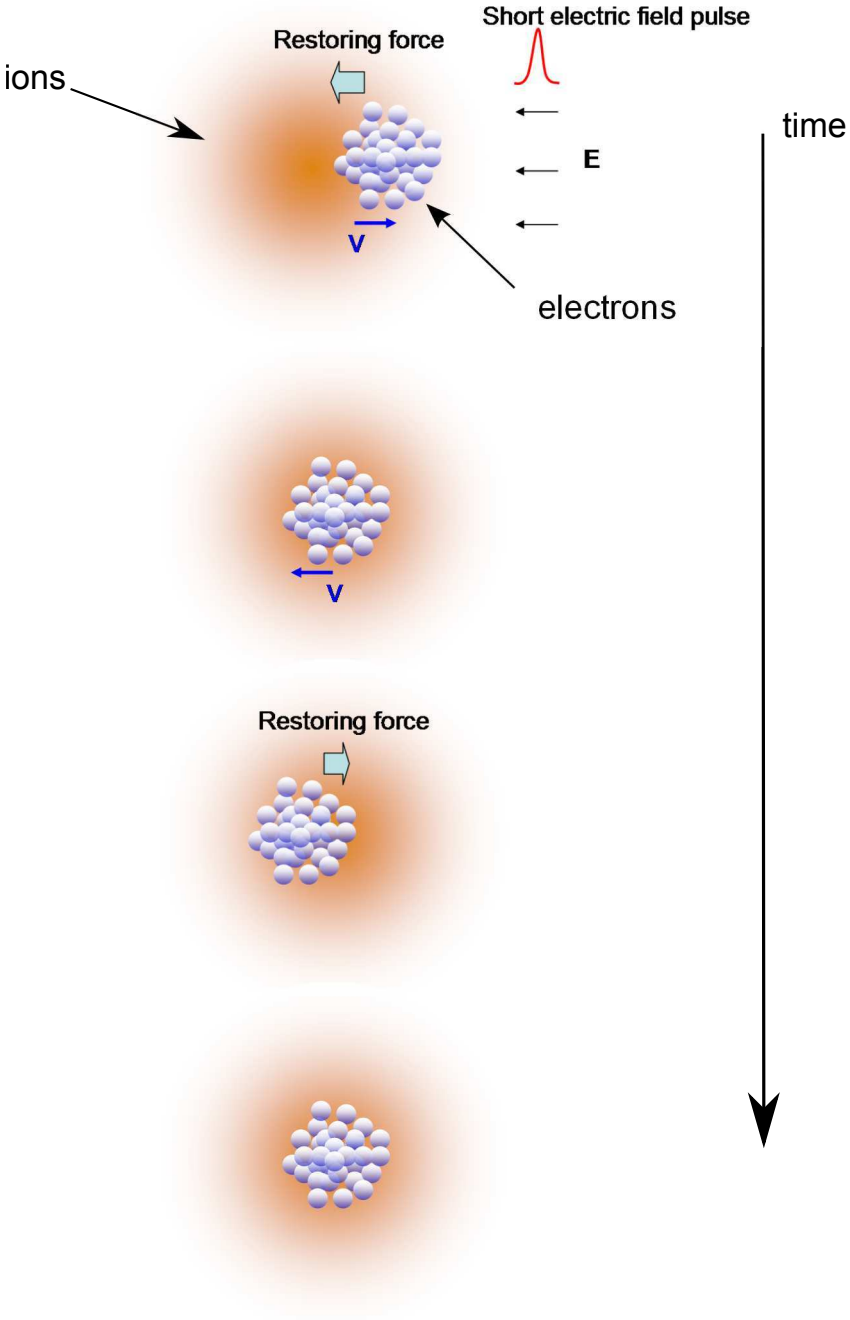

Figure 4.1: Illustration of CM motion initiated by applying a short electric field pulse. The electron cloud will oscillate and and that oscillation will damp with time.

harmonic potential, the oscillation phases between particles are maintained regardless of oscillation amplitude so the CM oscillation will not damp as long as there are no electron-ion collisions.

For collisionless damping, the main source of decrease in the oscillation amplitude comes from depahsing due to the anharmonicity of the ion trapping potential. The anharmonicity is a result of the inhomogeneous density profile. For our experiments, the ions in UCPs have a Gaussian spatial density distribution, therefore the trapping potential is not a harmonic one. The degree of anharmonicity depends on the spatial extent and distribution of the electrons. With anhrmonicity, shape oscillations in addition to the CM oscillation can occur. These shape oscillations in turn couple back to the CM oscillation through changes in the electron spatial distribution combined with the anharmonic confining potential. This can lead to an apparent damping of the CM oscillation as the net amplitude decreases with time, at least for the initial few plasma periods. The amplitude decrease is effectively due to mode coupling between the shape and CM oscillation modes. Amplitude collapse and revivals were observed numerically which means that the oscillation amplitude decrease was not purely dissipative. Fig. 4.2 shows a mixture of an overall damping and a partial collapse and revival. This is an indication of mode coupling occurring during the electron CM oscillation.

At this point, it is tempting to compare the decay of electron CM oscillation to a damped simple harmonic oscillator, $m\ddot{x} + \nu\dot{x} + kx = 0$, where m is the mass of the particle, ν is the damping rate, and k is the spring constant. For a damped harmonic oscillator, the damping is an energy dissipation process, and the damping rate of the oscillation is $\nu/2$. The parameter ν can be derived for electrons in a plasma from stopping power formula found in the literature [12]. We originally thought we could model CM oscillation damping in a UCP using a simple harmonic oscillator model. Unlike in a damped single harmonic oscillator case, the measurement of electron CM oscillation usually involves a combination of different mechanisms. If the damping is dominated by electron-ion collisions, the damping rate is a measure of momentum transfer rate as mentioned in chapter 2. If collisions are negligible, the damping measures the dephasing and coupling between different modes of the CM motion. This means that the relation between CM oscillation damping rate and the momentum transfer rate is not a simple factor as in the simple harmonic oscillator case presented above, and hence there's no direct comparison or translation between the theoretical

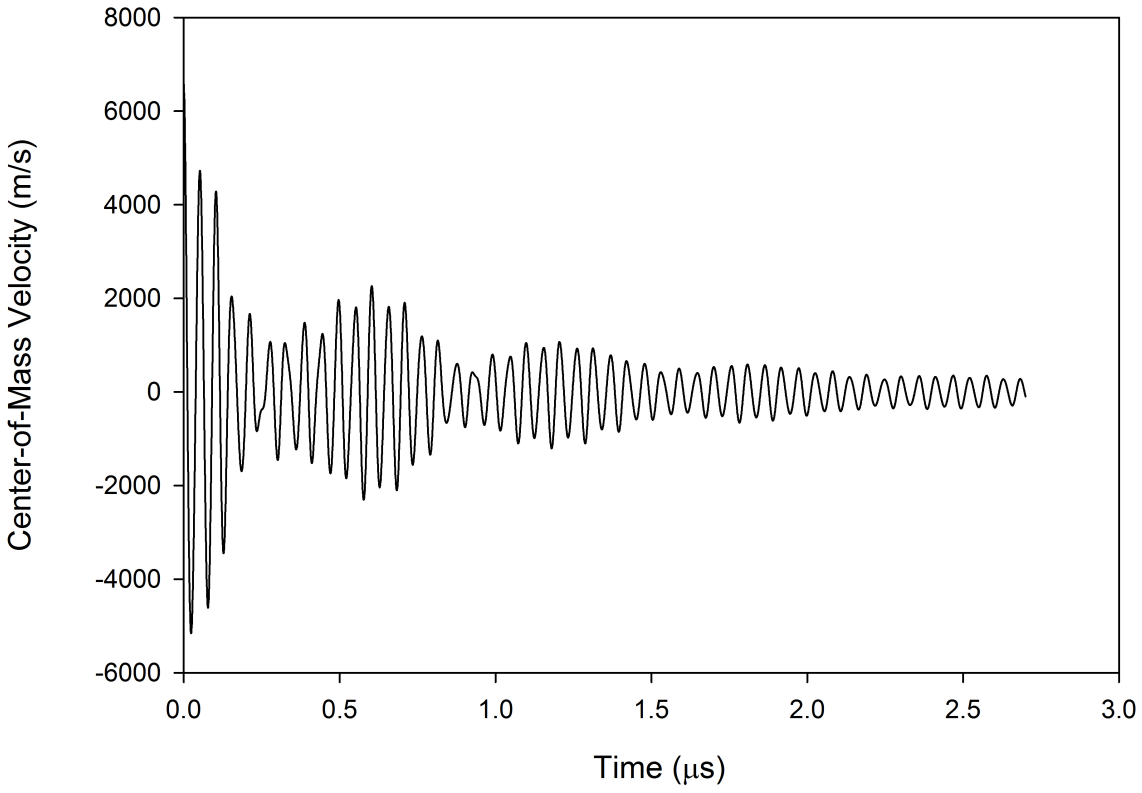

Figure 4.2: UCP electron CM velocity in the z direction as a function of time, in the absence of electron-ion collisions. Plasma parameters for the simulation mirrored experimental conditions for $T_e = 3K$ with $\delta = 0.45$. The ion numbers was 200,000, and the applied DC electric field was 7 V/m. The figure illustrates partial collapse and revival, and suggests coupling to modes.

expressions and our measurement. Therefore more serious modeling work was needed to interpret our data.

The ion trapping potential of UCP is close to a harmonic one around the center of the plasma and becomes more anharmonic with increasing distance away from the center. This does present an opportunity to try to minimize the influence of collisionless (i.e. anharmonic) damping. One would expect that this anharmonic damping will depend on both the charge imbalance $\delta = (N_i - N_e)/N_i$ of the UCP and the applied external electric field on the UCP, where N_i and N_e are the ion and electron numbers in UCP. For a UCP with a larger charge imbalance, the electrons are concentrated around the center region of the UCP, so the trapping potential seen by electrons inside the plasma is more harmonic than a more neutral UCP whose extent covers more volume of anharmoic portion of the potential. Therefore, we will expect the anharmonic damping to be less significant for larger charge imbalances. Another way to look at this is that in the limit of $N_i \gg N_e$, the UCP electron and ion density approach the uniform case. As shown in Figure. 4.3, the damping rate decreased with the increase of charge imbalance and eventually plateaued as expected. We interpret this as a strong indication that anharmonic effects are indeed responsible for significant damping in UCPs for many different conditions. This was confirmed by performing simulations assuming uniform-density ion distributions.

The presence of an applied external electric field will push the plasma electrons away from the center, so a larger external electric field will also make the plasma electrons see the more anharmonic part of the potential, which will enhance the contribution from the anharmonic damping. We ran simulations for the oscillation damping rate vs an applied electric field for several temperatures, and saw the damping rate increased with the applied electric field as shown in Fig. 4.4.

In our experiments, a 9 G magnetic field in the direction of the applied electric field was introduced to better guide the escaping electrons from the plasma to the detector. Therefore, we investigated the impact that a magnetic has a on the electron CM oscillations as well. Simulations, at variety of different temperatures, were run with a uniform magnetic field oriented along the direction of electron oscillation.

In a collisionally dominated regime, the addition of such a magnetic field would not be expected to have any significant impact on the electron CM motion given that the typical electron Larmor radius is greater than Debye screening length [13]. This was checked and verified by simulation.

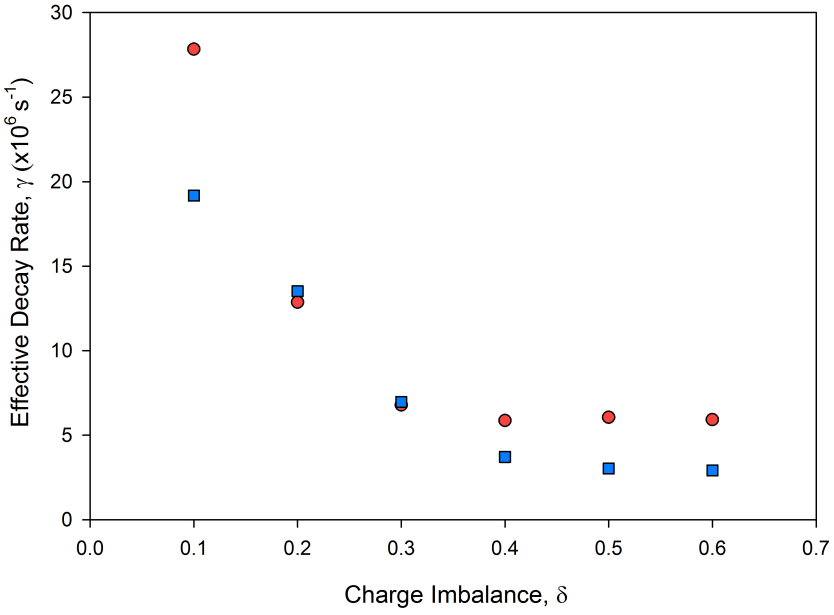

Figure 4.3: The impact of charge imbalance δ on the effective damping rate, γ. Simulations where run with 20,000 ions, and an appropriate number of electrons as defined by δ. No DC electric field was applied, and electron-ion collisions were included in the calculation. The electron temperature was 3 K for red circles and 15 K for blue squares. To extract γ, a damped sinusoid was fit to the first five oscillations of the CM motion. The figure shows the sharp increase in γ as the UCP becomes more neutral.

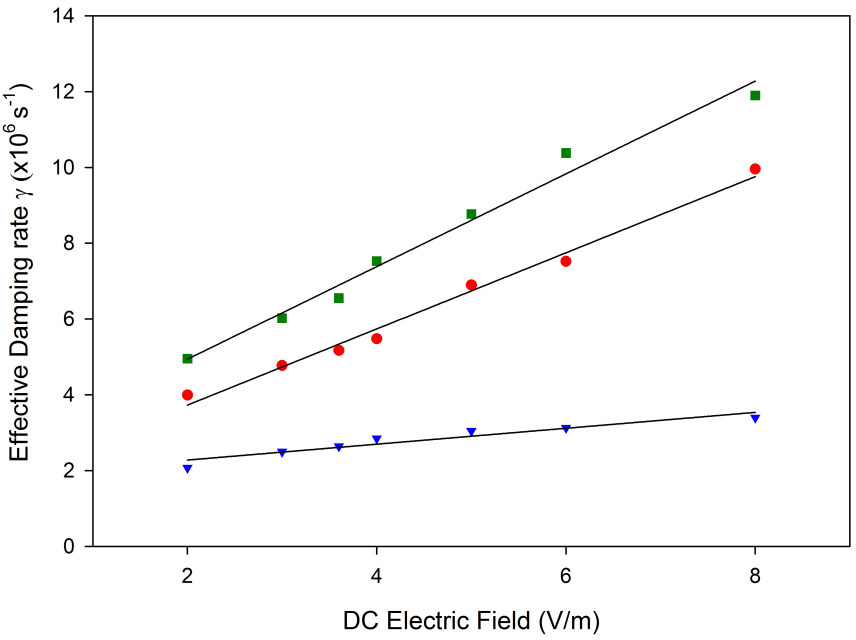

Figure 4.4: Effective damping rate γ, vs. applied DC electric field for three different electron temperatures(green square, 3K, red circle, 6K, and blue triangle, 15K). In this calculation, electron-ion collisions were included. The charge imbalance δ was 0.45, and the ion number was 200,000. The damping rate increases with an increase of applied DC electric field, and decreases with increasing electron temperature.

However, in a collisionless damping dominated parameter regime, we suspect that the magnetic field would have an effect, since the Larmor frequency at a 9 G magnetic field is 25.2 MHz which is greater than the plasma frequency which was about 17 MHz for the conditions that we studied experimentally. Examples of the impact of that an applied magnetic field has on the electron oscillation can be seen in Figure. 4.5. While a magnetic field does not add any qualitatively new physics, it shows that the addition of a magnetic field results in an observable change in the electron oscillation. The reduction is consistent with the expectation that the presence of the magnetic field will reduce the extent of shape oscillations.

4.3 Experiemnts

While our modeling elucidated many details about the physics of collisionless influences on electron CM oscillation damping, a natural question is how the model predictions compare with experimental measurements. The UCPs used in our experiment were created by photoionizing ^{85}Rb cold atoms. Details for creating the UCPs for our experiments are described in Chap. 3 and Ref. [14]. A DC electric field with an average value of 4.1 V/m was applied to the plasma for extracting and guiding the escaped electrons. This value of the electric field was determined by assuming a spatially constant field E_0 and a linear field $E_1 z$, where z is the axial coordinate (i.e. the coordinate along the direction of the applied field) describing the electric field in the region of the UCP. The value of E_0, and E_1 were adjusted to match both parameters to both the potential depth calculated from a modified version of the evaporation model in Ref. [15] and the electric field calibration data described in Chap. 3. Matching two different properties (plasma potential depth and plasma threshold number) allowed a unique determination of the two field parameters. We needed to include both parameters to have a reasonable model of our electric field as applied to our UCPs. To calculate the trapping potential, we need to know the parameter η which represents the ratio of the trapping potential energy depth to $k_b T$. After η was determined, we then know the trapping depth based on our determination of the electron temperature as described below. The estimation of η is discussed in the evaporative cooling part later in Sec. 4.5. Because we use electrodes to produce the required electric field (see section 3.5), there is the possibility of substantial spatial variation in the electric field across the UCP. For the measurements for this section, the axial

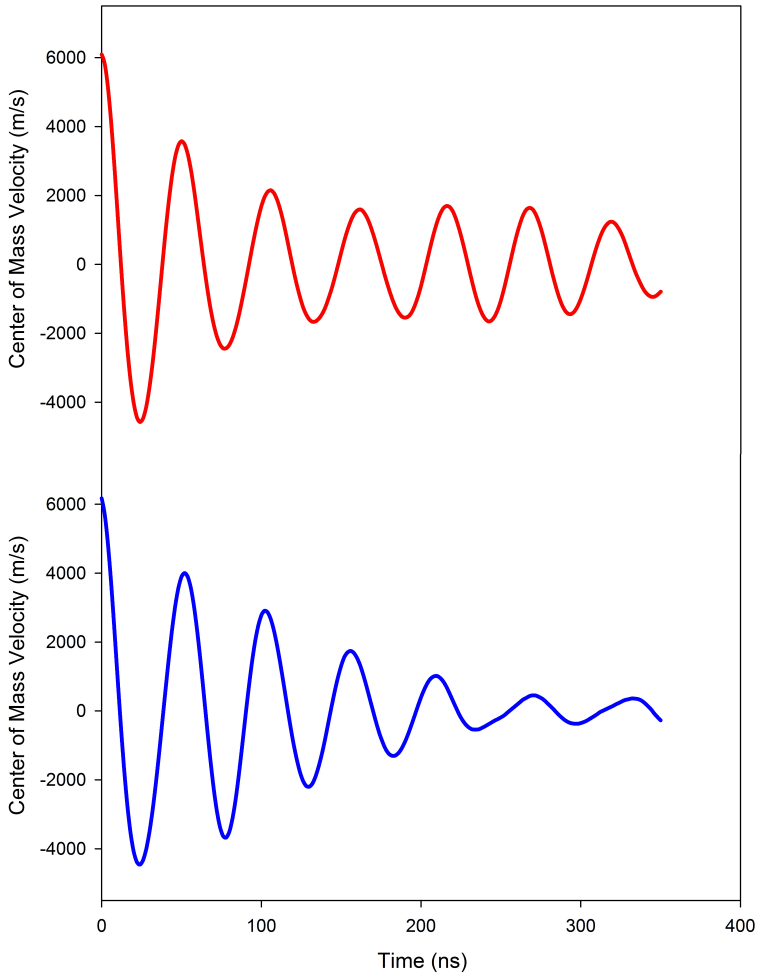

Figure 4.5: UCP electron center-of-mass velocities in the axial direction as a function of time from two different simulations. The simulation at the top incorporated a 9G uniform magnetic field pointing in the axial direction, while the bottom simulation did not include any magnetic field. Otherwise both simulations were identical, with $T_e = 2.86K$, $\delta = 0.55$ and 200,000 ions.

electric field component varied from 0 V/m to 9 V/m across the UCP spatial extent. Our model indicated that this variation did not affect the damping rate qualitatively (although as mentioned before it was influenced by the average electric field), and the variation was included in all of our model calculations that were compared to the experiment.

To produce and measure electron oscillations, we applied two short electric pulses to the UCP starting 3 μs (8 ns FWHM) after formation. The time between the two pulses was varied deliberately as part of our measurement technique. The first pulse had a field of 3 V/m and initiated the electron CM oscillation. The second pulse modified the oscillation. CM motion of the electrons produced internal oscillating electric fields that drove electrons with proper velocity and position out of the UCP [14]. The number of the electrons driven out of the UCP depends on the amplitude of the oscillation. If the second pulse is timed such that it produced an acceleration in phase with the electron motion, then the oscillation amplitude would increase and the number of electrons that escaped from the plasma would thus also increase. If the second pulse is timed so that it was applied out of the phase with the electron motion, then the oscillation amplitude would decrease, and so fewer electrons would escape. The number of escaped electrons that resulted from the application of the second pulse was thus an indication of the amplitude of CM motion. By varying the delay time of the second pulse, we could obtain the temporal profile of the electron CM oscillation, and then extract a decay time from the measured profile.

In using our two-pulse technique, we assume that the electron escape signal generated by the two pulses scales linearly with the amplitude of the CM motion of the electrons. We checked this assumption in three different ways that each confirmed a linear scaling. First, we performed numerical modeling of the plasma, using the model described above, in response to a two-pulse sequence. We then compared the variation of the escape and the amplitude of electron CM motion and found a linear scaling. Our second test involved measuring the electron escape response at the resonant frequency as a function of the amplitude of an applied two-cycle RF electric field pulse [14]. The measured results are shown in Fig. 4.6. The RF pulse does not accelerate loosely bound electrons out of the UCP as easily as a single pulse. Therefore, the total electron escape from the RF pulse is more akin to the late-time (i.e. post-initial oscillation) data from the two-pulse measurement. We found that the electron escape signal varied linearly with the applied field, again indicating a linear response. Finally, in the model, we followed the individual electrons that

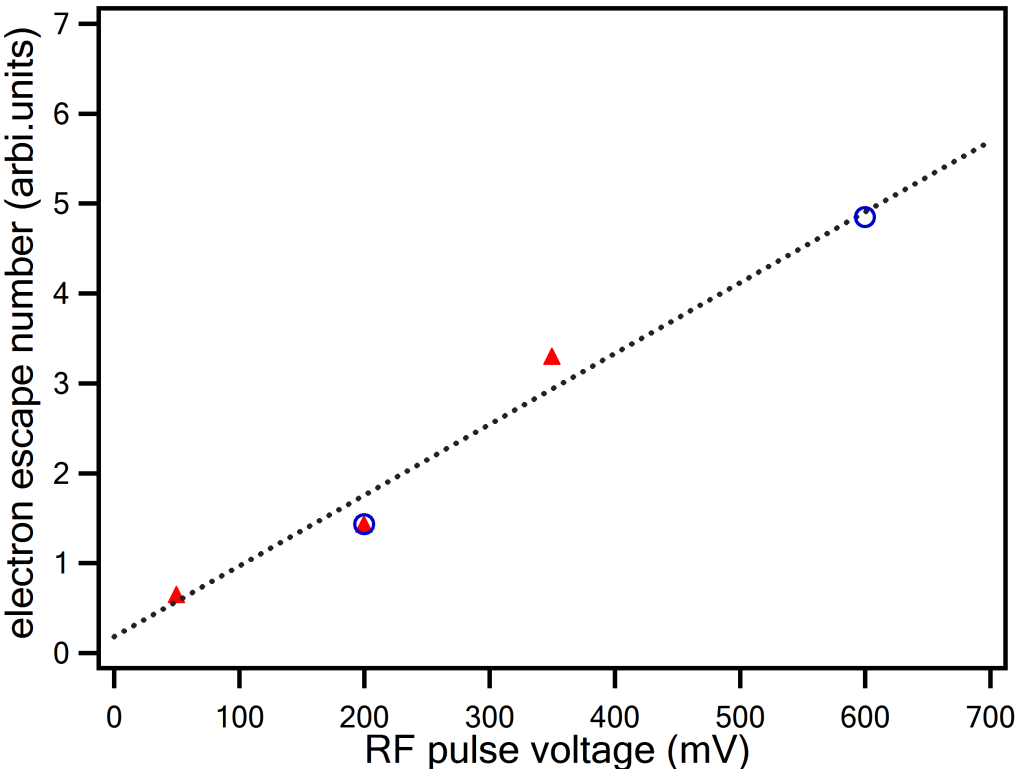

Figure 4.6: Electron escape response at the resonant frequency at different RF amplitudes. The red triangles and the blue circles are different set of measurements. The value of the blue data is scaled to match the red triangle 200 mV data.

escaped due to the oscillation, and found that the fields that accelerated them were consist with linear scaling of escape rate and the amplitude of CM motion.

The very first experimental two-pulse oscillation damping trials were conducted at the initial electron kinetic energy divided by $k_B$of 3.26 K, 8.26 K, 23.26 K, 48.26 K, 198.26 K, 298.26 K, and 498.26 K. While the photo-ionization imparts a particular kinetic energy to each ionized electron, it is easier to work in temperature-equivalent units, hence the k_b factors in the specification. The typical ion numbers were about 380,000 ions, with σ of 800 μm. The data were fit to an exponential decaying cosine function, as illustrated in Fig. 4.7. There were some higher energy electrons that were directly driven out by the applied electric pulse itself instead of the internal fields from the oscillation. Those electrons were mixed with electrons driven out by the CM motion, so we started the fit around the second peak (the peak around 50 ns) to avoid complications. The decay rates are shown in Figure. 4.8. The first observation of the data showed dependence on the initial kinetic energy which in turn strongly related to electron temperature. To see if the observed damping rates are from electron-ion collisions, we calculated some order of magnitude estimates of collisional damping rates. To do so, the temperature of the UCP can be roughly estimated by setting the initial electron temperature to be $T_e = 2/3 \cdot k_b \cdot$ (initial kinetic energy), and using a self-similar expansion model (described in 2.4.2) to estimate the temperature of UCP at 3 μs. Using estimated temperatures, we can calculate the collisional damping rate ν from stopping power results in the low projectile velocity limit [12], and use $\nu/2$ as an estimated oscillation damping rate. The comparison of the measured damping rate and estimated damping rate is shown in Figure. 4.8. We observed that except for the coldest initial kinetic energy data, the measured damping rates are one to two orders of magnitude higher than the collisional damping rate. This much higher measured damping rates is a strong indication of the existence of a substantial collisionless effect, and for an initial kinetic energy greater than 50 K, the damping is nearly completely collisionless.

We conducted further initial investigations by examining the damping rate vs. the UCP charge imbalance. Fig. 4.9 shows the damping rate at different charge imbalances at initial kinetic energy of 298.26 K. It suggests that a larger charge imbalance could have the effect of reducing the measured damping rate as described in previous section, although admittedly the error bars are large enough that the any effect is not well-resolved.

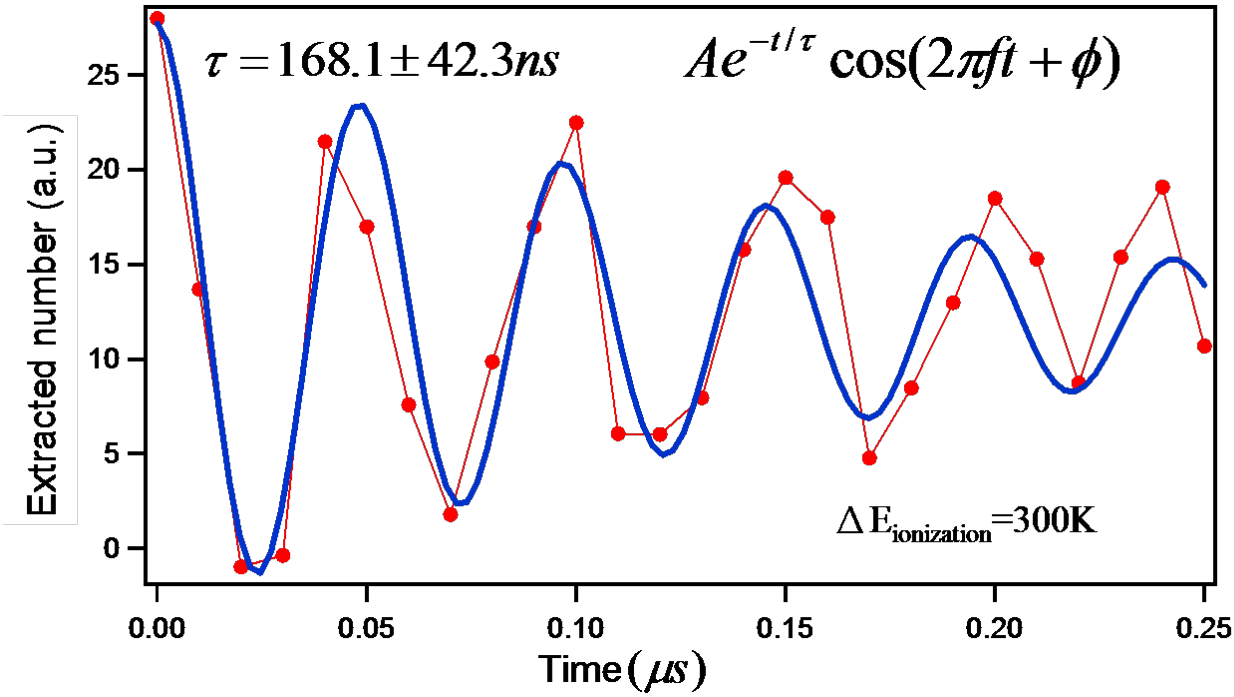

Figure 4.7: An illustration of fitting the data with a damped cosine function.

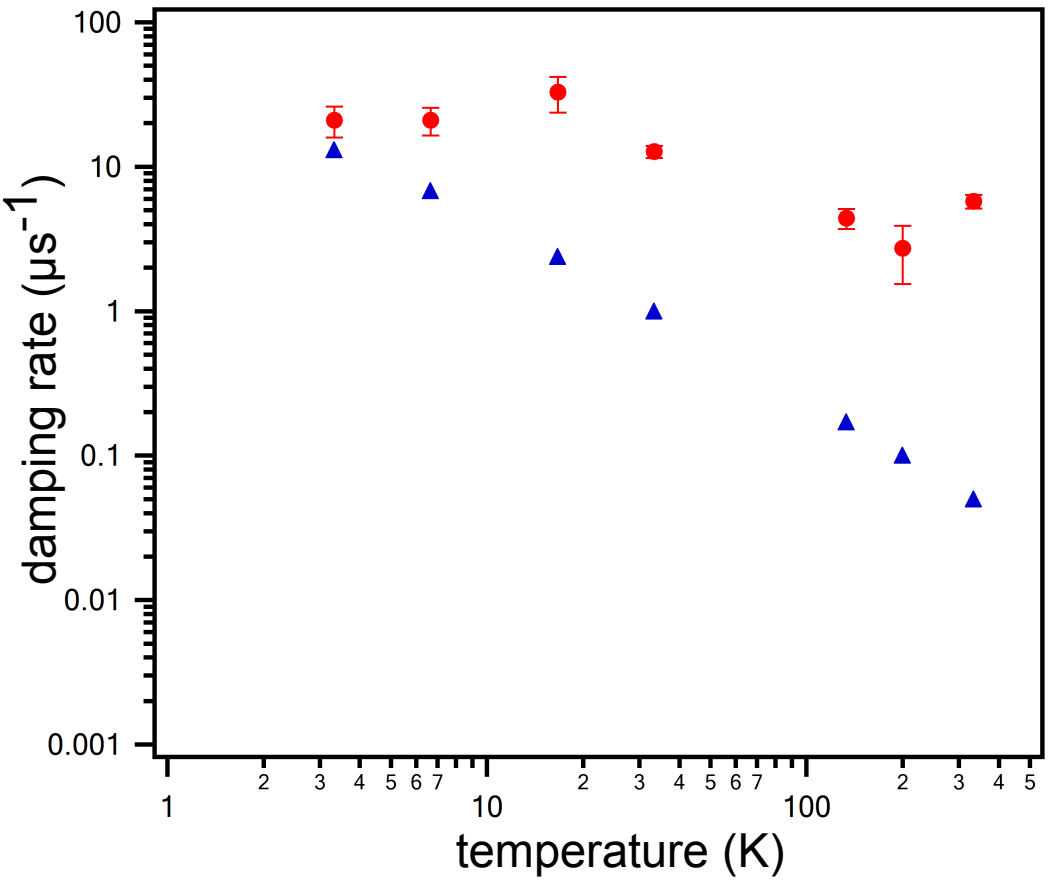

Figure 4.8: Comparison of measured damping rates (red circles) to predicted damping rates estimated from electron-ion collision rates (blue triangles). See the main text for the details of the comparison. The measured rates are clearly well in excess of those estimated from electron-ion collision rates. Note that the axes are logarithmic.

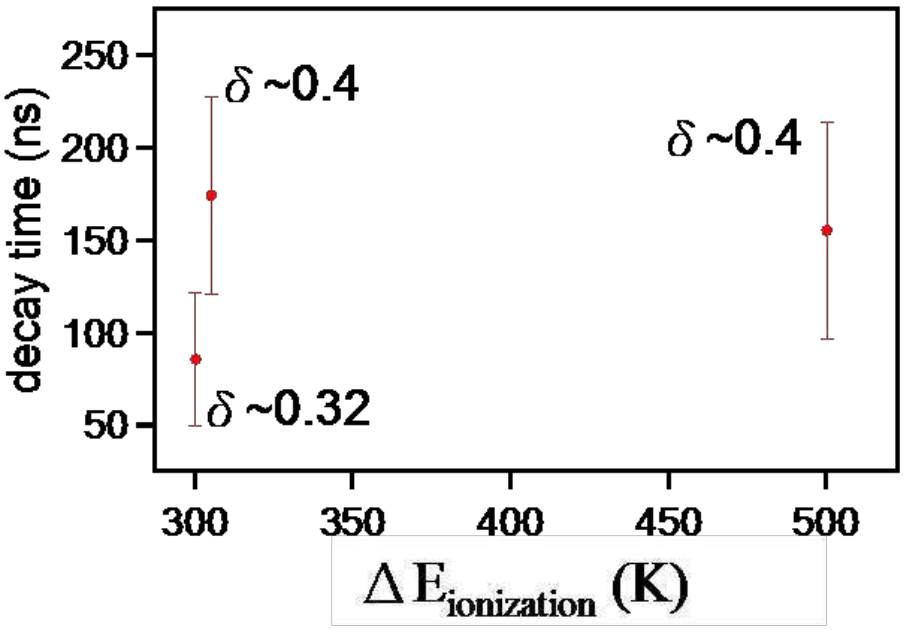

Figure 4.9: Measured decay time at different charge imbalance at 300 K. $\delta = \frac{N_{ion}-N_e}{N_{ion}}$ where $N_{ion,e}$ refer to the ion and electron number, respectively. The larger charge imbalance data shows a longer decay time.

With the guidance of the preliminary results in the first trial, we decided to reduce the number of electrons and ions in the UCPs to produce a larger charge imbalance. We performed these more refined measurements at average initial electron kinetic energy of 3.26 K $\cdot k_b$, 8.26 K$\cdot k_b$, and 23.26 K$\cdot k_b$, where k_b is the Boltzmann constant. The experimental data are shown in Figure 4.11. From such data, we can extract both the damping rate and the oscillation frequency. Since the CM oscillation frequency is density dependent (as shown in Fig. 4.10), we can calculate the average density from the frequency. The charge imbalance and the total ion number are known so we could measure the size of the plasma σ at the time of the two pulse measurement as well. Simulations showed that for our conditions, a correction was needed in determining the density as compared to the method in Ref. [9], and so we applied this correction in our data analysis.

To interpret the data, we need to estimate the plasma electron temperature. The temperature was expected to be the net result of several heating and cooling mechanisms such that the electron temperature T_e was a sum of several contributions.

$$\begin{aligned} T_e &= \Delta T_{ionize} + \Delta T_{dih} + \Delta T_{cont} + \Delta T_{3bd} \\ &\quad -\Delta T_{ad} - \Delta T_{evp} \end{aligned} \tag{4.2}$$

where T_e is the electron temperature and k_b is Boltzmann constant.

The first term ΔT_{ionize} is the initial kinetic energy converted from excess ionization photon energy. The second term ΔT_{dih} is the contribution given by disorder induced heating [16]. Disorder induced heating comes from the conversion of the correlation energy of the initially disordered electrons to their kinetic energy as they reach a more ordered state. The amount of heating was estimated by the formula [17, 18]

$$T_f \simeq \frac{2}{3}\frac{e^2}{a}\left|\frac{u}{\Gamma} + \frac{\kappa}{2}\right| \tag{4.3}$$

where e is the electron charge, a is the Wigner-Seitz radius, u is internal energy per particle, Γ is strong coupling parameter, and κ is a/λ_D, where λ_D is the Debye Screening length.

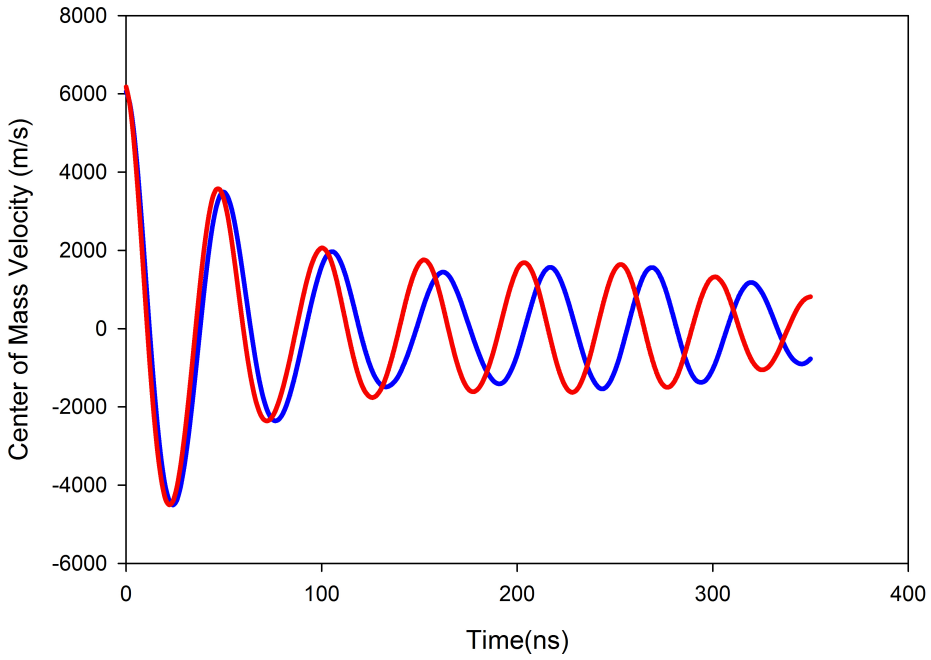

Figure 4.10: Illustration of the density dependence of the electron CM oscillation. The density of the blue line is 10% less than the red line, and we can observe that the blue line has a smaller oscillation frequency.

During plasma formation, the electrons are not fully in thermal equilibrium. Therefore, we used a dynamic screening length from Ref. [19] for approximation. By using tabulated value from Ref. [18], we estimate about 0.02K of disorder induced heating for our conditions.

To estimate the contribution of heating from continuum lowering [20] ΔT_{cont}, a molecular dynamic simulation was needed since the electrons were not created in thermal equilibrium. We thus took the molecular dynamic simulation which calculated continuum lowering from Ref.[20] and scaled it to our experimental conditions. Doing so, we found 0.8 K heating contribution from continuum lowering.

Heating from three-body recombination ΔT_{3bd} is expected in our UCPs. Using the three-body recombination rate from the literature [21, 22] and assuming each event results in energy increase equals to the bottleneck energy of about $3k_b$T [23], we can estimate the electron temperature increase from three body recombination. This heating was found significant only in the lowest temperature data that were collected. For those data, three body recombination was predicted to lead to a 6.1 % increase in the electron temperature.

The adiabatic cooling ΔT_{ad} due to the expansion of UCP was ignorable, because we took the measurement soon after formation, and so the size did not have time to change significantly. We confirmed this was the case by calculating the electron temperature decrease following the self-similar expansion treatment of Ref. [22].

For low density UCPs, evaporation can have a significant effect on electron temperature [15]. However, for the particular experimental conditions in this work, the effect of evaporative cooling was greatly reduced due to the magnitude of the applied electric field. Using the observed escaping rate of electrons from UCP at the time that our oscillation damping data were taken, we could estimate the amount of energy carried away by the escaping electrons to produce a ΔT_{evp} in a self-consistent model that related UCP electron potential depth, electron temperature, and escape rate to the observed conditions. We first estimate the depth parameter η from an evaporation model using a detailed balance technique. For details about this technique, see Ref. [11, 24]. The basic idea is that a numerically efficient model of the evaporation rate of electrons out of a UCP can be constructed by explicitly tracking the highest energy electrons in the UCP since those are the most likely to collide, pick up energy, and evaporate. Tracking only the highest energy electrons

reduces computational burdens, at the expenses of having to model the creation of higher energy electrons from lower energy electrons due to collisions and loss of higher energy electrons as they sometimes collide and lose energy. The end result of these calculations is a predicted evaporation rate that can be compared and then matched to the actual evaporation rate observed from our UCPs under different conditions. The evaporation rate was determined by the temperature T_e and η, where the trapping potential depth is $\eta k_b T_e$. From these two parameters we estimated the energy carried away by electrons escaping after plasma formation (see Ref. [14] and Chapter 5). Since we know the initial temperature and the amount of cooling, we were able to calculate the final temperature and compare this value to the temperature used in the evaporation model. By doing this self-consistently, we can obtain an estimated cooling contribution to the temperature from evaporation. We found that evaporation reduced the electron temperature by 9 % in each of our experimental conditions. The temperature reduction was not sensitive to the precise value of the predicted electron escape rate.

We collected our data using three different photoionization wavelength settings and thus three different temperatures, which were 2.87K $\pm$ 0.25 K, 5.74K $\pm$ 0.32 K, and 14.8K $\pm$ 0.73 K, respectively, as determined following the analysis presented above. In other words, these temperatures were determined via knowledge of the UCP density, photoionization laser wavelength, three-body recombination heating, and electron evaporation rate as measured in our experiments. The ion number was centered at approximately 200,000 for all cases, and the data set to data set variation in average number was on the order a few percent. The charge imbalance δ was 0.475, and again was maintained on average at the percent level across data sets. The value of σ that characterizes the spatial size of the UCP was 720 μm for our data, with variation described in the section below.

4.4 Results

In Fig 4.11, we show all of the complete data sets that we collected for this measurement. In each, the experimental data are represented as points with error bars that correspond to the observed statistical variation averaged across all points. The best-fit model predictions corresponding to each experimental condition are also shown for comparison. Overall, there is qualitative agree-

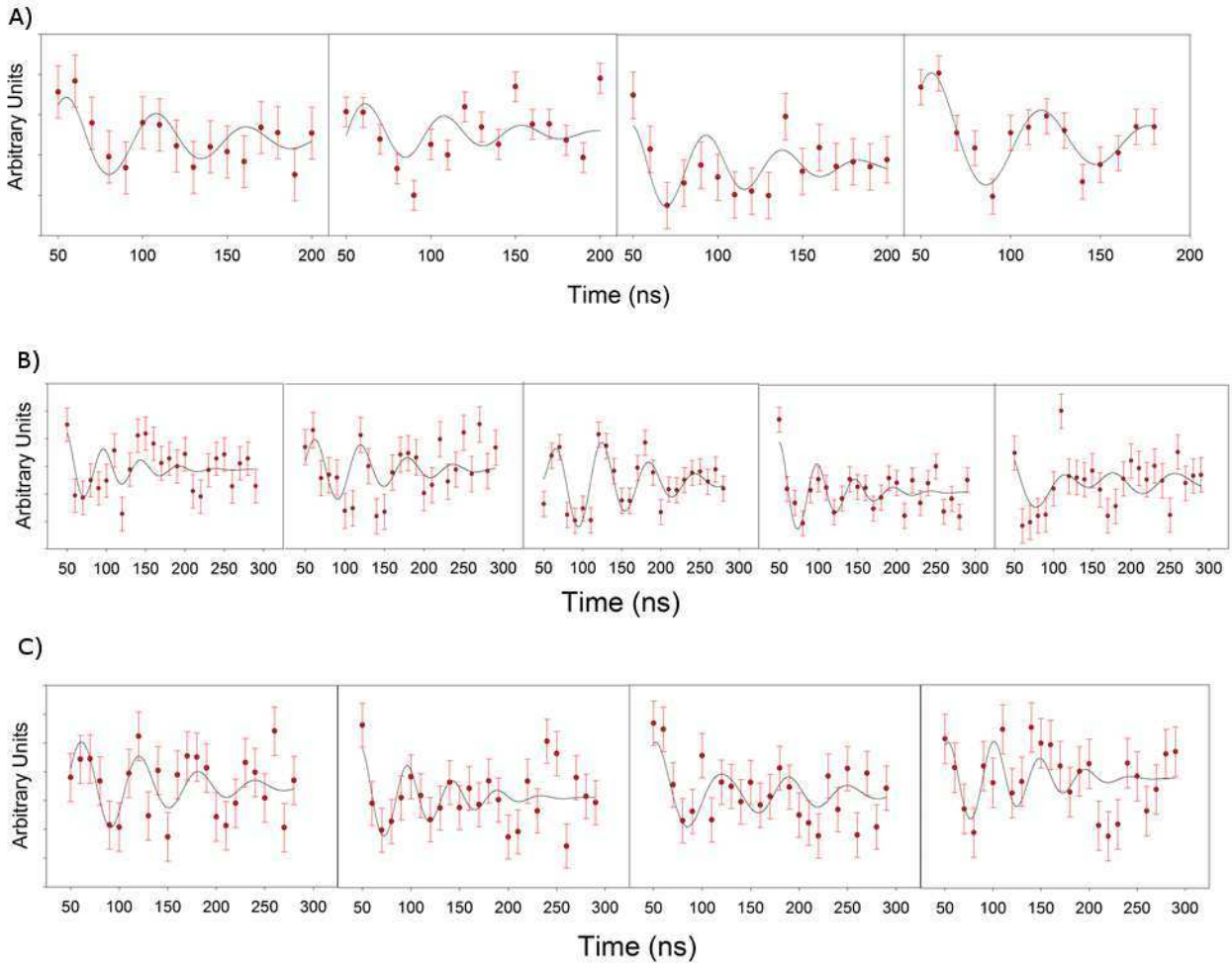

Figure 4.11: Comparison of model (solid line) to the experimental data (solid points). The electron temperature of A, B, and C were 2.87 K, 5.74K, and 14.8 K respectively. Data was taken with δ=0.475, 200,000 ions, 9 G magnetic field and electric field 4.1 V/m.

ment between the experimental measurements and the predicted oscillation damping. In the rest of this section, we discuss how we obtained a more quantitative comparison between the two.

Before doing so, we would note that the signal-to-noise measurement for each data set is such that about nine hours of continuous collection is required for each set. During that time, depending on lab conditions, there could be significant drifts over that time period and so data collected during those times would not be of sufficient quality for a complete set. Those data are not shown in Fig. 4.11.

In order to compare the measured damping rate to the damping rate predicted by our model calculations, it is useful to parameterize the measured damping rate in terms of an effective damping constant k_{eff}. Unlike the zero magnetic field case, the center-of-mass oscillation damping is not well described by a decaying sinusoid with a single decay constant γ when the magnetic field is present (see Fig 4.5). In fact, the center-of-mass amplitude change in time with the magnetic field present is generally complicated. However, the range of our experimental data corresponded to early time parts of the center-of-mass motion, and for the needed ranges of time the center-of-mass motion with the magnetic field present could be parameterized with a two-time-constant function given by:

$$(Ae^{-k_1(\omega)t} + Be^{-k_2(\omega)t})cos(\omega t + \phi) \tag{4.4}$$

where A, B are amplitude constants, $k_1(\omega), k_2(\omega)$ are the damping constants, and ω, ϕ are the oscillation frequency and phase. The damping constants are mild functions of the density. Since ω tracks the density, the values of the damping constants and ω are linked in the model calculation. Hence the indication of the scaling of the damping constants with ω is shown.

Given Eq. 4.4, we use a two-step process for determining the effective decay constant k_{eff} from our measured data.. First, we fit our measured oscillation signal (Fig 4.11) to the following functional form:

$$D(Ae^{-k_1(\omega)t} + Be^{-k_2(\omega)t})e^{-k_{aux}t}cos(\omega t + \phi) \tag{4.5}$$

where D, ϕ, ω and k_{aux} are all treated as fit parameters where the other parameters are determined from model predictions at the temperature associated with the experimental data being fit. D is

a scaling parameter for our MCP signal. ω and ϕ allow for determination of the density and time offset associated with the data. If the model damping rate was a perfect fit to the experimental damping rate, k_{aux} would be zero. In the event that the experimental damping rate fits to a rate faster than predicted, k_{aux} would be greater than zero. If the experiment damping rate fits to a slower damping rate, then k_{aux} would be less than zero. From all of the data sets measured at a particular temperature, the central value of k_{aux} that best fits the data and the standard uncertainty in that parameter were determined. To determine k_{eff} determined by the data, we use the following equation:

$$(A+B)e^{-k_{eff}t_0} = (Ae^{-k_1(\omega)t_0} + Be^{-k_2(\omega)t_0})e^{-k_{aux}t_0} \tag{4.6}$$

where t_0 is set to a convenient value, 150 ns for the range of times typical of our experiments. Recall that A and B are not fit parameters, but come from model predictions. The value of k_{eff} determined from the data can be compared to model predictions of k_{eff} by deriving a model prediction for k_{eff} determined by setting k_{aux} to zero in the equation above.

One other consideration is added to the parameterization described above. The spatial size of the atom cloud that was ionized (σ) is not perfectly constant from experiment run to experiment run. This leads to a frequency variation from run to run that appears as damping since later time data points from runs with different frequency had different phases from one another. We determine the damping from this effect via an additional fit parameter added to our data analysis. The $\sim 5\%$ run-to-run variation indicated by this fit parameter is consistent with the estimated σ variation in our system.

This somewhat involved data analysis technique allows us to determine an effective experimental and model decay rate k_{eff} in analogy to a single sinusoidal decay constant γ for each of our temperature conditions using all of our complete experimental data sets, in light of the structure of the predicted CM damping curves from our model predictions. The model predictions and experimental data can thus be compared in terms of a damping rate.

4.5 Analysis And Discussion

Fig 4.12 compares our measured damping rates to predicted damping rates in terms of the k_{eff} parameter described above. Within the uncertainty of our measurements, the experimental results and model predictions are in agreement. Choosing a different value of t_0 does not change the degree of agreement in any significant way. This indicates that our modeling of the CM motion is in agreement with experimental results at our level of statistical significance. We note that the absolute value of the damping rate is not a free parameter in this analysis, but is rather determined from the density and electron temperatures we determined independent of the damping rate for our conditions.

The conditions that we selected to conduct our experiments to compare with the model were based on considerations of charge neutrality, applied electric field, and signal-to-noise. For the given number of ions and electrons we selected, significantly smaller electric fields would have resulted in more neutral plasmas and faster damping rates, reducing signal-to-noise. Significantly larger electric fields would have driven faster damping due to the dependence of the damping rate on the applied electric field. We operated between those extremes. Running with smaller electron and ion numbers than the maximum of our system was capable of ($\sim$ 10 percent of our maximum number of ions and electrons) resulted in being able to access a more favorable neutrality/electric field parameter region.

For this set of conditions, the damping rate is dominated by collisionless mechanisms, according to model calculations. This can be determined by comparing k_{eff} rates with the binary electron-ion collisions included in the model and without those collisions included. Removing the electron-ion collisions in the calculation reduced k_{eff} only by several percent, indicating for these conditions electron-ion collisions are predicted to have only a mild effect on the damping rate.

While our data serve as an experimental test of our model predictions, measuring the electron oscillation damping rate in a collisionally-dominated parameter region would enable the testing of electron-ion collision rate predictions. In order to gain sensitivity to electron-ion collisions, a different UCP strategy would need to be pursued. This will be presented in chapter 5.

From our research after the original analysis and publication of these results, , we found the applied DC electric field will increase the temperature of UCP during formation. Since this effect

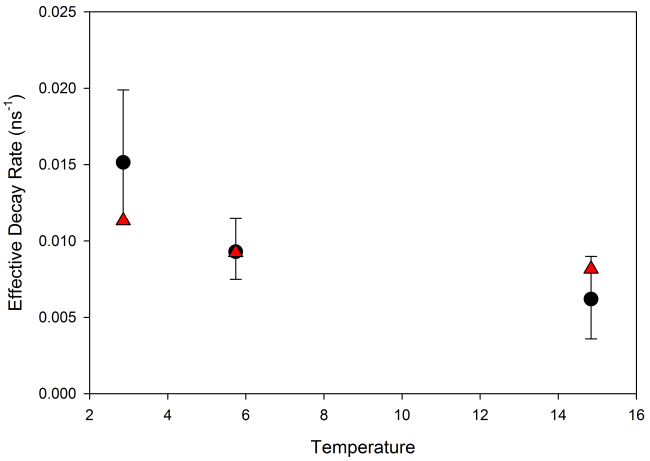

Figure 4.12: Effective damping rate vs temperature. Data was taken with δ=0.475, 200,000 ions, 9 G magnetic filed and electric field 4.1 V/m. The black dots are the experimental results and the triangles are the calculation results.

was unknown at the time, it was not included in this original analysis. In principle, a detailed reanalysis of all of the data could be performed. However, we don't expect such a reanalysis to change our basic conclusions or reveal new physics considerations. The amount of heating is estimated to be about 2.1 K from the electric field heating for all three temperature conditions. However, the amount heating from three-body recombination would be reduced and so the full 2.1K of additional heating would not be imparted. Slightly higher evaporative cooling would be expected, too. A reasonable estimate of the temperature increase of each point would be about 1.5K. As shown figure 4.12, for the higher two temperature points, the predicted damping rate increases very slowly with increasing temperature. Therefore, shifting data points about 1.5K to the right would not change the degree of agreement significantly. The situation is somewhat worse for the coldest point as there would no longer be agreement within the error bar. However, the resulting disagreement would still by only about 1.3 standard deviations. The probability that the amount of variation that was observed in the shifted data would occur given a statistical distribution is still greater than 30% – certainly indicating the absence of a strong disagreement between predictions and measurements. In addition, the results in chapter 5 indicate that strong-coupling effects may be starting to play a role for the coldest point in this data set, too.

4.6 Conclusion

In this chapter, we developed a technique that uses two short electric field pulses to initiate and measure the oscillation and damping of the electron CM motion. In order to interpret the data, we constructed a numeric simulation model that was able to model the electron CM oscillation in our experiments. We found that in the parameter regimes in which we perform studies in this chapter, the damping rate of the oscillation is dominated by the dephasing of electron motion, a collisionless mechanism. By moving to the parameter space where the damping of electron CM oscillations is dominated by electron-ion collision, we can move on to study electron-ion collisions and the strongly coupling influence on such collisions and this will be described in the next chapter.

References

[1] L. Spitzer, Jr., *Physics of Fully Ionized Gases* (Dover, New York, 1962).

[2] L. Landau J. Phys. (USSR) **10**, 25 (1946).

[3] L. Tonk, Phys. Rev. **37**, 1458 (1931).

[4] A. Dattner, Phys. Rev. Lett. **10**, 205 (1963).

[5] R. S. Fletcher, X. L. Zhang, and S. L. Rolston, Phys. Rev. Lett. **96**, 105003 (2006).

[6] T. C. Killian, S. Kulin, S. D. Bergeson, L. A. Orozco, C. Orzel, and S. L. Rolston, Phys. Rev. Lett. **83**, 4776 (1999).

[7] J. P. Morrison, C. J. Rennick, J. S. Keller, and E. R. Grant, Phys. Rev. Lett. **101**, 205005 (2008).

[8] S. Kulin, T. C. Killian, S. D. Bergeson, and S. L. Rolston, Phys. Rev. Lett. **85**, 318 (2000).

[9] T. M. Wilson, W.-T. Chen, and J. L. Roberts, Phys. Rev. A **87**, 013410 (2013).

[10] L. S. Brown, D. L. Preston, and R. Singleton Jr., Phys. Rep. **410**, 237 (2005).

[11] Craig Witte, *Computational Modeling of Low-density Ultracold Plasmas*, Ph.D. Dissertation (Colorado State University, 2017).

[12] P. E. Grabowski, M. P. Surh, D. F. Richards, F. R. Graziani, and M. S. Murillo, Phys. Rev. Lett. **111**, 215002 (2013).

[13] M. E. Glinsky, T. M. ONeil, M. N. Rosenbluth, K. Tsuruta, and S. Ichimaru, Phys. Fluid B **4**, 1156 (1992).

[14] T. M. Wilson, *Dynamics of low-density ultracold plasmas in externally applied electric and magnetic fields*, Ph.D. Dissertation (Colorado State University, 2013).

[15] T. M. Wilson, W.-T. Chen, and J. L. Roberts, Phys. Plasmas **20**, 073503 (2013).

[16] M. S. Murillo, Phys. Rev. Lett. **87**, 115003 (2001).

[17] P. Gupta, S. Laha, C. E. Simien, H. Gao, J. Castro, T. C. Killian, and T. Pohl, Phys. Rev. Lett. **99**, 075005 (2007).

[18] S. Hamaguchi and R. T. Farouki, J. Chem. Phys. **101**, 9876 (1994).

[19] D. G. Swanson, *Plasma Kinetic Theory*. CRC Press (2008).

[20] S. Mazevet, L. A. Collins, J. D. Kress, and T. T. Grove, Phys. Rev. Lett. 88, 055001 (2002).

[21] T. C. Killian, M. J. Lim, S. Kulin, R. Dumke, S. D. Bergeson, and S. L. Rolston, Phys. Rev. Lett. **86**, 3759 (2001).

[22] F. Robicheaux, and J. D. Hanson, Phys. Rev. Lett. **88**, 055002 (2002).

[23] S. G. Kuzmin and T. M. Oneil, Phys. Plasmas **9**, 3743 (2002).

[24] Craig Witte and Jacob L. Roberts, Physics of Plasmas **24**, 052122 (2017).

Chapter 5

The measurements of center of mass damping of electrons in ultracold plasma collisional region

In this chapter, we will address the fundamental importance of electron-ion collisions rates in plasmas. We will then explain the problems of the weak-coupling expression of electron-ion collision rates when the degree of coupling in plasmas becomes strong. Experiments and molecular dynamics simulations were performed to investigate the strong coupling influence on electron-ion collision rates. Our measured results showed not only clear influences from the strong couping effect but also the breakdown of standard assumptions used in treatments for plasma collisions.

5.1 Introduction

In chapter one, we see that in systems with sufficiently strong interactions between particles, spatial correlations develop and many properties of the system are affected significantly. In plasmas, the onset of significant correlations is referred to as strong coupling and is characterized by the dimensionless parameter $\Gamma = \frac{1}{4\pi\epsilon_0}\frac{e^2}{a}/k_bT$ [1], which is the ratio of the typical nearest neighbor Coulomb potential energy to thermal energy in a plasma, where e is the plasma constituent charge, ϵ_0 is the vacuum electric permittivity, a is the Wigner-Seitz radius, k_b is the Boltzmann constant, and T is the temperature. Strongly coupled plasmas can be created in laboratory settings [2–6] through either ionizing solid state densities (small a), through ionizing cold atoms (small T), or through highly charged grains (dusty plasmas). Strongly coupled plasmas are also predicted to be found in astrophysical [7, 8] environments as well.

One of the consequences of such strong coupling of a plasma is the breakdown in the standard approximations used to calculate collision rates [9]. Collision rates, such as the electron-ion collision rate, are of fundamental importance in thermalization and transport. They determine several other plasma properties, such as electron-ion thermalization rates [10], transport coefficients (diffusion, electric conductivity) [11], and stopping power considerations that, for instance, influence achievable DT fusion [12, 13]. To be clear, for our work, strong coupling is considered with respect to the

electron component of the plasma, not the ion component as in studies elsewhere [14]. The electron-ion collision rate of weak-coupled plasma is given by [15]

$$\nu_{ei} = \frac{1}{3}\sqrt{\frac{2}{\pi}}\frac{Z^2 e^4 n_i}{4\pi\epsilon_0^2 m_e^2 v_{th}^3}\ln\Lambda, \tag{5.1}$$

where Z is charges number, e is the elementary electron charge, n_i is the ion density, ϵ_0 is the electric permittivity in vacuum, m_e is the mass of an electron, v_{th} is $\sqrt{k_b T_e/m_e}$, and $\Lambda = \ln(C\lambda_D/b_0)$, where λ_D is the Debye screening length, $b_0 = e^2/4\pi\epsilon_0 k_b T$ is the charateristic large angle scattering impact parameter, and $C = 0.765$ is suggested in Ref. [10, 16, 17].

The presence of the screening length in the collision rate shows collective effects are relevant in a plasma even for individual collisions. This comes about because of a logarithmic divergence in the computed collision rate arising from large impact parameter collisions. The screening in a plasma reduces the influence of such collisions by screening out the inter-particle Coulomb forces. More specifically, this justifies using a cutoff parameter based on the screening length λ_D in Coulomb collision integrals to prevent the divergence of the integral (also see chapter 2).

The strong coupling parameter can be written in terms of b_0 and λ_D as $\Gamma = [b_0/(\sqrt{3}\lambda_D)]^{2/3}$. For sufficiently strongly coupled plasmas, Eq. 5.1 must break down. This can be seen by rewriting Eq. 5.1 in terms of the electron plasma frequency (ω_p) and Γ as $\nu_{ei} = \omega_p\sqrt{\frac{2}{3\pi}}\Gamma^{3/2}\ln(\frac{C}{\sqrt{3}}\Gamma^{-3/2})$ and noting that as Γ becomes greater than about 0.58, ν_{ei} becomes unphysically negative and the accuracy of Eq. 5.1 is expected to diminish significantly well before Γ reaches that value. Some theoretical effort in different contexts was made to extend this expression to the strong coupling regime by modifying the argument of the Coulomb logarithm [10, 16, 19, 20].

Ultracold plasmas (UCPs) are sufficiently cold and dense to enable stong coupling effect measurements to be conducted. In particular, UCPs are clean and well controlled systems for studying electron-ion or ion-ion collision rates where strong coupling influences are present [14, 21]. The universal dependence of the collision rate on Γ and ω_p makes the measurements of strong coupling effects on collisions in UCPs capable of testing of theoretical approaches that can be in turn applied to more complicated strongly-coupled plasma systems. The experimental investigation of the breakdown of Eq. 5.1 using UCPs is the primary motivation of the work in this chapter.

The work described in this chapter is really an extension of the electron oscillation damping measurement described in chapter 4. Using what we learned from that work, we were able to operate under conditions where collisionless mechanisms were not important. The damping was thus dominated by electron-ion collisions, allowing us to measure the electron-ion collision rate. The primary changes that we made were to reduce the electron and ion number even further than the previous work and to apply an larger electric field during UCP creation. Both of these things reduced anharmonic effects through having the electrons exist primarily in the more uniform-density center of the UCP.

In addidtion, one would not expect the Γ of the electron component can be greater than unity [22]. Essentially, if that degree of correlation could be maintained a plasma would turn back into atoms in about a plasma period. There are also simulations show upper limits of Γ [22, 26, 27], so it is interesting to see what value of Γ we can reach if we create the UCP by photoionizing the atoms just above the ionization threshold.

5.2 Experiment

To create our UCP for these experiments, we followed the techniques presented earlier in this thesis and in a previous thesis associated with this experiment [28]. A brief overview is provided here. We first made an ^{85}Rb magneto-optical trap and then loaded the atoms into an anti-Helmholtz coil magnetic trap. After the atoms were loaded into the magnetic trap, they were transferred to another chamber for plasma creation via two-step photoionization [29]. By controlling the wavelength of the photoionizing laser, the initial kinetic energy imparted to the UCP electrons could be controlled. Through adjusting the intensity of the laser associated with the first step of the two-step photoionization, we could control the number of the electrons and ions, and we typically ionize about 5% of the initial cold atom gas. After photoionization, some electrons will immediately leave the UCP until a sufficiently large space charge develops such that the remaining electrons are trapped, forming a plasma. Typical electron and ion temperatures can be as low as a few Kelvins [21]. The plasma would then expand and fall apart on the order of one hundred μs, but all the measurements reported here occurred before such expansion was significant.

Our primary experimental signal consisted, as usual, of measuring the electrons' escape from the UCP, both in response to sequences of applied electric field pulses and as a result of the unperturbed UCP evolution. There was an axial 2V/m DC electric field and a 9 G magnetic field applied that helped guide the escaping electrons to the detector, the micro-channel-plate. Typical plasma ion numbers N_i were 6.9×10^4 ions with a distribution $n_i e^{-r^2/2\sigma^2}$, where r is the distance to the center of the plasma, n_i is the peak ion density, and σ is the characteristic spatial extent, which is about 650 μm for our experiments.

To perform our experiments, we created the UCPs at a higher applied electric field then decreased that field down to 2.0(1) V/m to operate at a desired charge imbalance, which is about 45% electrons remaining in the plasma. The chosen combination of low ion numbers and high charge imbalance was selected to operate in the regime where the electron oscillation damping was predicted to be dominated by electron-ion collisions (see chapter 4). The experimental two-pulse sequence that we used to measure the electron oscillation damping was the same as in chapter 4. In this case, 3.6 μs after the plasma was created, we applied a short electric pulse along the DC electric field direction to 'kick' the electrons to initiate the electron center-of-mass (CM) oscillation. We chose to take the measurement at this time because the formation processes are finished and stablized at this point but it is still early enough that the expansion is still ignorable so that the plasma size is essentially the same as the initial size. As in chapter 4, by measuring the amount of the electrons that escaped as a result of the second pulse as a function of the delay time between the two pulses, we mapped out the original electron oscillation as a function of time. A typical data set from such a measurement set is shown in Fig. 5.1. We then extract the oscillation frequency and damping rate from such a measurement. We performed the measurement at two initial ionization energies : $k_b \cdot 2.26$ K, and $k_b \cdot 0.1$ K. These values are chosen to be just above ionization threshold on the low side, and not too hot on the high side such that the damping rate would be difficult to resolve.

5.3 Analysis And Results

To extract the decay rate of the oscillation, we fit the data such as shown in Fig. 5.1 to a damped cosine wave $Ae^{-kt}cos(2\pi ft + \phi) + c$, where A is the amplitude of oscillation, k is the

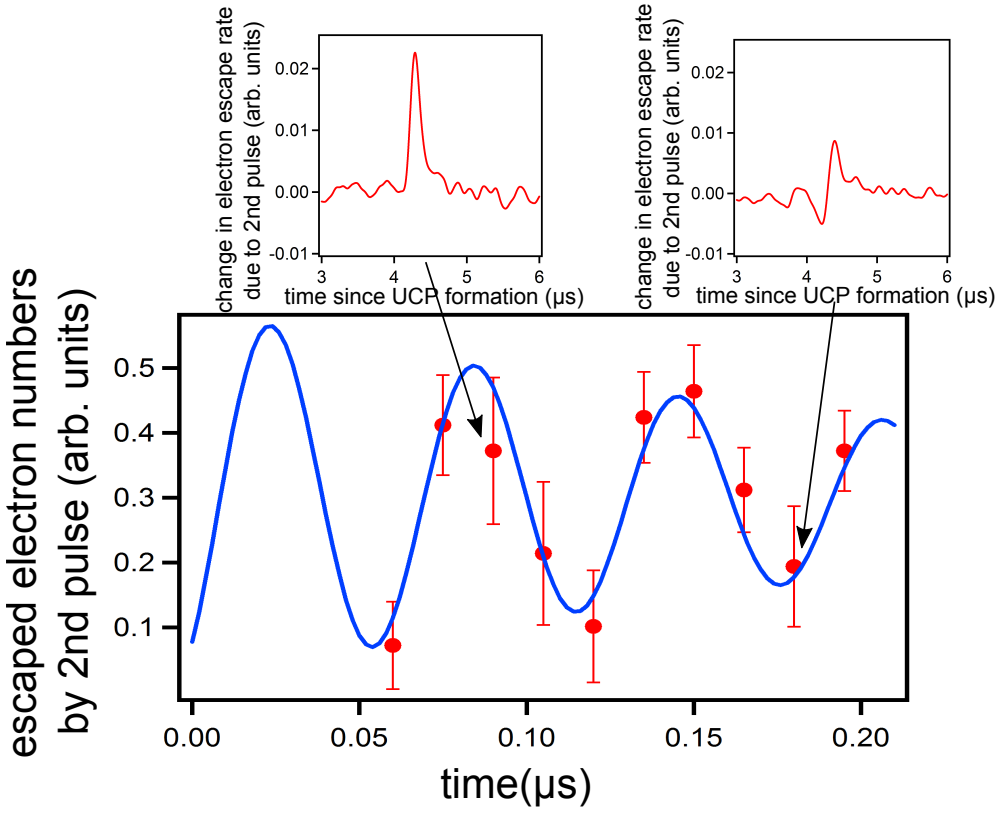

Figure 5.1: A typical experimental data set. The data points show the electron escape as a function of time delay between the initial and second applied electric field pulse. The solid line is the damped cosine wave fit to the data. This set was taken at initial electron kinetic energy $2.26K \cdot k_b$. The ion and electron numbers were 5.9×10^4 and 2.7×10^4 respectively. The two insets show the recorded net electron escape signal as detected for a relatively large escape point (left) and a relatively low escape point (right).

damping rate, f is the frequency, ϕ is the phase, and c is the offset. There were two complications that we had to deal with in doing so. First, there existed shot-to-shot variation in particle number, spatial size, and charge imbalance. This effectively added a phase variation that would introduce an additional apparent damping into the data since the oscillation frequency is sensitive to those parameters as pointed out in chapter 4. However, the charge imbalance and the total number were measured with high precision for each individual data point, and the size is a function of those two parameters. The total number was determined from the integration of the total MCP signal (i.e. counting all the escaped electrons). We could do this with a precision of well better than one percent. The charge imbalance was similarly determined by computing the ratio of the integrated MCP signal before the oscillation measurement time and the total integrated signal. Again, the precision in doing so was better than a percent. To mitigate number and charge imbalance variation problem, we introduced linear correction terms to compensate the variations on a point-to-point basis in the damped cosine fit through using the measured charge imbalance and total number values. The variations from charge imbalance and total ions numbers showed up in the variations of amplitude A, frequency f and phase ϕ of the oscillation. Therefore, for f, ϕ and A, we added linear corrections scaling with the difference in charge imbalance $d\delta$ and total number dN for each data point. Again, $\delta = (N_{ion} - N_e)/N_{ion}$, where $d\delta$ is the difference between the charge imbalance for the specific data point as compared to the average charge imbalance for the data set as a whole, dN is the the same type of difference with respect to the total number. The correction to f, ϕ, and A were set to be $a_1 d\delta + b_1 dN$, $a_2 d\delta + b_2 dN$, and $a_3 d\delta + b_3 dN$ respectively for each individual data point. For each set of data, we performed a χ^2 fit for all fitting parameters, including the damping rate k.

Secondly, our current signal-to-noise level is small enough so that standard statistical analysis that assumes first-order expansions are sufficient to describe fluctuations needed some corrections. Therefore, we analyzed random simulated data using our analysis protocol (i.e. fitting the decay curves with the above linear correction terms) to ensure proper fitting of the damping rate and the determination of the associated uncertainties. This had the additional effect of demonstrating that the linear correction terms added to account for shot-to-shot variation successfully did so for our protocol. The resulting damping rates were $3.72 \mu s^{-1} \pm 0.79\ \mu s^{-1}$for initial ionization energy

$k_b \cdot 2.26$ K, and $8.53\mu s^{-1} \pm 1.54\ \mu s^{-1}$ for initial ionization energy $k_b \cdot 0.1$ K for our average particle number and spatial size conditions.

5.4 Discussion

One of the main goals of our work is to measure the degree to which strong coupling corrections to the usual weak-coupling expression of electron-ion collision rates are needed to match our experimental measurements. In order to determine the predicted electron CM oscillation damping rate given an electron-ion collision rate as in, say, Eq. 5.1, the collision and damping rates need to be related to one another. If the electrons remained in thermal equilibrium during the oscillation (i.e. could be treated hydrodynamically), an analytical relationship could be easily calculated. That is, the oscillation damping rate would be 0.5 times the damping rate obtained from Ref. [10, 16, 19]. However, the electron-electron collision timescale is on the order of the electron-ion collision timescale, and so the electrons cannot be assumed to be in thermal equilibrium during the damping measurement. In addition, the scattering rates for slower electrons are higher than for faster electrons. This leads to non-trivial velocity-space correlations that must be explicitly accounted for.

To illustrate the basic issue, consider the high energy electrons in the UCP. These electrons have lower collision rates. When kicked, they can travel farther in the UCP than slower electrons. Thus, the electron spatial distribution will shift from an equilibrium distribution to one where there is a correlation between spatial extent and initial electron velocity. Calculating a damping rate by averaging over an assumed equilibrium distribution is problematic in these circumstances.

In order to take such an effect into account, we developed a numerical model capable of linking any predicted electron-ion collision rate to a predicted oscillation damping rate. This Monte-Carlo binary collision model is the same as the one used in chapter 4 to calculate the oscillation damping rates in that work. An overview is provided here. See the PhD thesis of Craig Witte [18] for additional details. In this model, the electrons are tracked as individual particles that interact with one another via Coulomb forces (i.e. MD simulation for electron-electron interactions). The electrons are placed in a smooth positive charge background with Gaussian spatial distribution to match our experimental conditions to model the electron confinement. The electron-ion collisions

are modeled with a random collision operator that consists of three parts. First, for an electron moving with velocity v, a maximum possible impact parameter b_{max} is computed. Second, the probability of a collision in each timestep dt, is calculated as $nv\pi b_{max}^2 dt$, and random numbers are generated for each electron to see if a collision occurs. Finally, if a collision does happen, the impact parameter is randomly determined and the resulting electron velocity deflection from the collision is applied accordingly and instantaneously.

We apply all of the usual assumptions typically used in weak-coupled electron-ion collision calculations. The first one is that collisions occur via Rutherford scattering with a cutoff parameter b_{max} based on λ_D. The second one is the use of the binary collision approximation which means the deflections are accumulated through only two body collisions. The third one is a substitution of a thermal velocity in the Coulomb logarithm for an individual electron velocity. This approximation comes from the fact that for each velocity class v, the Coulomb logarithm is really of the form $g(v) = \ln C\lambda_D/(e^2/4\pi\epsilon_0 mv^2)$ (see chapter 2). Computing collision quantities of interest involves averaging over a velocity distribution $f(v)$. In that case the averaging integration contains $f(v)\ln g(v)$ in the integrand. For weakly coupled plasmas, $\ln g(v)$ is mostly constant over the part of the velocity range that contributes most to typical integral quantities, so one can repalce the velocity in the logarithm by thermal velocity and pull the logarithm out of the integrand and still obtain a good result. While very common in plasma physics, such a direct substitution of T terms for v^2 terms is not conducted carefully on a formal basis. However, such a substitution can be accomplished in a formal way. To maintain the same integration result, the use of substitution of thermal velocity in the logarithm requires a velocity dependent cutoff $C\lambda_d k_B T/mv^2$ for the integration limit that cuts off the impact parameters to avoid the divergence associated with Coulomb collisions discussed earlier in the thesis. Since theoretical results are reported in the literature with the T substitution of velocity terms in the Coulomb logarithm, and those results are reported to be in agreement with more sophisticated theoretical calculations, we adopt the velocity-dependent cutoff. The last typical assumption that we use is an assumption that ions are spatially uncorrelated [9]. Within these approximations, any given electron-ion collision expression translates to a unique random collision operator. Thus, given a model for electron-ion collisions, an electron oscillation damping rate can be calculated. For weak-coupling predictions, we set the collision cross-section to produce collision rates consistent with those implied in the so called BPS stopping power model [17].

To see if strong coupling corrections are necessary, we performed simulations from 1.2 K to 2.6 K around the maximum electron-ion collision rate given by the weak-coupling expression in Eq. 5.1. The existence of a such maximum in the predicted collision rate is due to the fact that the Coulomb logarithm tends toward zero at low electron temperature since it does not account for strong coupling effects within the weak coupling approximations. We found that the weak-coupling limit damping rate peaked around 2 K with rate $3.3\mu s^{-1}$ as shown in Fig. 5.2. The predicted maximum damping rate is beyond 3 standard deviations below the measured damping rate of our colder temperature data. Thus the weak coupling predictions cannot match our experimental observation for any electron temperature.

The need for a strong coupling correction is thus clearly evident. To capture the strong coupling effect directly to compare with our data, we performed full MD simulations for both electrons and ions. In other words, direct force calculations are not only conducted between electrons in the simulation, but between point ion particles (and those particles and the electrons) as well. A softening parameter for the Coulomb potential was used to address timescale and other problems associated with unlike charges [22]. The Coulomb potential between two charges was set to be $U = e^2/4\pi\epsilon_0\sqrt{r^2+\alpha^2}$, where α is a softening parameter. We confirmed that the softening parameter was small enough that it did not significantly impact the predicted damping rate. The MD simulation predicted larger damping rates for parameters where the strong coupling was expected to be significant. By tuning the electron temperature, the predicted damping rate could be matched to our experimentally measured damping rates. The main question is thus whether the implied temperature obtained through this technique is consistent with expectations.

There were several factors that influenced the electron temperature of our UCPs. The first one was the initial ionization energy, which was determined by the photoionization laser wavelength. Other known effects include continuum lowering [30], three-body recombination heating [25], disorder induced heating [31], evaporative cooling [32], and adiabatic cooling. Our conditions were chosen to minimize all these factors. This is mainly done by operating in a low density regime, since the disorder induced heating and continuum lowering scale roughly with $n^{1/3}$, and three-body recombination heating scales with n^2. We used the MD simulation to estimate the net contribution of all the factors listed above. When we did so, we found that the most significant heating arose from a previously unreported mechanism where a DC electric field applied during the formation

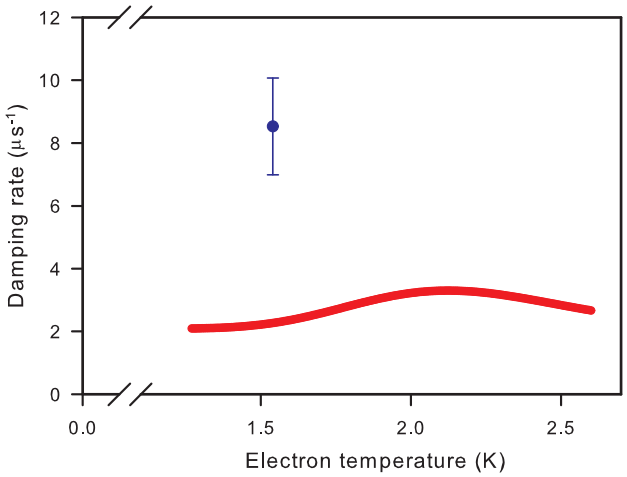

Figure 5.2: The weak coupling prediction of the damping rate (red line) vs the electron temperature from our MC random collision model. The ion number in the simulations was 7.2×10^4, and the spatial size was 650 μm. The damping rate peaked at 2 K, which is an expected behavior for weak coupling treatments. The data point shown in the figure is from our colder condition.

raises the electron temperature. This heating occurs because the DC electric field accelerates the electrons while the trapping potential due to the ions develops, resulting in a net increase in electron kinetic energy.

Using MD simulations, we could predict the amount of heating as a function of the initial ionization energy and applied DC electric field. We note that such a prediction captures other heating and cooling mechanisms (e.g. evaporation), and so does not independently predict the amount of heating from the DC electric field alone. The DC electric field was measured to be 2.0(1) V/m using our electric field calibration procedure described in chapter 3 and Ref. [32]. By running the MD simulation using this measured electric field while initializing the simulation with our experimental conditions, we can compare the measured damping rates to the predicted damping rate as shown in Fig. 5.3. We found reasonable agreement between the two. The consistency between MD simulation results and experimental measurements gives us confidence that the relevant physics considerations were accounted for in the MD simulation. We therefore used the MD simulation to extract the temperature from the measured damping rate. The temperature of the hotter set of data was determined to be 3.57 K $\pm$ 0.71 K and the colder set to be 1.58 K $\pm$ 0.28 K, corresponding to a density-averaged Γ of 0.15 $\pm$0.04 and 0.35 $\pm$0.08 respectively. Previous simulations showed that Γ will settle to a maximum of around 0.2 for times sufficiently long after UCP formation [25]. This is due to the interplay between the three-body recombination heating and the plasma expansion. However, Γ higher than 0.2 is expected for early times [25–27] when the three-body recombination heating is less significant. Our observation of $\Gamma = 0.35 \pm 0.08$ is in line with these predictions.

The heating from the DC electric field can be estimated in the following way. Assume that both the electrons and ions form a solid spherical ball with a uniform density, and only uniform external electric fields are considered. In our estimate, we set the density to be the average density n_{ave} of a Gaussian profile at a given charge imbalance for our experimental conditions. The charge imbalance can be estimated by using the model in ref. [32] and chapter 4, and the estimated charge imbalances are close to the charge imbalance from MD simulations. If there is no external DC electric field, the electron ball will sit at the center. If there is an external DC electric field, we can calculate how far the electron ball will be displaced from the center by

Table 5.1: Comparison of final electron temperature T_e between the simple model and the MD simulation. Initial temperatures are 2/3 times the initial kinetic energy. T_e from MD simulation is measured when the temperature is shown as stablized in the simulation.

E_{ext}	**initial tempeature**	**Final T_e (estimate)**	**Final T_e (MD)**
2 V/m	0.067 K	1.2 K	1.7 K
2 V/m	1.5 K	2.3 K	2.7 K
4 V/m	0.067 K	3.0 K	2.7 K
4 V/m	1.5 K	4.3 K	3.7 K

$$d = \frac{3\epsilon_0 E_{ext}}{e n_{ave}} \tag{5.2}$$

where E_{ext} is the applied external DC electric field, n_{ave} is the number density of the electrons, e is the elementary electron charge, and d is the displacement. The associated potential energy change per electron between the centered and displaced position is $eE_{ext} \cdot d/k_b$ in units of Kelvin-equivalent energy units. Since the electrons are created in a centered configuration, if we assume that all of the potential energy difference between the initial and final positions is converted to electron kinetic energy, the temperature increase from this potential energy will be $2eE_{ext} \cdot d/k_b/3$. The initial temperature of the electrons is estimated approximately to be the temperature from initial kinetic energy plus $2eE_{ext} \cdot d/k_b/3$. Using this initial temperature, we can further estimate the effect from three-body recombination heating as described in chapter 4 to improve the estimate. The initial kinetic energy and the density of the hotter condition is 2.36 K and $6.5 \times 10^{12} m^{-3}$, and the colder condition is 0.1 K and $6.9 \times 10^{12} m^{-3}$. The comparison between the naive model and the MD simulation is listed in Table 5.1. However, this comparison is not a fair one since rhe MD simulation contains other processes like continuum lowering, disorder induced heating and evaporative cooling. The estimation of temperature from the naive model can be off by 10% to 30%, which suggests this simple model description is able to give reasonable result for the purpose of estimation at least.

Our goal in this work is to observe the effect of strong coupling on the oscillation damping rate solely due to electron-ion collisions, but we learned from the previous chapter that there could be collisionless damping effects that show up in the system. To investigate this possibility, we ran MD simulations and found that even as we reduced the strength of the applied DC electric field from the previous 4 V/m value to 2 V/m, the damping rate with a 2 V/m electrc field on was still faster

than the field off case. This indicates there is still some collisionless damping present. Fortunately, this initial evaluation was done without the applied magnetic field in the simulation. Once the experimental magnetic field was added, this collisionless damping was reduced significantly. We also ran MD simulations without the DC electric field, but with the axial magnetic field on and off. We found no difference between the magnetic field on and off cases. This is expected from the fact that the gyro-radius $\sqrt{k_b T_e/m}/(eB/m)$ at 1.58 K is about 31 μm, which is greater than the Debye screening length which is about 27 μm [34], albeit on the same order. The gyro-radius is not substantially smaller than the Debye screening length, in any case.

Although the MD results are in agreement with the measured data, it is interesting to compare predicted strong coupling extensions using our MC binary collision code to our experimental results. These extensions have been theoretically developed in multiple contexts including electron-ion temperature equilibration, stopping power, effective potential, and transport and diffusion calculations [10, 16, 19, 24]. However, given that the oscillating CM electron velocity in our experiments is less than the typical electron thermal velocity (at least for most of the oscillation period), the range of comparison for these different approaches in the relevant parameter space is expected to be dominated by binary electron-ion collisions as the only relevant physics. Not surprisingly, these theories produce expressions that involve a modification of the Coulomb logarithm. For the range of Γ in our study, a modification consistent with the predictions in Ref. [10, 16, 19] is to set $\ln\Lambda = \ln\left(1 + 0.765\lambda_D/b_0\right)$ in Eq. 5.1. We concentrated on comparisons to these theories because they are consistent with one another and are referenced directly to classical MD simulations that involve assumptions that look to be well justified for UCPs. We applied these extensions to our Monte-Carlo binary collision calculation by substituting the weak-coupling cutoff $C\lambda_d k_B T/mv^2$ with $(b_0 + C\lambda_d)k_B T/mv^2$, to compute the resulting modification of the weak-coupling damping rate. For our colder conditions, the predicted damping rate is 3.41 μs^{-1}. This is an improvement on the weak-coupling-only prediction, but still not consistent with our measurement or associated MD simulation. Thus, a straightforward application of the implied collision rates in Ref. [10, 16, 19] fails to match our observations.

We tested the possibility that the velocity dependent cutoff may have different forms. We tested this by changing the velocity dependent cutoff from the original form of $Ck_B T/mv^2$ to $\alpha + \beta k_B T/mv^2$, where α and β were parameters chosen to produce results that are consistent

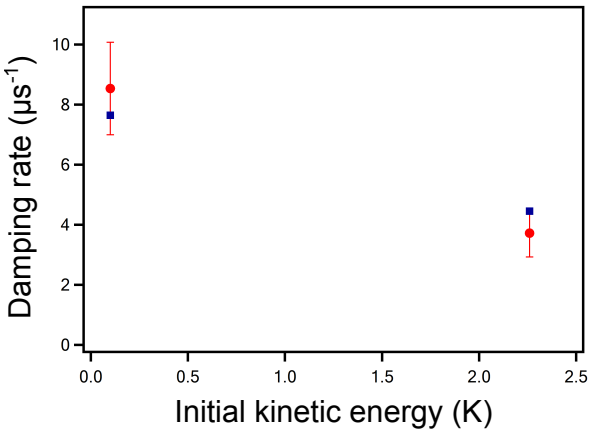

Figure 5.3: The electron C.M oscillation damping rate vs initial kinetic energy. The red circle is the measured rate and the blue square is the predicted rate from MD simulation.

with [10, 16] over a wide range of values of β. In other words, we always made sure that the stopping power and thermalization rates derived from the binary collision rate we used was constant and in agreement with these predictions. Thus, we were altering the relative contributions of different electron velocity classes to the damping, but not changing the average damping rate. This modification only produced a few percent variation compared to the original calculation.

A natural implication is that one or more of the standard assumptions that were included in the Monte-Carlo binary collision calculation are violated. The most suspect one is the thermal velocity substitution approximation as it is one of the most unphysical. We investigated what would happen if that approximation is modified. We did so by using a constant values of coutoff b_{max} over all velocity classes. This removes the thermal velocity substitution approximation completely while still requiring consistency with the predictions in Ref. [10, 16, 19]. By just removing this assumption, more than half the gap between the strong coupling predictions with the assumption (green dotted line in Fig. 5.4) and MD results was closed. While we were altering the nature of the cutoff (b_{max}) with velocity, we explored related impacts further by including dynamic screening that scales with each electron's velocity if consistency with Ref. [10] is maintained, the change in predicted damping rate from such a dynamic screening is less than a few percent. Despite achieving significant improvement by introducing the modifications above, there is still a difference that remained with respect to MD simulation/experimental results.

Thus, it seems that one or more other remaining assumptions are also violated. We examined the possible influence of ion-ion spatial correlations by increasing their mass substantially in the MD code to greatly slow down any correlation formation. Electron-ion correlation influence was also examined by MD simulation using like charge ions and electrons within a smoothed neutralizing background to see if unlike charge effects (Barkas effect) were significant. The changes in damping rate in both cases are found to be less than few percent - not enough for agreement. Therefore, it appears that the Rutherford scattering or binary collision approximation, or both, are not valid. Another possibility is that the electrons can not only scatter through individual ions but also scatter through the fluctuations of the ion density distribution. This hypothesis is in analogy to anomalous transport in fusion plasmas. Investigation of the breakdown in these assumptions is more complicated than relaxing other assumptions and is to be the subject of planned future work.

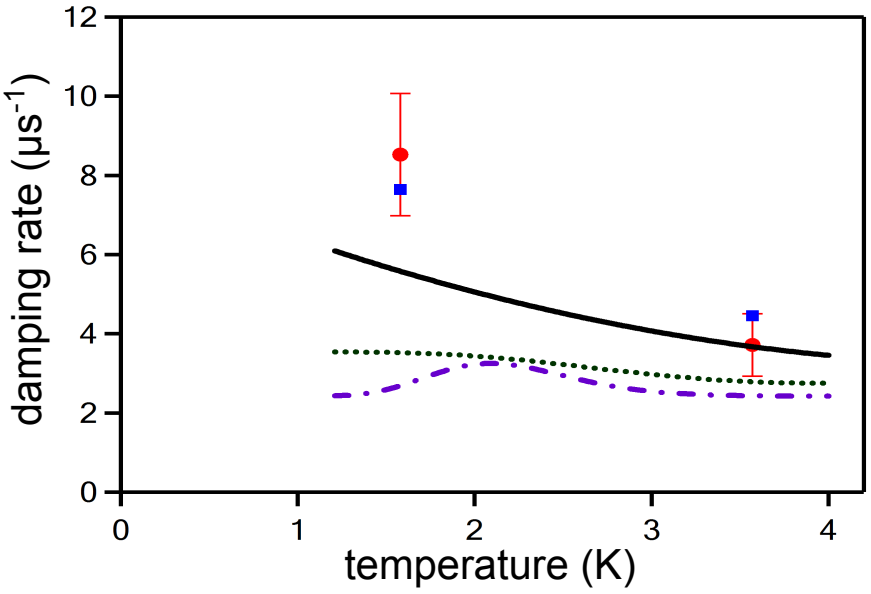

Figure 5.4: Comparisons between measured damping rates and calculations. The red circles are the measured damping rate. The blue squares are MD simulation results. All lines are results from MC binary collision model simulation results (see main text). The dash-dotted purple line is weak coupling result. The green dotted line is using strong coupling extensions from Ref. [10, 16, 19]. The black solid curve is the result using a fixed velocity-independent cutoff in addition to account for strong coupling corrections.

In any case, we show that the standard electron-ion collision approximations are problematic and need to be treated with care when strong coupling is relevant.

5.5 Conclusion

In conclusion, we experimentally measured a strong coupling influence on the electron-ion collision rate in a UCP through the electron CM oscillation damping rate measurements. Our experimental results were consistent with molecular dynamics modeling of our system. We report a measured electron strong coupling parameter as large as $\Gamma = 0.35(8)$, which demonstrates that experimental conditions at low density can achieve a greater value of Γ than predicted in [25], consistent with other predictions [26, 27]. In addition, we identify a previously unreported heating mechanism that occurs due to the presence of a DC electric field during UCP formation. Discovering this heating mechanism may help future experiments achieve lower temperature and hence higher Γ. Under the listed conditions, the necessity of strong coupling corrections is not surprising, but the size of correction is larger than expected from other theories [10, 16, 19, 24], and if typical assumptions are applied, it is not possible to obtain simultaneous agreement between our data and these theories. We found improvements if the standard practice of replacing velocity terms with temperature terms in the Coulomb logarithm is removed, but that change alone was not enough to produce agreement. This likely indicates breakdown of other assumptions, and further investigation of the validity of assumptions of Rutherford scattering and binary collision are called for. In addition, electrons may also undergo scattering through the density fluctuation in UCPs on top of normal binary collision process. All these subjects will be topics for future investigations.

We note that our use of a Monte-Carlo binary collision operator in our model is not unusual. This is a standard way of modeling collisions in, for instance, Particle-in-cell codes [35] used commonly to simulate plasmas. The disagreement between our binary collision code and MD simulation is thus potentially relevant to other theoretical treatments, if parameters where strong coupling is relevant are to be simulated. Our continuing efforts to understand our currently unexplained disagreements will also very likely be useful in this regard.

References

[1] S. Ichimaru, Rev. Mod. Phys. **54**, No.4., 1017 (1982).

[2] A. Ravasio et.al, Phys. Rev. Lett **99**, 135006 (2007).

[3] J. N. Tan, J. J. Bollinger, B. Jelenkovic and D. J. Wineland, Phys. Rev. Lett. 75, 4198 (1995).

[4] H. Thomas *et al.*, Phys. Rev. Lett. **73**, 652 (1994).

[5] M. S. Murillo, Phys. Plasmas **11**, 2964 (2004).

[6] S. X. Hu, B. Militzer, V. N. Goncharov, and S. Skupsky, Phys. Rev. Lett. **104**, 235003 (2010).

[7] H. M. Van Horn, Science **252**, 384 (1991).

[8] Bruce A. Remington, R. Paul Drake, and Dmitri D. Ryutov, Rev. Mod. Phys. **78**, 755 (2006).

[9] L. Spitzer, Jr., *Physics of Fully Ionized Gases* (Dover, New York, 1962).

[10] Guy Dimonte, and Jerome Daligault, Phys. Rev. Lett. **101**, 135001 (2008).

[11] F. L. Hinton, and R. D. Hazeltine, Rev. Mod. Phys. **48**, 239 (1976).

[12] A. B. Zylstra et al., Phys. Rev. Lett. **114**, 215002 (2015).

[13] J. A. Frenje *et al.*, Phys. Rev. Lett. 115, 205001 (2015).

[14] G. Bannasch, J. Castro, P. McQuillen, T. Pohl, and T. C. Killian, Phys. Rev. Lett. **109**, 185008 (2012).

[15] P. Mulser, F. Cornolti, E. Besuelle, and R. Schneider, Phys. Rev. E **63**, 016406 (2000).

[16] P. E. Grabowski, M. P. Surh, D. F. Richards, F. R. Graziani, and M. S. Murillo, Phys. Rev. Lett. **111**, 215002 (2013).

[17] Lowell. S. Brown, Dean. L. Preston, and Robert. L. Singleton Jr., Physics Reports **410**, 237 (2005).

[18] Craig Witte, *Computational Modeling of Low-density Ultracold Plasmas*, Ph.D. Dissertation (Colorado State University, 2017).

[19] S. D. Baalrud, Phys. Plasmas **19**, 030701 (2012).

[20] M.W.C. Dharma-wardana and F. Perrot, Phys. Rev. E **58**, 3705 (1998)

[21] T. C. Killian *et al.*, Phys. Rev. Lett. **83**, 4776 (1999).

[22] S. G. Kuzmin and T. M. ONeil, Phys. Plasmas **9**, 3743 (2002).

[23] Truman. M. Wilson, Wei-Ting Chen, and Jacob. L. Roberts, Phys. Rev. A **87**, 013410 (2013).

[24] Liam G. Stanton, and Michael S. Murillo, Phys. Rev. E **93**, 043203 (2016).

[25] F. Robicheaux, and J. D. Hanson, Phys. Rev. Lett. **88**, 055002 (2002).

[26] G. Bannasch, and T. Pohl, Phys. Rev. A **84**, 052710 (2011).

[27] K. Niffenegger, K. A. Gilmore and F. Robicheaux, J. Phys. B: At. Mol. Opt. Phys. **44**, 145701 (2011).

[28] T. M. Wilson, Dynamics of low-density ultracold plasmas in externally applied electric and magnetic fields, Ph.D. Dissertation (Colorado State University, 2013).

[29] Wei-Ting Chen, Craig Witte, and Jacob. L. Roberts, Phys. Plasmas **23**, 052101 (2016).

[30] John. C. Stewart, and Kedar. D. Pyatt, Astrophys. J. **144**, 1203 (1966).

[31] M. S. Murillo, Phys. Rev. Lett. **87**, 115003 (2001).

[32] Truman. M. Wilson, Wei-Ting Chen, and Jacob. L. Roberts, Phys. Plasmas **20**, 073503 (2013).

[33] Guthrie John and Jacob Roberts, J. Phys. B: At. Mol. Opt. Phys. **49**, 045701 (2016).

[34] M. E. Glinsky, T. M. ONeil, M. N. Rosenbluth, K. Tsuruta, and S. Ichimaru, Phys. Fluid B **4**, 1156 (1992).

[35] A. J. Kemp, Phys. Plasmas **11**, 5648 (2004).

Chapter 6

Measurements of Rydberg Atom Populations Above The Kinetic Bottleneck in A Ultracold Plasma

The free electrons and ions in an plasma do not always remain free. It is possible for electrons and ions to recombine into atoms. There are several recombination processes that can occur in plasmas: radiative recombination, dielectronic recombination, and three-body recombination (TBR). A brief description of these processes is presented here. Radiative recombination is a process where a free electron is captured by an ion through emitting a photon. This process tends to populate the captured electron at tightly bound levels. The radiative recombination rate is given by $1.55 \times 10^{-10} n_e T_e^{-0.63} sec^{-1}$ [1], where n_e is the electron density in cm^{-3}, and T_e is the electron temperature in °K. For our typical experimental conditions, $10^7 \mathrm{cm}^{-3}$ in density and 1 K in temperature, the radiative recombination time is about 645 s, which is far longer than the UCP lifetime. Dielectronic decay is a process where an electron is captured in an intermediate excited state simultaneous with a bound electron becoming excited and then emits a photon dropping to a lower bound state. The dielectronic recombination rate is given by the formula $6 \times 10^{-9} T_e^{-2.18} n_e^{1.37}$ [1]. Under the same condition described above, the dielectronic recombination time is about 0.043 s, still much longer than our UCP lifetime. Three-body recombination is a process in which two electrons collide with each other when an ion is nearby. After the collision, one of the electron loses energy and becomes bound with the ion to form a Rydberg atom and the other electron carries away energy, which conserves energy and momentum. The rate of this process is $3.8 \times 10^{-9} n_e^2 T_e^{-4.5}$ [1]. Under the same plasma conditions, the recombination time is 2.6 μs. Therefore, for UCPs, radiative recombination and dielectronic recombination are negligible, while three-body recombination is the dominant recombination process. Thus three-body recombination is the dominant source of the Rydberg atom formation in UCPs. Formation of Rydberg atoms from a plasma results in loss of plasma particles, and the fact that one of the electron gains energy means that this process heats the electron component of plasmas.

Heating due to three-body recombination is a concern in UCP research since it prevents the strong coupling parameter Γ from staying high [2–4]. Therefore, understanding three-body recombination processes and how they relate to the Rydberg atom formation is helpful for developing

possible techniques for reaching higher Γ in UCPs. This is important for experiments studying stong coupling influences on properties such as eletron-ion collision rates as mentioned in the previous chapter. In addition, the recombination rates and Rydberg atom formation rates depend on the temperature of the electrons in UCPs. By studying these rates, temperature information for UCPs can be obtained. Measurements of the electron temperature have been a long-standing challenge in the field. While electron-ion collision rates can be used to deduce the temperature, a more versatile and rapid technique would expand the range of plasma conditions that could be measured. There have been previous work on measurements and predictions of Rydberg atom formation rates in UCPs. For instance, in Ref. [6], the UCP temperature was extracted by measuring the Rydberg atom formation rate assuming the Rydberg atom formation rate scales as $T^{-9/2}$. Furthermore, the $T^{-9/2}$ dependence of the three-body recombination rates is expected to be modified in the strong coupling regime [3, 7–10]. The necessity of modification of the rate with increasing strong coupling can be seen from the fact that as T goes to zero, the rate unphysically diverges.

In this chapter, the basic background theory of three-body recombination and Rydberg atom formation will be introduced. Then we will describe the experimental technique that we used to measure highly excited Rydberg atoms. Measurements of Rydberg populations were performed at different UCP temperatures and times after plasma formation. The experimental results are compared with theoretical calculations and good agreement was found under some conditions.

6.1 Three-Body Recombination And Rydberg Atom Formation in UCPs

The conventional three-body recombination rate in a plasma is predicted to scale as $n_e^2 T_e^{-9/2}$. This temperature and density dependence can be derived from a couple of simple scaling arguments. First, the collision frequency of electron-electron collisions is proportional to $\bar{v}b^2 n_e$, where $\bar{v}$ is the average electron velocity (which is proportional to the square root of the electron temperature T_e), n_e is the electron density, and b is the Coulomb distance of closest approach that characterizes the length scale of Coulomb collisions and which scales with T_e^{-1}. Thus, the collision frequency scales as $n_e T_e^{-3/2}$. Second, the probability of finding such an event near an ion within the Coulomb interaction range scales with $n_e b^3$ which is proportional to $n_e T^{-3}$. Thus, the three-body recombination

rate ν_{3bd} scales with $n_e^2 T_e^{-9/2}$ [3]. Note that this rate can be written in the form of $\nu_{3bd} \sim \omega_p \Gamma^{9/2}$, which only depends on the plasma frequency (ω_p) and the strong coupling parameter Γ. It is clear that this temperature scaling of the three-body recombination rate is expected to break down for sufficiently low temperatures (or sufficiently strongly-coupled plasmas).

While the general argument in the above paragraph is useful for estimating the temperature and density dependence for the total Rydberg atom formation rate, it is also possible to examine the population of Rydberg atoms in a given quantum level n as a function of time to better characterize the Rydberg atom population. For a chosen level n, there are processes that both increase and decrease the Rydberg atom population in that quantum level. Three-body recombination directly to that level will increase the population. Once Rydberg atoms are formed in other quantum states n', there is also the possibility for an electron-Rydberg atom collision that will change the Rydberg atom quantum level from n' to n. This is another way that the population with quantum state n could increase. These electron-Rydberg atom collisions will also decrease the population in n at some rate, too, though and so can also decrease the population in the n state. Electron-Rydberg atom collisions can also re-ionize the Rydberg atom, decreasing not only the population in state n but the total Rydberg atom number. The population in state n will thus be a function of these processes that can either increase or decrease the population. Most of these properties do not scale with $T^{-9/2}$ and so it would not be expected that the Rydberg atom population in a given n state will scale that way. In fact, it turns out that the total Rydberg atom population itself does not scale with $T^{-9/2}$ once all of these effects are taken into account. Instead, one has to differentiate between Rydberg atom formation and atom recombination in order to recover the $T^{-9/2}$ scaling. The details of this will be presented below.

Before discussing rate equations and temperature scaling issues, it will be helpful to understand the concept of the kinetic bottleneck. Consider a single ion embedded in a sea of electrons in thermal equilibrium. Electrons enter and exit bound states, or move between bound states, constantly due to interactions with other background electrons. The processes of reionization consists of both direct ionizations from just one collision, and indirect ionizations during which the electron goes through two or more bound state transitions before ionization. The same direct and indirect processes also apply to an electron that ultimately goes to a particular n state. The concept of the kinetic bottleneck associated with the binding energy E_b is to consider the bottleneck energy as the energy

such that if an electron's energy is above E_b, then the electron tends to be reionized after some time. If an electron ever has an energy below E_b, it will most likely make a series of de-excitations through collisions and radiation until it eventually relaxes all the way to the ground state. The root cause of such a behavior is the result of the probability distribution associated with the n state that an electron eventually finds itself in after thermal equilibration. This depends on the Boltzmann factor and the phase space density [5]. Given this, the flux that passes (either upward or downward) through some phase space surface scales as [5]

$$Flux \sim \frac{1}{|E|^{3.83}} e^{-E} \tag{6.1}$$

where E is the binding energy whose value is negative. The $1/|E|^{3.83}$ term is the phase space factor and the e^{-E} term is the Boltzmann factor. The flux is large at small E because of the $1/|E|^{3.8}$, and the flux is also large at large E where the Boltzmann factor becomes large. The flux has a minimum value at $E_b = 3.83$ which is the bottleneck energy. When electrons are above the bottleneck energy, the resulting rate is in favor of moving toward higher energy levels due to the larger phase space factor for higher energies, which leads to a higher probability for electrons to be reionized. When the electrons are below the bottleneck energy, the rate is more favorable of the atom decaying to lower levels because of the Boltzmann factor getting larger. In other words, the bottleneck energy is the energy at which the probability for an electron to be reionized is 0.5 [3]. Therefore, the rate for those electrons to go below the bottleneck so that the resulting atoms are stable, and are not ionized again, is given by

$$R_{rec} = 3.89 \times 10^{-9} n_e^2 T_e^{-4.5} s^{-1} \mathrm{cm}^3 K^{-1} \tag{6.2}$$

where n_e is the plasma electron density in cm^{-3}, and T_e is the electron temperature. One implication from this is that the $T_e^{-4.5}$ scaling is an evaluation of the one way flux through the bottleneck [11]. If one wants to study the Rydberg atoms formation rates in certain range of principle quantum number n rather than those below the bottleneck energy, then one has to use rate equations to trace the populations within the energy range of interest. This is an important distinction that is sometimes overlooked in UCP physics.

The relevant rate equations are given in Ref. [3]

$$\frac{d\rho_n(t)}{dt} = \rho_e(t)\sum_{n'\neq n}[\rho_{n'}(t)R(n',n) - \rho_n(t)R(n,n')] + \rho_e(t)^3 R_{rec}(n) - \rho_e(t)\rho_n(t)R_{ion}(n) \quad (6.3)$$

$$\frac{d\rho_e(t)}{dt} = \rho_e(t)\sum_{n'}[\rho_{n'}(t)R_{ion}(n') - \rho_e(t)^2 R_{rec}(n')] \quad (6.4)$$

where $\rho_n(t)$ is the n-level population density in state n, ρ_e is the free electron density, $R(n,n')$ is the excitation ($n' > n$) and de-excitation ($n' < n$) rate constant, $R_{rec}(n)$ is the recombination rate to level n, and $R_{ion}(n)$ is the ionization rate at level n. The rate constants are obtained from classical Monte-Carlo trajectory simulations, and are listed as follows. The excitation rate is

$$R(n,n') = k_0\epsilon_{n'}^{3/2}e^{\epsilon_{n'}-\epsilon_n}[\frac{22}{(\epsilon_n+0.9)^{7/3}} + \frac{4.5}{\epsilon_n^{5/2}\Delta\epsilon^{4/3}}], \quad (6.5)$$

the de-excitation rate is

$$R(n,n') = k_0\frac{\epsilon_n^{5/2}}{\epsilon_{n'}}[\frac{22}{(\epsilon_n+0.9)^{7/3}} + \frac{4.5}{\epsilon_n^{5/2}\Delta\epsilon^{4/3}}], \quad (6.6)$$

the recombination rate to level n is

$$R_{rec}(n) = \frac{11\sqrt{\mathtt{R}/k_BT_e}k_0n^2\Lambda_{de}^3}{\epsilon_n^{7/3} + 4.38\epsilon_n^{1.72} + 1.32\epsilon_n}, \quad (6.7)$$

and the reionization rate from level n is

$$R_{ion}(n) = \frac{11\sqrt{\mathtt{R}/k_BT_e}k_0e^{-\epsilon_n}}{\epsilon_n^{7/3} + 4.38\epsilon_n^{1.72} + 1.32\epsilon_n}, \quad (6.8)$$

where $k_0 = e^4/(4\pi\epsilon_0)^2 k_B T_e \sqrt{m_e \mathtt{R}}$, $\epsilon_n = \mathtt{R}/n^2 k_B T_e$, $\Delta\epsilon = |\epsilon_n - \epsilon_{n'}|$, $\Lambda_{de} = \sqrt{h^2/2\pi m_e k_B T_e}$ is the thermal de Broglie wavelength, $\mathtt{R} = 13.6eV$ is the Rydberg unit of energy, and h is the Planck's constant.

If one wants to model the population even for just one n state, theoretically, one will have to sum over all possible transitions which includes an infinite number of states (from ground state $n = 1$ to $n = \infty$). Since it is impossible to sum over infinite states, in practice one has to sum from $n = 1$ to a chosen cutoff level, denoted as n_{cut} for our calculations. One would expect when n_{cut} is large enough, the result between different cutoffs will converge. This convergence behavior is illustrated in Fig. 6.1. In Fig. 6.1, we calculated the populations between a weighted n value from $n = 128$ to $n = 164$ by computing the rate equations including contributions from $n = 1$ to various n_{cut}. The weighting of the different populations is determined by our experimental parameters, as will be described in detail below.

In the energy range of Rydberg atoms that we are interested in, the different n_{cut} results converge at $n_{cut} \sim 400$ at least for the plasma temperature 2.87K. In Ref. [5], a parameter β was introduced to estimate at what n_{cut} the calculated results converge. The parameter β is roughly the ratio of energy of the phase space surface to the Coulomb energy. They found that their results converge at $\beta \sim 8$ [5]. By choosing the value of the energy surface energy to be the bottleneck energy ($\sim 3.83 k_B T_e$), and $\beta = 8$, which gives a cutoff at $n_{cut} \sim 330$, which is close to what we see in our calculation.

6.2 Experimental Measurement of Rydberg Atom Populations

In the section, the experimental techniques we used to measure Rydberg atom populations will be described. We first create a UCP as described in previous chapters. After waiting for a designed amount of time (usually a few μs), we apply a "clear out" electric field to get rid of all of the free plasma electrons. We maintained the field for about 5 μs to give those plasma electrons enough time to leave the UCP. Then we apply a field ionization pulse to ionize the Rydberg atoms. Those ionized electrons are detected by the MCP. The sequence is summarized alongside a typical experimental trace as shown in Fig. 6.2. The reminder of this section will provide details about

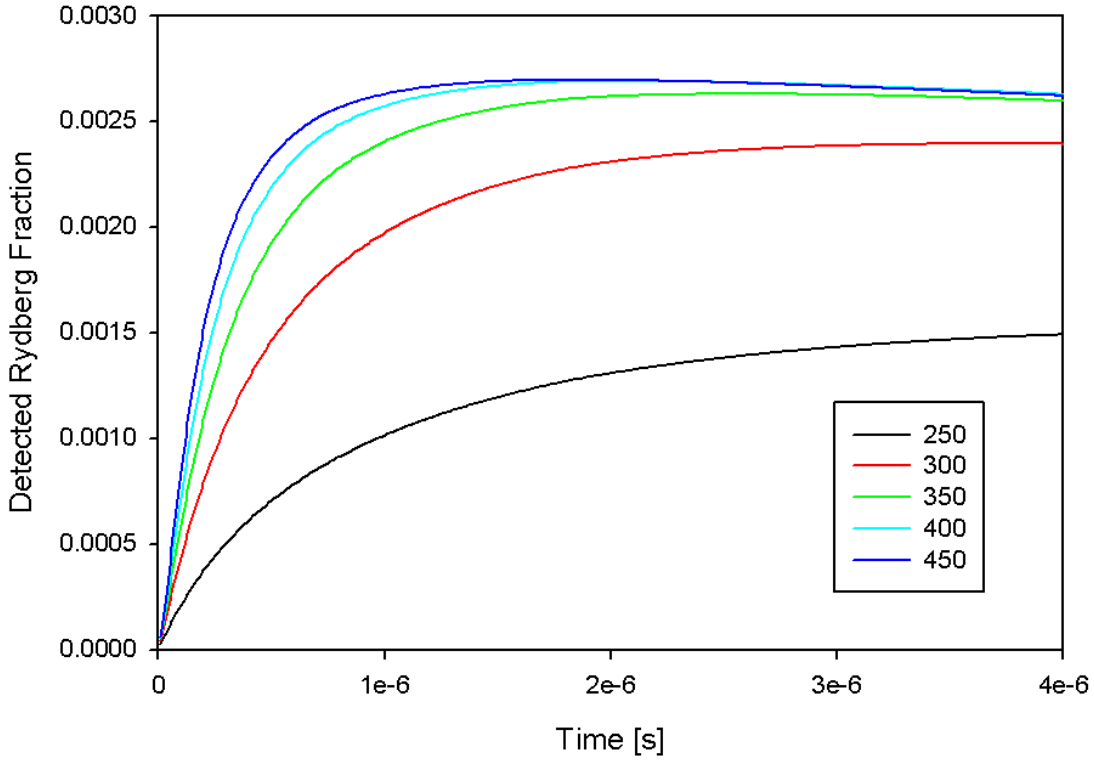

Figure 6.1: The ratio of the number of Rydberg atoms between principle quantum number of weighted value from $n = 128$ to $n = 164$ to the total plasma ion numbers with respect to the time after plasma formation. We perform calculations at different n_{cut}. The results start to converge around $n_{cut} = 400$.

the sequence shown in Fig. 6.2. We performed our experiments with $\sim$ 70000 ions, and with a characteristic spatial size of 630 μm.

The clear out field is a generated by an Agilent 33250A function generator. The pulse has a 1 μs rising edge, and then reaches the maximum voltage 2.5 V which lasts for 5 μs, then falls back in 1 μs. The magnitude of the "clear out" electric field is 44.5 V/m at the center of the UCP. The reasons why we implemented a clear our pulse is that we want to measure the Rydberg atom population at a certain time after plasma formation, and the way we detect Rydberg atoms is through measuring field ionized electrons from the Rydberg atoms. Therefore, if we don't clear out the plasma electrons in the first place, there will be signal contamination coming from those free electrons in the UCP. The value of the electric field that we need to apply to the UCP in order to extract all the free electrons is calculated as follows. We first assume the ions have a smoothed Gaussian spatial distribution of characteristic size of 630 μm, and the total amount of charge is that associated with 70000 ions. We can calculate the electric field created by the smoothed ion distribution and calculate how much DC electric field we need to apply to the ions to flatten the trapping potential created by the ions, so that free electrons no longer are confined and will all escape.

We used a Tektronix AFG3102 duo channel function generator to create the field ionization pulse. We combine the output from both channels, and the electric field pulse we used has a full width of half maximum of about 10 ns with maximum peak voltage of 14 V, and the electric field of the ionization pulse is 75.0 V/m.

Applying a "clear out" electric field that is then followed by an ionization field pulse has a significant consequence. The "clear out" pulse not only removed free electrons but field ionized those Rydberg atoms with energy above some level n_1. Likewise, the field ionization pulse ionized those Rydberg atoms with energy above n_2. Thus, the Rydberg atoms ionized by the field ionization pulse are those Rydberg atoms within the range of $n_2 < n < n_1$. The relation between the electric field strength and the smallest n state that can be ionized by the field is [12]

$$E_{ion} = \frac{1}{16n^4}, \tag{6.9}$$

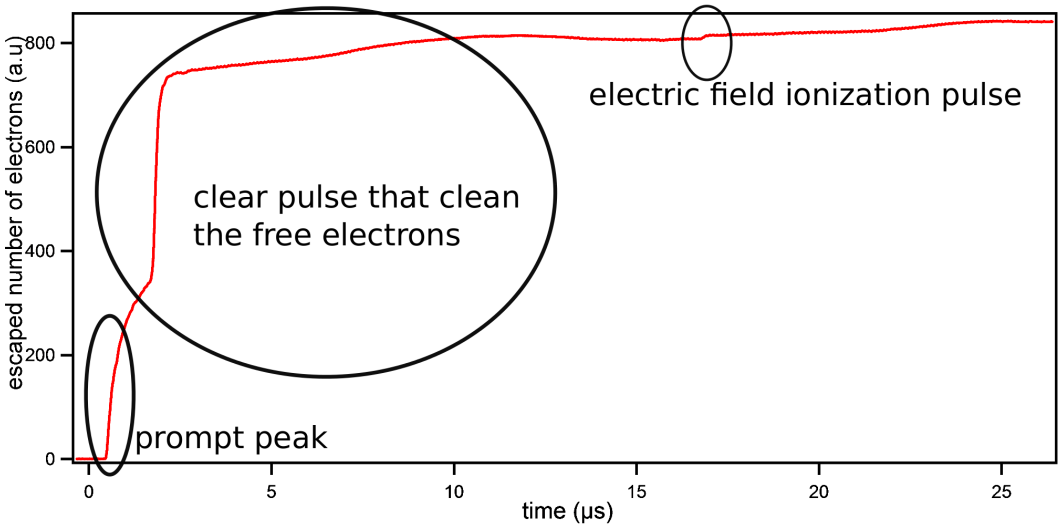

Figure 6.2: A typical trace from a Rydberg atom experiments and the illustration of experimental sequence.

where E_{ion} is the electric field, and n is the principal quantum number. The formula is in atomic units, and a unit electric field in atomic units is $5.14 \times 10^{11} V/m$, which is equal to the field created by an elementary charge at a distance of a Bohr radius. Given the electric fields mentioned above, the Rydberg population observed in our measurements corresponded to those occupying the range from $n = 144$ to $n = 164$. This range is narrower than ideal, but was the best we could do in the experimental apparatus at the time our data were collected.

We found in simulations that 4 μs after the plasma formation, for plasma temperatures higher than 2 K, the numbers of Rydberg atoms within this range of levels are close to their equilibrium values. We thus focused on taking measurements at 4 μs under different temperatures to avoid having to account for population dynamics.

6.3 Results And Discussion

Fig. 6.3 shows the Rydberg atom fractions measured 4 μs after UCP formation with respect to different UCP temperatures. The Rydberg atom fraction is defined as the ratio of the measured Rydberg atom number to the total ion number. The temperature is determined in the following way. As mentioned in chapter 5, the presence of an applied external electric field during plasma formation will heat up the UCP. There was a 2.0 V/m DC electric field present in the UCP region in our experiments. Therefore we performed a MD simulation at an initial temperature $k_B \times$ 1.5 K (i.e. initial kinetic energy 2.25 K) and calculate the temperature 1μs after formation. The temperature obtained from the MD simulation was 2.67 K which indicates an amount of heating of 1.17 K. We assume that the amount of heating for initial temperature higher than 1.5 K was the same since the three-body recombination heating is not significant for these conditions and the dominant factor that affects the UCP temperature is the electric field heating, which is a temperature insensitive mechanism. Thus the assumed temperatures were the initial temperature plus the 1.17 K from the electric field heating. The exception to this are conditions where the initial temperature is below 1.5K. For those initial temperatures, we had to run a MD simulation at an initial temperature of 1 K in order to determine the UCP temperature, because there's no simple recipe to determine the temperature around that condition. This is due to the fact that the three-body recombination heating is no longer negligible, and hence the UCP temperature was affected by both electric field

heating and three-body recombination heating. Although the electric field heating remains the same, the three-body recombination heating is known to have a strong dependence on the plasma temperature. Thus a MD simulation was required to obtain the temperature for MD simulations including all these factors.

In Fig. 6.3, we observe that the measured Rydberg atom fraction dropped as the temperature becomes larger. This behavior is expected since for higher temperatures, the three-body recombination rates decreased rapidly. We further compared our measurements to theoretical predictions of the Rydberg fractions using the model described in section 6.1.

This section contains a more detailed description of how we model Rydberg atom populations under our experimental conditions. The measured data was the Rydberg population within a particular range of n, so we integrated rate equations through time. In this calculation, a spherically-symmetric UCP was assumed, and we broke up the UCP into spherical shells that had roughly the same density. The spatial distribution of electrons is approximated by a $T_e = 0$ distribution which was a good approximation under these low temperature conditions. We needed to know the numbers of electrons in the UCP to calculate the Rydberg populations, but electrons evaporate out of the UCP continuously. We therefore used the experimentally measured evaporation rates in the model to account for the electron loss.

To mimic the experimental process mentioned in the previous section, at a selected time the clear out pulse was applied in the model. Note that before the clear out electric field pulse was applied, several processes could have affected the electron temperature in the UCP. They include Rydberg atom formation which heated up the plasma electrons, Rydberg state changing collisions which could have either heated or cooled the electrons, and Rydberg atom reionization which cooled the electrons. We ignored evaporative cooling in the calculation. Since the change in the electron temperature affected the Rydberg atoms formation rate, we tracked the electron temperature through energy conservation. When the clear out pulse was applied, the local electric field was calculated assuming all free electrons were removed. Any high-lying Rydberg atoms above the local field ionization limit were assumed ionized. This was repeated for the field ionization pulse, but this time the number of atoms ionized was recorded. In both cases above, an electric field based on Simion calculations for our electrode geometry was used to model the electric field across the UCP.

We found good agreement between the measured data and the calculation results. Note that our theoretical predictions were no-free-parameter calculations. We fit the data with a power law function $y0 + aT_e^b$ where $y0$ fits to zero within the error bars, a, and b are fitting parameters, and T_e is the electron temperature. This resulted in a fitted power of $b = 1.90 \pm 0.51$ with respect to the UCP temperature. We also fit theoretical predictions with a power law which produced a fitted power of 2.30 ± 0.14.

From these measurements taken at 4 μs after plasma formation, we roughly verify the validity of the model described in Ref. [3]. The clear dependence of the Rydberg population with respect to the temperature of UCPs is helpful in that it provides another method for measuring UCP temperatures. We may be able to apply this technique to measure the temperatures of UCPs for future experiments.

Although the measurements at 4 μs after the formation agree well with the calculation, measurements conducted at earlier times with respect to the formation are not yet understood. We conducted these measurements by applying the clear out electric field earlier in time. By removing free electrons earlier, the Rydberg atoms we measured corresponded Rydberg atom populations earlier in time. We found that for the measurements of initial ionization energy within the range 1.1 K to 1.8 K, the Rydberg populations at 2 μs are measured to be a factor of two to three times larger than those at 4 μs. For initial ionization energy larger than 1.8 K, we measured the Rydberg populations at 2 μs to be about the same as those of 4 μs. In contrast, the theoretical calculations showed the Rydberg populations are already close to equilibrium at 2 μs after formation, nowhere close a factor of two difference. This observation, being so inconsistent with theoretical expectations, means that there is significant physics involved that is not yet understood.

One possibility is that those larger signals at 2 μs contained free electrons that distorted the Rydberg population measurement. Although the ion density distribution is a Gaussian, there exists density fluctuations. That means that there are some ions that are spatially closer together or farther away as compared to the expectation of the average density value. Estimates show that higher density regions of ions are able to trap electrons with kinetic energy of about 1 K to 2 K. Thus, for low initial kinetic energy conditions, there could be some free electrons trapped locally, but for higher initial kinetic energy cases, the depth of local density fluctuations is not deep enough to trap them. At 4 μs, the ion density fluctuation decreases due to the relaxation of the correlation

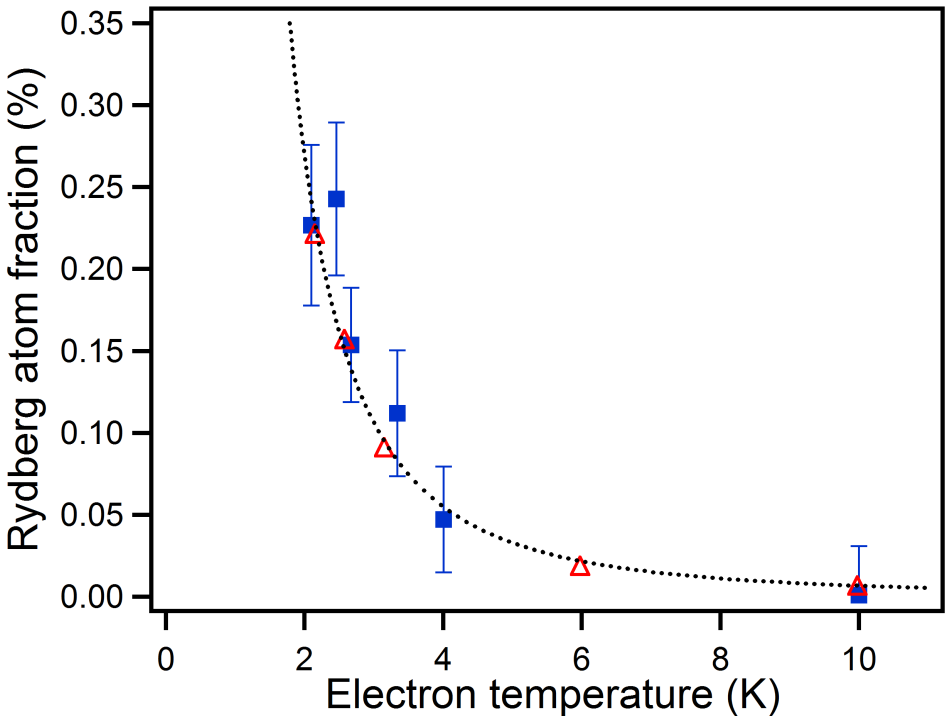

Figure 6.3: Rydberg atom fractions vs temperature. The blue squares are the measured data, and the red triangles are the theoretical calculations using model in Ref. [3]. The dash line is the power law fir to the calculated points.

energy (via disorder induced heating), and hence the trap depth due to density fluctuations would no longer be able to trap free electrons. Although this hypothesis is able to explain qualitatively of what we observed, the UCP ions had a substantial amount of time (12 microseconds) to expand after the clear out pulse while the electric field was still being applied. We would expect the local potential traps created by ion density fluctuation would be greatly reduced due to disorder induced heating and the plasma expansion. Therefore, trapping by density fluctuation would require the local "cluster" of ions to continue to trap any free electrons during the expansion of the ions after the clear out pulse. It is not immediately obvious how this could be case, however, and so this speculation about the possible source of our difficult-to-explain measurements has difficulties itself. The lack of understanding of the reason of high Rydberg population numbers at early time periods naturally raises doubts about the interpretation of our 4 μs measurements. At time of the writing of this thesis, this discrepancy remains unresolved. Until it is resolved, the interpretation of our data remains uncertain.

There are also several other issues we observed in this set of experiments. We saw day to day variations for the values of measured signals under what should have been the same conditions. We suspect this is likely due to the background subtraction process not fully removing the background. In our Rydberg atom experiment, we took traces with the presence of the ionization pulse as shown in Fig. 6.2, and we also took traces without the presence of the ionization pulse as background traces. We then subtract the two traces in order to eliminate the signal which was not from ionization of Rydberg atoms. Because the background traces were not instantaneous background traces, and the subtraction may not have been able to fully remove the background. If that was the case, then improper background subtraction could have caused our signals to appear to vary more than they did. This variation would likely be random so by averaging the data of different sets, we could reduce the influence of such an effect on the average populations measured. One of the reasons that we suspect background subtraction issues might be the cause of the day-to-day irreproducibility is that with the very small signal sizes involved in these measurements, we would be far more sensitive to background subtraction issues than in previous experiments. It should be emphasized, though, that the day-to-day variation are not yet understood which represents perhaps another problem with our measurements.

In addition, although we find good agreement between the theory and measurements, the n value of the levels needed in our calculation extended beyond the range of n which was validated in the original theory. The calculations in the related references were performed by assuming a single ion embedded in a thermalized electron bath. When n is sufficiently large, the corresponding orbital size becomes the same as or larger than the interparticle spacing. For such cases, a single ion picture for Rydberg atom formation is no longer an adequate description (i.e. a many-body description would be needed in this case). For the n range we were measured, the circular orbital size is less than 1.5 μm and the interparticle spacing is about 28 μm. Thus we are not particularly worried about the validity of the results from a single particle treatment. We do not know, however, how reliable the rate equations are for populations in higher n levels that are relevant to our formation rate.

From a limited perspective, the situation with respect to measuring Rydberg atom populations in UCPs looks good in that agreement between theory and experiment seems reasonable. However, for other conditions the comparison fails and we also did not understand our day-to-day reproducibility. Thus, the measurements that are described in this chapter need to still be considered preliminary.

Future studies are planned that should have much better signal-to-noise. This should allow evaluation of the day-to-day fluctuation issues more clearly. MD modeling will be performed to see if the early excess Rydberg atom populations are observed in such a simulation as well. If so, the physics of this phenomenon will be investigated. If not, additional experimental measurements will be needed to evaluate where the excess signal is coming from. In any case, continued work is planned using many of the same techniques described in this chapter.

6.4 Conclusion

By introducing a combination of electric field pulses and using field ionization of Rydberg atoms, we are able to measure the Rydberg atom populations for a range of n states. We performed measurements at different UCP temperatures, and observed a temperature dependence in the measured Rydberg atom populations. By fitting the data with a power law, we obtained a fitted power 1.75 ± 0.9. We also found our measurements agree with our parameter-free calculations based

on the model in Ref. [3]. However, the fact that we currently cannot explain high Rydberg atom numbers at early times just after to UCP formation makes us unable to rule out the possibility that the agreement between the measurement and the calculation is a coincidence. Therefore, further theoretical and experimental studies are needed. Experimentally, we have redesigned the system by switching from using electrodes to using grids (see section 3.6). This upgrade of our system is expected to increase our signal size. By increasing the signal-to-noise ratio and figuring out a better way to subtract the background, we can greatly increase the precision of the experiments. One immediate application of this is that we can turn the Rydberg atom population measurements into a temperature measurement of the electron component of UCPs, which has been challenging for UCP experiments. The new grid design also allows us to measure more deeply-bound Rydberg atoms which means we will be able to measure Rydberg populations below the bottleneck energy due to the capability of applying larger electric fields. These theoretical and experimental works will be subjects of future study.

References

[1] J. Stevefelt, J. Boulmer, and J-F. Delpech, Phys. Rev. A **12**, 1246 (1975)

[2] F. Robicheaux, and J. D. Hanson, Phys. Rev. Lett. **88**, 055002 (2002).

[3] G. Bannasch, and T. Pohl, Phys. Rev. A **84**, 052710 (2011).

[4] K. Niffenegger, K. A. Gilmore and F. Robicheaux, J. Phys. B: At. Mol. Opt. Phys. **44**, 145701 (2011).

[5] Peter Mansbach, and James Keck, Phys. Rev. **181**, 275 (1969).

[6] R. S. Fletcher, X. L. Zhang, and S. L. Rolston, Phys. Rev. lett. **99**, 145001 (2007).

[7] Y. Hahn, Phys. Rev. E **64**, 046409 (2001).

[8] B. Zygelman, J. Phys. B **36**, L31 (2003).

[9] A. V. Lankin and G. E. Norman, J. Phys. A **42**, 214042 (2009).

[10] A. A. Bobrov, S. Y. Bronin, B. B. Zelener, B. V. Zelener, E. A. Manykin, and D. R. Khikhlukha, J. Exp. Theor. Phys. **112**, 527 (2011).

[11] S. G. Kuzmin and T. M. O'Neil, Phys. Plasmas **9**, 3743 (2002).

[12] Thomas F. Gallagher, *Rydberg Atoms*, Cambridge (1994)

[13] Wei-Ting Chen, Craig Witte, and Jacob. L. Roberts, Phys. Plasmas **23**, 052101 (2016).

[14] Truman. M. Wilson, Wei-Ting Chen, and Jacob. L. Roberts, Phys. Plasmas **20**, 073503 (2013).

[15] Guthrie John and Jacob Roberts, J. Phys. B: At. Mol. Opt. Phys. **49**, 045701 (2016).

Chapter 7

Future Work

In a previous chapter, we described measurments of the strong coupling influence on electron-ion collision rates by measuring the damping of the electron CM oscillation in UCPs. Using the same setup, we are also able to measure the Rydberg atom populations at different temperatures and we find agreement between theoretical calculation and the measurements. We can explore more topics in plasma physics by applying the techniques developed in this thesis. In addition to all the interesting results we achieved, we have learned that there are several places in which we can improve future experiments. In this chapter, some possible future research directions will be described. They are: measuring the strong coupling effect on electron-ion collision rates in a magnetized plasma, measuring the the below bottleneck Rydberg population, and the study of evaporation rates.

7.1 Strong Coupling Influence on Electron-Ion Collisions in Magnetized UCPs

Almost every plasma system, from the earth's ionosphere, the solar wind, the sun, dense stellar objects such as white dwarfs and neutron stars, and jet phenomenons etc, involves a significant interaction with respect to magnetic fields. Therefore, to study and understand the influence of magnetic fields on plasma behavior is important. Generally speaking, the presence of a magnetic field results in changes to plasma transport properties. These changes can be observed in collective modes, fluid dynamic properties such as turbulence, and individual collisions. Although our UCPs are able to test the magnetic field influence on collective modes in plasmas, here we focus on measuring its effect on electron-ion collisions through measurements in a UCP system.

As mentioned in chapter 4, from the perspective of collision, a plasma starts becoming magnetized when the typical cyclotron radius r_c becomes smaller than the Debye screening length λ_D. This makes sense since the cutoffs used in collision treatments are based on the screening length. When the cyclotron radius is large compared to λ_D, the deflections of a particle are still dominated by normal binary collisions that occurs within the Debye sphere. When r_c becomes shorter than

λ_D, the gyromotion becomes more significant within the Debye sphere. Thus the expressions for electron-ion collisions are expected to be modified.

Because the UCPs' temperature can be as low as few degrees Kelvin, the field needed to magnetize the plasma is also relatively low ($<$ 1 Tesla). The required field strength to magnetize UCPs can be generated in a lab. For instance, taking the coldest condition we achieved in chapter 5, the temperature is 1.67 K, and the density is about 10^7 cm^{-3}. The magnetic field required to just magnetize the plasma is 17 G, and a 200 G magnetic field can make r_c more than 10 times smaller than λ_D. We therefore have a clean system with well controlled and tunable initial conditions to study electron-ion collision rates of a magnetized plasma in both strong and weak coupling regimes. The experiments to be conducted would be largely similar to those described in chapter 5. Electron oscillation damping rates would again be measured, but this time with a much stronger applied magnetic field. In some respects, such measurements should be easier as the collisionless damping effects should be reduced by the stronger magnetic field. The apparatus that provides the required magnetic field is now under construction.

7.2 Measurements of Rydberg Atom Formation and Populations Below Bottleneck Level

As can be seen in chapter 6, the Rydberg atoms we measured were excited to levels above the bottleneck energy. Their population and formation rates depend on three factors which were the three-body recombination rate, the reionization rate, and the energy-level-changing electron-Rydberg atom collision rate. However, for the formation rate below the bottleneck, they were largely only sensitive to the three-body recombination rate. Since the electron temperatures can be determined independently by measuring the electron CM oscillation damping rate, if we measure the Rydberg population below the bottleneck, we can more directly test the temperature dependence of the three-body recombination rate under higher Γ.

In order to field ionize the population below the bottleneck energy, we have to apply a larger electric field (Eq. 6.9). The electric field we were able to apply to the apparatus that we performed the Rydberg measurements in was limited. This is because if the electric field ionization pulse is sufficiently large, the electrons could hit the electrode when they escape from the UCP. To address

this problem, we have already designed and implemented a grid system to replace the electrode apparatus. By doing so, we can apply a higher electric field to ionize Rydberg atoms below the bottleneck energy without being concerned about electron loss.

7.3 Study of Evaporation Rates

The evaporation rate of UCPs is determined by electron temperature, number density, and the depth of the trapping potential. Thus, the measurement of the electron evaporation rate contains temperature information. However, according to the work in Ref. [1], one cannot simply use the standard evaporation model applied to atomic collisions to evaporation in UCPs. In addition, the evaporation rates are very sensitive to the depth which in turn depends on the actual ion density distribution and the applied external electric field. The complicated electric field environments generated by using electrodes prevented us from modeling the evaporation correctly. The change to grids will produce a simpler electric field environment, which should allow us to model evaporation (both through molecular dynamic simulation and the model used in Ref. [1]) more precisely, which we can then compare to the measured evaporation rates. We can then use the measured evaporation rates to extract the temperature information of UCPs, which would be a much easier way to measure the electron temperatures in UCPs since we measure the evaporation rate in every data trace. In addition, evaporation rates also depend on collisions in the plasma, so we can use the Monte-Carlo binary collision model described in chapter 4 and chapter 5 to model evaporation to test different plasma collision expressions more rapidly over a wider range of parameters. Finally, by understanding the evaporation of UCPs, there might be a way to utilize evaporative cooling to increase Γ in our UCPs. Repeating the measurements in chapter 6 with this ability to apply a larger electric field should produce useful insights into the three-body recombination rate.

7.4 Conclusion

UCPs provide a valuable tool to study plasma physics in a clean system with tunable and well controlled initial conditions. We can study collective modes, individual collisions and strong coupling effects using UCPs. In the work presented in this thesis, we report our development of a two-short-electric-pulse technique to study strong coupling influence on electron-ion collision rates.

We observed a much larger effect on strong coupling as compared to theoretical predictions in the literature. We also showed our system is able to conduct Rydberg atom measurements which, although not conclusive, found a good agreement between data and theory from a specific model [2]. Other than the subjects conducted in this thesis, there are much more topics in plasma physics to explore by using UCPs. We discover what needs to be done for us to improve our experiments. We are in the process of upgrading the apparatus by switching to using grids to provide the desired electric field, and we think this upgrade will be beneficial for our future experimental studies.

References

[1] Craig Witte and Jacob Roberts, Physics of Plasmas **24**, 052122(2017).

[2] G. Bannasch, and T. Pohl, Phys. Rev. A **84**, 052710 (2011).